Construction of a Structurally-controlled Pt Shell-Pd Core Catalyst by Hydrogen Sacrificial Protection Method and Its Application for Polymer Electrolyte Fuel Cells

(犠牲水素法による構造制御Ptシェル-Pdコア触媒の構築および固体高分子形燃料電池への適用)

Katsumasa Matsumoto

Graduate School of Chemical Sciences and Engineering

Hokkaido University

2021

Acknowledgements

First of all, I would like to express my deep gratitude to Professor Emeritus Kohei Uosaki for his advice and cooperation. He has advised the best approach for carrying out this research.

I would like to express my special gratitude to Professor Hidenori Noguchi for his patience in experimenting and writing this thesis and for giving me a lot of appropriate advice.

I would like to express my special gratitude to Dr. Takashi Iijima and Mr. Masataka Hiyoshi for their deep involvement in this research and both public and private.

I would like to thank Dr. Kenichi Uemura for giving me the opportunity to study at Hokkaido University and National Institute for Materials Science (NIMS).

I would like to express my deep gratitude to everyone involved in Nippon Steel Corporation.

I would like to thank all the people who have taken care of me in the Hokkaido University, NIMS Nano Interface Group, NIMS Microstructural Characterization Platform, NIMS Battery Research Platform, and Nippon steel technology Co., Ltd.

Finally, I would like to thank my parents, wife, and children for their warm encouragement and lots of supports.

Katsumasa Matsumoto

Amagasaki

September 2021

Table of Contents

Chapter 1

INTRODUCTION

1.1 General introduction

Currently, expectations and requirements for renewable energy are increasing year after year in response to various environmental issues such as global warming. From the point of view of global warming, the solution to the CO_2 problems is an urgent problem and a big challenge for humanity [1-2]. To solve these problems, technological innovation in energy conversion materials is remarkable, and various research have carried out great challenges and innovations for reducing CO_2.

Fuel cells (FCs) are one of the candidates for solving these problems because they can generate electricity and water by a chemical reaction between hydrogen and oxygen without CO_2 emission during operation. Thus, FCs are positioned as the expected source of clean energy [3-4]. The principle of FC power generation was discovered by Grobe of England in 1839 during an experiment on water electrolysis [5]. Grobe carried out an experiment on the electrolysis of water and found that the current was flowing when the hydrogen gas and oxygen gas generated remained after the electrolysis was stopped. This is a result of the reaction of hydrogen and oxygen by the Pt electrode to produce electricity. This discovery is at the heart of current FCs.

So far, various types of FC have been devised, and the basic configuration is a structure in which an electrolyte is sandwiched between two electrodes called an anode

and a cathode. The energy generation mechanism and operating temperature range differ depending on the type of electrode and electrolyte, and the application also differs depending on the type of FC. **Table 1-1** shows the various FCs that have been built and are currently in use and developed [6].

Alkaline fuel cells (AFCs) were one of the first fuel cell technologies developed and the first type widely used in the U.S. space program to generate electrical energy and water onboard spacecraft. These FCs may use aqueous potassium hydroxide solution as the electrolyte and various non-precious metals as catalysts for the anode and cathode catalysts.

Phosphoric acid fuel cells (PAFCs) use liquid phosphoric acid as the electrolyte. This acid is contained in a Teflon-bonded silicon carbide matrix and the porous carbon electrodes contain a platinum catalyst.

Molten carbonate fuel cells (MCFCs) are being developed for natural gas and coal-fired power plants for electrical, industrial, and military applications. MCFC is a high-temperature FC that uses an electrolyte consisting of a mixture of molten carbonate salt suspended in a porous matrix of chemically inert ceramic lithium aluminum oxide. Operating at temperatures as high as 650 °C, non-precious metals can be used as anode and cathode catalysts, reducing costs.

Solid oxide fuel cells (SOFCs) use a hard, non-porous ceramic compound as the electrolyte. SOFCs are about 60% efficient at converting fuel to electricity. For applications designed to capture and use the residual heat of the system (cogeneration),

the overall efficiency of fuel consumption can exceed 85%. SOFCs operate at very high temperatures, as high as 1,000 °C. High temperature operation eliminates the need for precious metal catalysts and reduces costs. In addition, SOFCs can reform fuel internally, allowing the use of a variety of fuels and reducing the costs associated with adding reformers to the system.

Polymer electrolyte fuel cells (PEFCs), also called proton exchange membrane fuel cells, provide high power density and the advantages of low weight and volume over other FCs. PEFC uses a solid polymer as an electrolyte and uses a porous carbon electrode containing platinum or a platinum alloy catalyst. All the need to work is hydrogen, air oxygen, and water. They are generally supplied with pure hydrogen from storage or reforming tanks. PEFCs operate at a relatively low temperature of about 80 °C. The low-temperature operation allows for quick start-up (shorter warm-up time) and prevents wear on system components for improved durability. However, it requires the use of precious metal catalysts (usually platinum) to separate electrons and protons from hydrogen, which increases the cost of the system. Platinum catalysts are also very sensitive to carbon monoxide poisoning, so if hydrogen is derived from hydrocarbon fuels, additional reactors will need to be used to reduce carbon monoxide in the fuel gas. This reactor also adds to the cost. PEFC is primarily used for transportation and some cogeneration systems. PEFC is particularly suitable for passenger vehicles, such as cars and buses due to its short start-up time and excellent power-to-weight ratio. PEFC has already been used in household FC since 2009 and in FC vehicles since 2014.

In Japan, it has been commercialized and the market is expanding since 2020 [7].

Table 1.1 The different FCs that have been built and are currently in use and development.[6]

	AFC Alkaline	PAFC Phosphoric Acid	MCFC Molten Carbonate	SOFC Solid Oxide	PEFC Polymer Electrolyte
Operating temp.(°C)	<100	160-220	600-800	800-1000 Low temperature(500-600)possible	60-120
Electrolyte	KOH	H_3PO_4 immobilized in SiC matrix	Li_2CO_3-K_2CO_3 eutectic mixture immobilized in γ-$LiAlO_2$	YSZ(yttria stabilized zirconia)	Perfluoro sulfonic acid (Nafion membrane)
Charge carrier in the electrolyte	OH^-	H^+	CO_3^{2-}	O_2^-	H^+
Anode reaction	$H_2+2OH^- \rightarrow 2H_2O+2e^-$	$H_2 \rightarrow 2H^+ + 2e^-$	$H_2+CO_3^{2-} \rightarrow H_2O+CO_2+2e^-$	$H_2+O_2^- \rightarrow H_2O+2e^-$	$H_2 \rightarrow 2H^+ + 2e^- \rightarrow H_2O$
Cathode reaction	$1/2O_2+H_2O+2e^- \rightarrow 2OH^-$	$1/2O_2+2H^++2e^- \rightarrow H_2O$	$1/2O_2+CO_2+2e^- \rightarrow CO_3^{2-}$	$1/2O_2+2e^- \rightarrow O^{2-}$	$1/2O_2+2H^++2e^- \rightarrow H_2O$

1.2 Principle of FCs

Figure 1-1 shows the structure of PEFC consisting of a gas diffusion layer, a catalyst layer, a bipolar plate, and a polymer electrolyte membrane (PEM). The gases supplied to PEFC are O_2 and H_2, and the reduction and oxidation reactions occur at the cathode and anode, respectively. PEM separates the two electrode reactions. For the anodic reaction, H_2 flows through the gas diffusion layer and reaches the catalyst layer, where dissociation into two electrons and two protons occurs. The two protons pass through the PEM to reach the cathode catalyst layer, while the two electrons pass through an external circuit to reach the cathode. Therefore, the anodic reaction can be expressed as:

$$H_2 \rightarrow 2H^+ + 2e^- \qquad E^o = 0.00 \text{ V vs. SHE} \qquad (1.1)$$

Similarly, in the case of a cathodic reaction, air reaches the catalyst layer through a gas diffusion layer, where it reacts with two electrons, where the two protons result from an anodic reaction that produces heat and water. Therefore, the cathodic reaction can be expressed as:

$$1/2O_2 + 2H^+ + 2e^- \rightarrow H_2O \qquad E^o = 1.23 \text{ V vs. SHE} \qquad (1.2)$$

Then, the overall PEMFC reaction is:

$$H_2 + 1/2O_2 \rightarrow H_2O \qquad E^o = 1.23 \text{ V vs. SHE} \qquad (1.3)$$

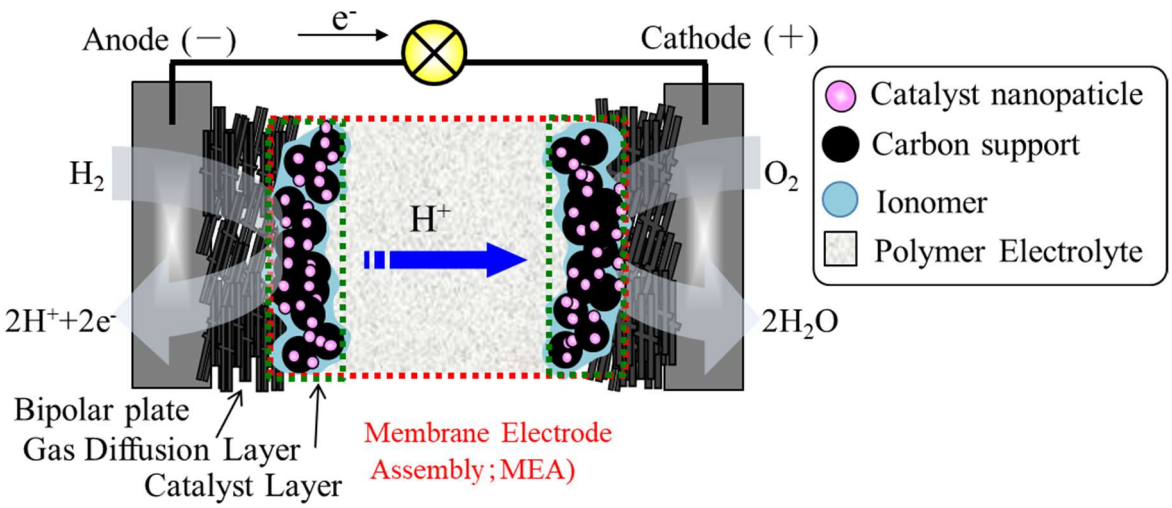

Figure 1-1 Schematic of PEFC system.

As mentioned above, Pt nanoparticles with a particle size of about 3 to 5 nm are commonly used to provide and react easily to hydrogen and oxygen gases. Carbon supports with a large specific surface area are usually used [8-9]. Oxygen adsorption, dissociation, and desorption are rate-determining steps at Pt used at the cathode, but FC uses expensive Pt as a catalyst because of its fast reaction rate.

Recent advanced analytical techniques are expected to be used to elucidate and provide strategies for catalytic design [10-12]. Pt is known as an expensive precious metal, but the amount of Pt currently used in FC vehicles is said to be several tens of grams. This means that Pt catalysts cost more than 100,000 yen per FC vehicle. Therefore, reducing the amount of Pt use (high activation of Pt catalyst) is an urgent issue [9,13].

1.3 Oxygen reduction reaction (ORR)

1.3.1 Mechanism of ORR

The ORR reaction mechanism has been studied extensively in the past, including single-crystal studies since the 1980s, kinetic studies on four-electron reduction since the 1970s, and computational studies since the 2000s, which have proposed several models involving multi-step intermediates. The mechanism of the oxygen reduction reaction at Pt (eq. 1.2) is explained by a kinetic reaction in which oxygen dissociated and adsorbed on the metal surface reacts with hydrogen and is sequentially reduced to water. Although various studies have been carried out, the reports compiled by Wroblowa are prominently available [14]. **Figure 1-2** shows the ORR pathway proposed by Wroblowa in 1976. He used rotating ring-disk electrode voltammetry based on an estimate of the ORR rate constants. k_1, k_2, and k_3 are rate constants that correspond to a four-electron reduction of O_2 to H_2O, two-electron reduction of O_2 to H_2O_2, and two-electron reduction of H_2O_2 to H_2O, respectively. The ideal reaction pathway (k_1) is that oxygen is adsorbed on Pt and the four-electron reduction process proceeds, but two-electron reduction processes (k_2, k_4) have also been proposed. The mechanism related to this kinetics depends on experimental conditions such as the electrolyte, and not all have been elucidated at present, but it is important to control the reaction rate of absorption and desorption of oxygen on Pt.

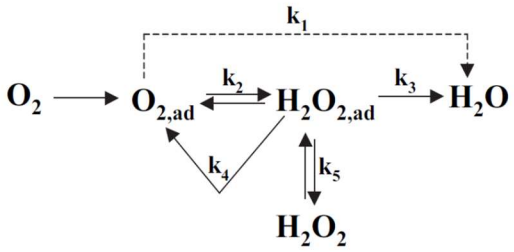

Figure 1-2 General kinetic scheme of ORR. [14]

From Fig. 1-2, general ORR reaction may be described as follows:

The direct four-electron reduction reaction

$$O_2+4H^++4e^-\rightarrow H_2O \qquad E^o=1.23 \text{ V vs. SHE} \qquad (1.4)$$

And two-electron reduction reaction

$$O_2+2H^++2e^-\rightarrow H_2O_2 \qquad E^o=0.68 \text{ V vs. SHE} \qquad (1.5)$$

There is also a report that H_2O_2 generated by two-electron reduction (1.5) decreases cell voltage, and deteriorates the polymer electrolyte membrane [15].

1.3.2 Factors contributing to the ORR

Pt nanoparticle catalysts are widely used due to their relatively low overpotential at FC operation. The chemical reaction of ORR depends on the O_2 adsorption energy, the dissociation energy of bound O-O, and the binding energy of OH on Pt. Stamenkovic et al explained the principle of high activity of Pt alloys in terms of the electronic states of metals and oxygen by density functional theory (DFT) calculation [16]. **Figure 1-3** shows the formation of bonding and antibonding orbitals by hybridizing the oxygen 2p and 5d bands of Pt(111). Here, the vertical axis is energy (ε_F = Fermi level). The strength of the surface oxygen-metal bond depends on the strength

of the covalent bond between the oxygen 2p and d orbitals of the transition metal. This bond splits into an antibonding orbital and a bonding orbital, but the bonding orbital is occupied by electrons, and the occupancy of the antibonding orbital depends on the metal surface. Oxygen adsorption energy depends on the position of the d-band center. In the case of metal, the degree of occupancy is determined by their relative relationship to the Fermi level in the d state. When the d state shifts upward considering the Fermi level, the antibonding state also shifts upward, reducing the occupancy of the antibonding orbital, resulting in stronger Pt-O bonds, and oxygen desorption becoming a rate-determining step. They also confirmed that the d-band center values obtained by this DFT calculation were in good agreement with the experimentally obtained trends in catalytic activity determined by electrochemical measurement.

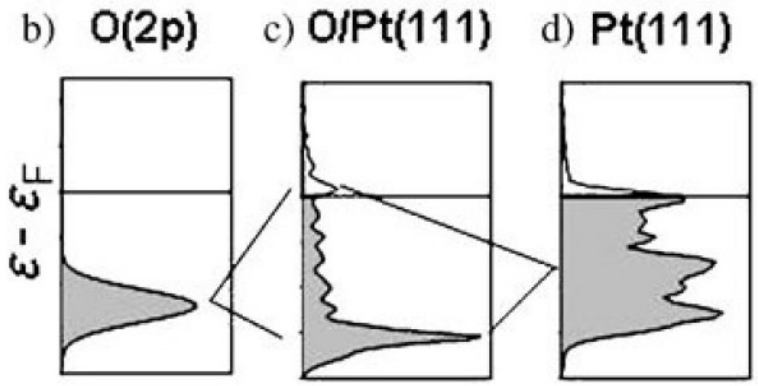

Figure 1-3 The density of states for O (2p) orbital, Pt (5d) orbital, and their coupling orbital O/Pt. [16]

In **Figure 1-4**, the vertical axis shows the dissociation and the adsorption energy of oxygen to some metal surfaces, the horizontal axis shows the binding of OH as an

intermediate, and the ORR activity in the contour line direction. The strength of the bond between the metal surface and O and OH is not too strong and not too weak, indicating that a region in which both the adsorption and desorption of the reactants on the metal surface proceed are preferable. From this figure, it can be seen that Pt has the best ORR activity. This idea corresponds to the idea proposed by Sabatier in the field of catalysts [17,18].

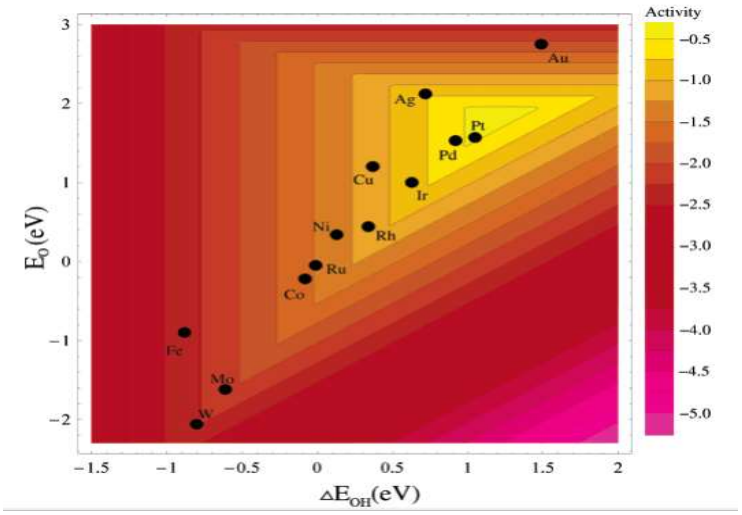

Figure 1-4 A contour plot, which shows the dissociative adsorption of oxygen on Pt on the vertical axis, the binding of OH as an intermediate on the horizontal axis, and the ORR activity in the contour direction, calculated from the free energy [17].

1.4 Various candidates for next-generation catalyst

There are many excellent reviews, especially edited by T. J. Schmidt et al., which are very easy to understand [19]. The following (a) to (h) have been proposed for highly active Pt (reduction of Pt usage) catalysts as shown in **Table1-2**. (a) Alloy: Metals such as add Co, Ni, or Fe are added to Pt fine particles to improve the catalytic activity [20-

22], (b) Core-shell: Replaces metal elements in catalyst particles that do not directly contribute to the catalytic reaction with metals other than Pt [23-25], (c) Crystal orientation: Control of catalyst surface [26-27], (d) Metal oxides: Convert or mix with Pt catalysts [28-30]. (e) A new structure that is not bound by the structure of nanoparticles [31-32]. (f) Metal oxide [33-36], (g) Metal complex [37-41], (h) Carbon material [42-49], etc.

However, each candidate has challenges in industrial use. (a) In the alloy, the additive element on the surface of the catalyst fine particles is dissolved, and there is a concern about the durability of the catalyst [50]. (b) It is technically difficult to control the core-shell structure of the core-shell. (c) Durability is a concern in controlling the crystal plane. (d) Metal oxides do not contribute much to reducing usage, but they do contribute to durability. (e) The development of catalysts with new structures requires special equipment to produce catalysts. The non-Pt-based catalysts (f), (g), and (h) are very attractive materials, but they have low catalytic activity and are currently less active with respect to Pt catalysts [33-49]. From an industrial perspective, the development schedule for these candidate catalysts was reviewed by workers in Ballad Power Systems in 2017. **Figure 1-5** shows the development schedule for various candidate Pt-based catalysts. The core-shell catalyst has the potential to significantly reduce the amount of Pt used in the Pt catalyst, but there are still issues that must be challenged for practical use, and the principle of expressing the catalytic activity of the core-shell catalyst is understood and controlled. That is useful for the industrial

production of core-shell catalysts [51].

Table 1-2 Various candidates for next generation catalyst.

Classification	Approach	Model Structure	Example of synthesis method	Example of references
Pt-based	(a) Alloy	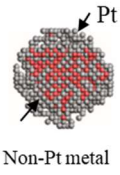	Thermal treatment	20-22
	(b) Core-Shell	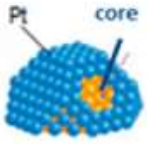	Electro-deposition	23-25
	(c) Orientation	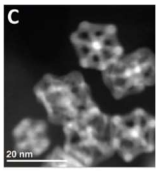	Acid reaching Capping	26-27
	(d) Metal oxide	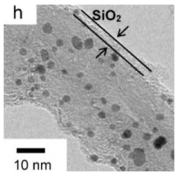	Sol-gel	28-30
	(e) Others	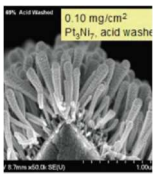	Sputter	31-32
Non-Pt-based	(f) Metal	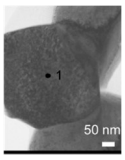	Thermal treatment Acid washing	33-36
	(g) Metal complex	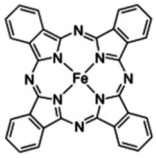	Thermal treatment	37-41
	(h) Carbon	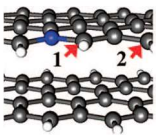	Thermal treatment Acid washing	42-49

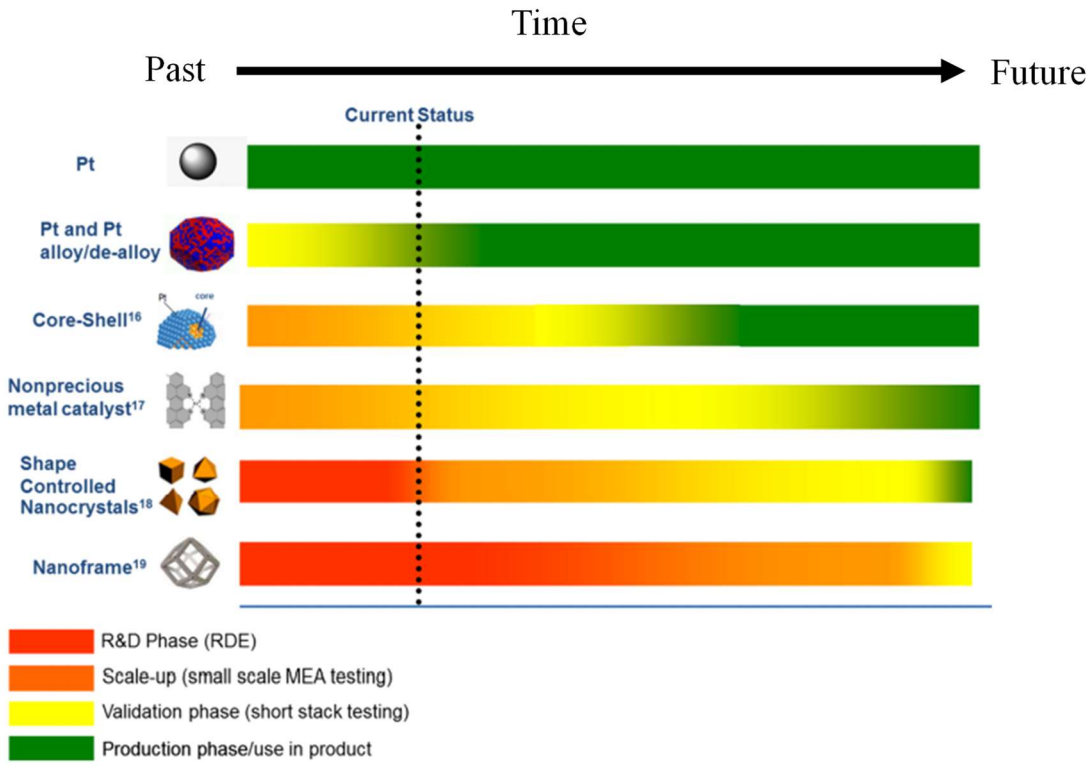

Figure 1-5 Development schedule for various candidate Pt-based catalysts. [51]

1.5 Pt alloy catalyst

Pt alloy catalysts have been studied as a catalyst to improve ORR activity, and have attracted much attention for PEFC applications, about 20 years after the study of Pt catalysts mentioned above. As with Pt alone, many studies have been conducted using kinetics and calculations, including model electrodes by a group at the University of Yamanashi in Japan, and the work of Argonne National Laboratory.

As an example of the research on the ORR reaction mechanism, Toda et al. showed that the electronic state of the Pt film is affected by the electronic state of the underlying alloy and is in a higher valence state (5 d electron deficit) than that of Pt alone, as shown in **Figure 1-6** [52]. They have insisted that the -O bond strength, and that once Pt d-electron back-donation occurs, the first rate-limiting electron transfer (reaction (b) in Fig.1-6), H^+ addition, and O-O bond cleavage is promoted, leading to accelerated ORR.

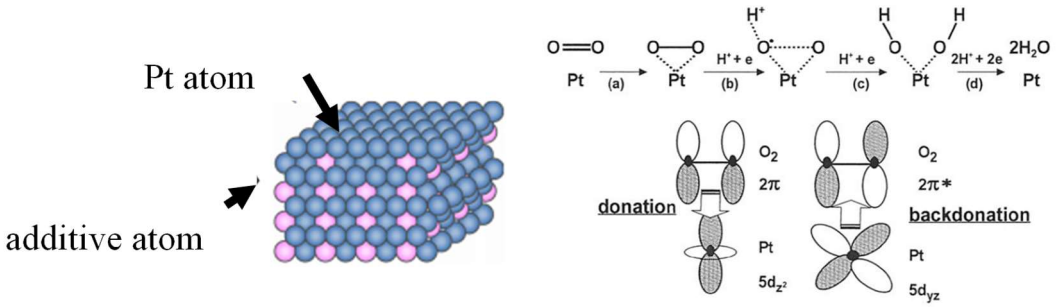

Figure 1-6 Schematic diagram of Pt alloy plate (left) and schematic diagram of ORR reaction mechanism on Pt surface where Pt alloy accelerates ORR activity (right). [52]

The mechanism of the enhanced activity of alloying depends on the research group, and the mechanism has not been standardized. From calculations and experiments, it

has been explained that the optimization of the 5d d-band center of Pt is effective in accelerating the ORR, and PtCo and PtNi are promising for high activity as shown in **Figure 1-7** [16].

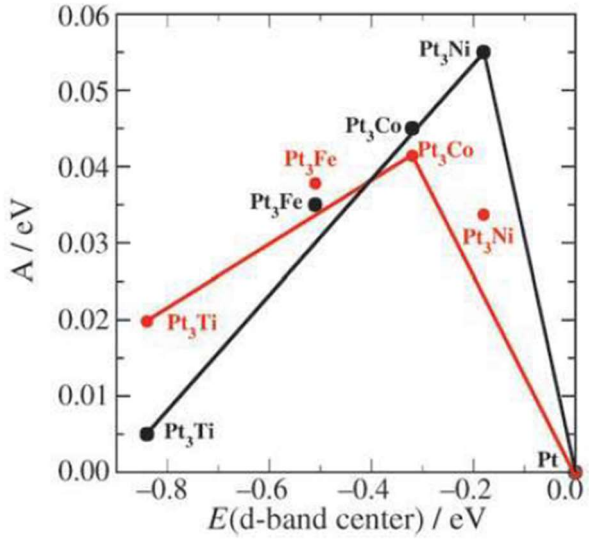

Figure 1-7 ORR activity vs. the experimentally measured d-band center relative to platinum. The activity predicted from DFT simulations is shown in black, and the measured activity is shown in red. [16]

In particular, in the nanoparticle state, as shown in the schematic diagram and the elemental distribution in **Figure 1-8**, due to the preparation method of the nanoparticles, the ideal structure with a regular arrangement of Pt atomic layers proposed in the model electrode has not been realized [53].

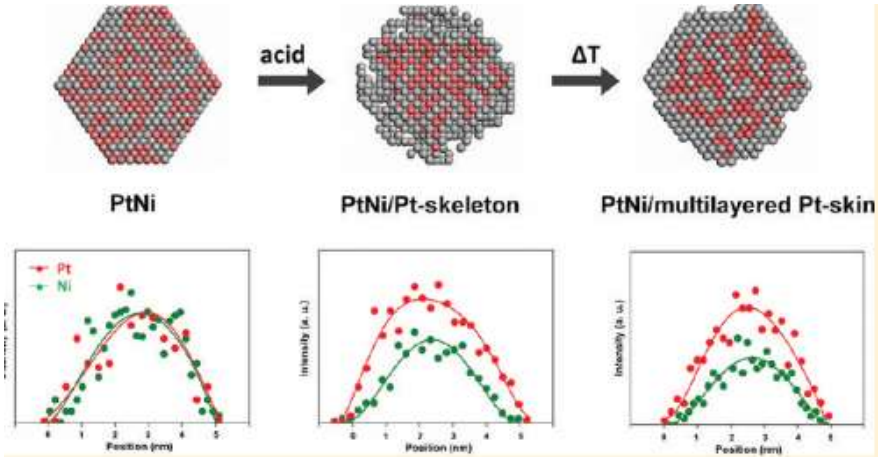

Figure 1-8 Schematic diagram of PtNi alloy nanoparticle catalyst (top) and its elemental distribution measured by EDS line analysis (Pt(red) and Ni(green) elements, respectively).[53]

1.6 Core-shell catalyst

The concept of structurally controlling Pt atomic layers on top of different elements as an approach to an ideal ordered structure has already been studied in the alloy studies described above. It was first reported in 2004 that the Pt atomic layers are electrochemically controlled on Pd (111) as a model electrode [23]. In **Figure 1-9**, as shown in the electrochemical properties on the left and the surface image of the scanning tunneling microscope, Cu was electrochemically deposited one layer on Pd and then replaced with Pt elements to deposit one layer of Pt atoms. Later, the same research group extended the technique to not only Pd but also elements such as Au, Ir, Rh, and other elements that can form a face-centered cubic lattice structure in which Pt atomic layers are epitaxially deposited [54].

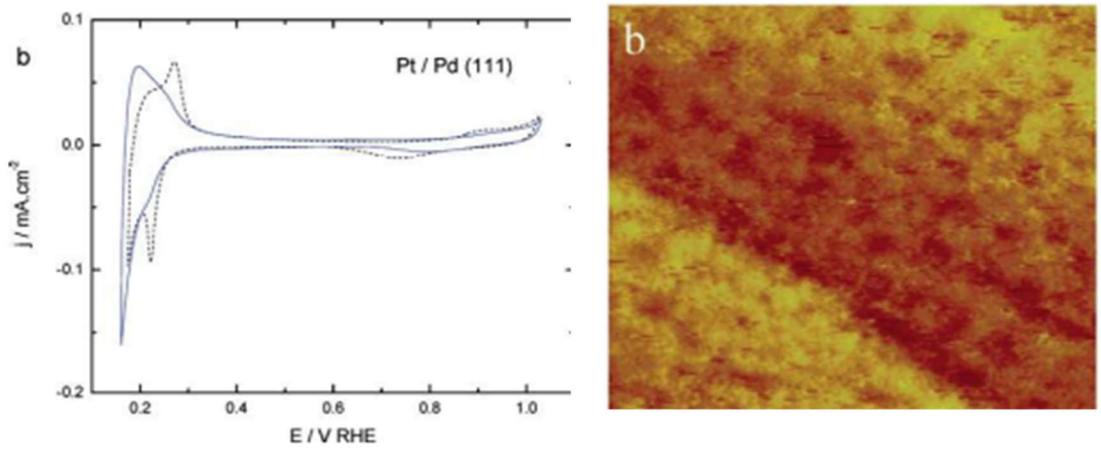

Figure 1-9 Cyclic voltammograms of Pt/Pd(111) (blue line) and Pd(111) (black line) single crystals (left) and surface atomic images by scanning tunneling microscopy (right). [23]

As shown in the next section, we are also studying the coating of Pt atomic layers on nanoparticles by applying this technology to model electrodes. This is called a core-shell catalyst. Here, based on the elemental distribution of Pt and Pd by local analysis using transmission electron microscopy, it is claimed that a Pt atomic layer is formed in the previous study. Core-shell catalysts are, in a broad sense, an extension of alloy catalysts, the definition of which is ambiguous by the authors of the paper. Pt skin catalysts and Pt skeleton catalysts have been proposed as core-shell similar structures, and catalyst particles in which Pt is concentrated on the outermost surface, although not epitaxial growth with respect to the underlying core metal, are also expressed as core shells [53].

Figure 1-10 shows the reasons why core-shell catalysts and Pt atomic layer

technology are used as catalysts. The core metal species is also shown in the calculations and experiments. In the model electrode, Pt on Pd(111) is reported to be 1.3 times more active than pure Pt(111) due to the optimization of the Pt d-band center [54].

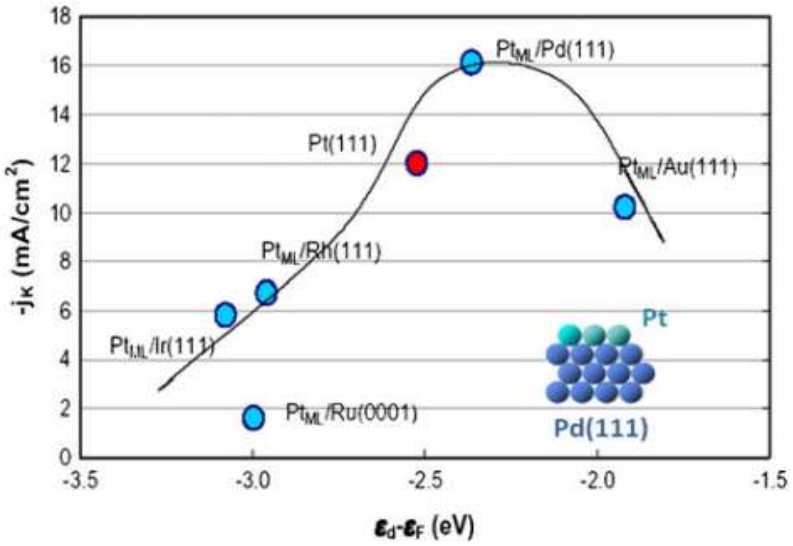

Figure 1-10 Relationship between activity and d-band centers of Pt atomic layers on various single crystals. The vertical axis shows the ORR activity and the horizontal axis shows the d-band center calculated from the DFT calculation.[54]

In the following, I will introduce two methods, the electrodeposition method, which is a typical synthesis method for core-shell catalysts, and the characteristic hydrogen sacrificial protection method. Also, I will discuss the electrochemical properties that have been carried out so far.

1.6.1 Electrodeposition method

The well-known electrodeposition method is the under potential deposition method

(UPD). The UPD method is a method in which Cu is electrochemically deposited on the core-catalyst particles and Cu and Pt are replaced by using the redox potential difference. Sasaki et al. reported an excellent review for the UPD method [55].

Figure 1-11 shows a schematic diagram of the core-shell catalyst synthesis procedure using the UPD method. As shown in Fig. 1-8, firstly, Pd nanoparticles are synthesized. In the second step, the electrochemical potential (for example, 0.3V vs. RHE) is applied to the Pd nanoparticles in a solution containing Cu^{2+} to form a Cu monolayer on the Pd. The Pt monolayer can then be deposited on the Pd nanoparticles by performing a substitution reaction between the Pt precursor solution and Cu on Pd.

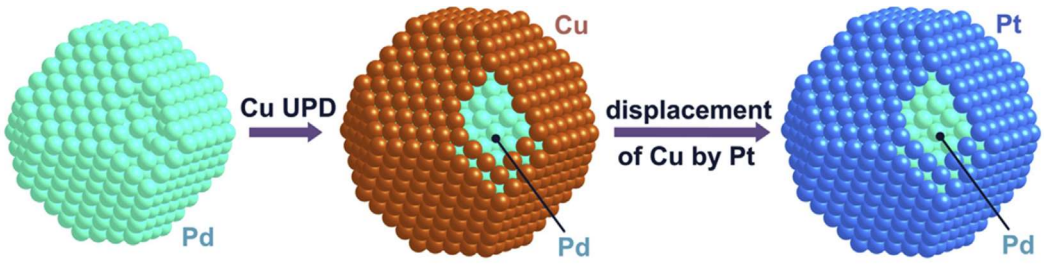

Figure 1-11 Schematic diagram of galvanic displacement of Pt/Pd/C by UPD method. [55]

The structure of core-shell catalyst is characterized by TEM-EDX, XAFS, XRD, XPS etc. [10-11,23-35,55-57] They have shown core-shell structure was successfully formed and their d-band center was shifted by tensile or compressive stresses on the substrate. **Figure 1-12** shows the HAADF-STEM image and EDS line profile for Pt/Pd

nanoparticles. It was found that (i) Pt atoms completely covered the surface of the Pd nanoparticles, (ii) Pt intensity was low and constant at the center of the Pd nanoparticles, and (iii) Pt intensity at both edges of the nanoparticle is stronger than the Pt intensity at the center part of the particle [57].

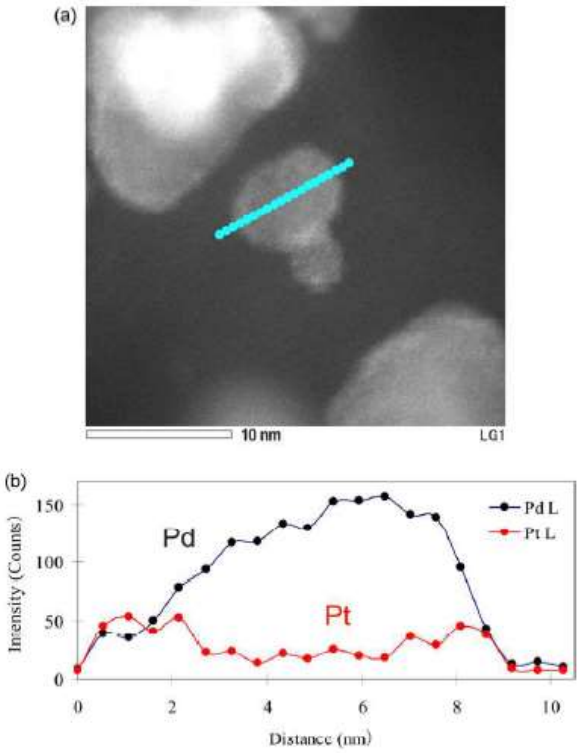

Figure 1-12 HAADF-STEM image and EDS line profiles of Pt/Pd nanoparticles. [57]

They have also evaluated electrochemical properties such as CV and ORR. **Figure 1-13** shows a linear sweep voltammogram (LSV) of the Pt/Pt nanoparticles in ORR. The oxygen reduction reaction began with a high onset potential at 0.95-1 V vs. RHE. They estimated that the activity of Pt/Pd/C (0.57 A/mgPt) was three times higher than that of Pt/C (ca. 0.2 A/mgPt) calculated from the Koutecky-Levich plot.

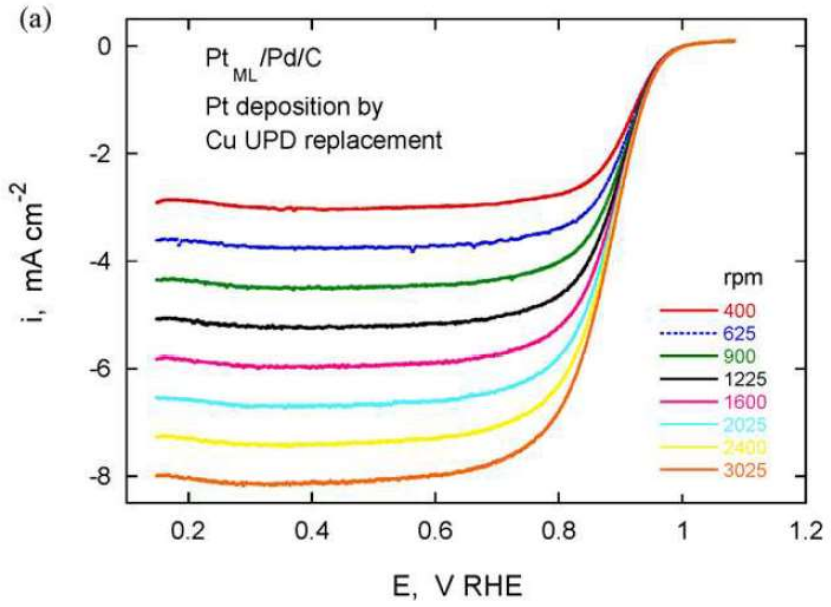

Figure 1-13 Liner sweep voltammogram of the Pt/Pd nanoparticles measured by RDE in oxygen saturated 0.1 M $HClO_4$. Sweep rate was 10 mV/s. [57]

Many papers report the structural and electrochemical properties of this UPD method. For example, the electrochemical properties of CV, ORR, and PEFC single cells (MEA) have been evaluated and their performance is superior to conventional Pt/C [10-11,23-35,55-57].

Although the UPD method is academically superior method including the design concept, it is a commercially multi-step process and a complex process that makes it difficult to completely coat platinum. For example, potential control is required, and there is concern about contamination by impurities such as Cu. The impregnation method is the same as the UPD method, and since the core metal fine particles are supported on the carbon, it is considered that Pt is not coated on the interface between the metal fine particles and the carbon supports. From these points, this method may

require very severe parameters to control for industrial applications.

1.6.2 Hydrogen sacrificial protection method

Compare to the UPD method, there are few reports on the hydrogen sacrificial protection method. It is said that the hydrogen sacrificial protection method is a relatively simple process because there is no potential control required and there is no risk of impurities being mixed in compared to the UPD method [58-59]. Therefore, it is advantageous for industrial applications. The hydrogen sacrificial protection method was reported by Toshima et al. in 1997, and a mechanism for estimating the Pt deposition process on nanoparticles was proposed [58]. **Figure 1-14** shows a hydrogen sacrificial protection strategy for preparing bimetal colloids with a core-shell structure. Pd has the ability to adsorb and split hydrogen from metal-H bonds on its surface (process an in fig. 1-14). The hydrogen atom adsorbed on Pd has a very strong reducing ability, implying a very low redox potential. Hydrogen-adsorbed Pd nanoparticles promote the completeness of additionally charged Pt ions and selectively form a Pt layer on Pd nanoparticles [58]. First, hydrogen is absorbed on Pd nanoparticles (fig. 1-14a), followed by electron reduction of Pt ions and redox reaction of protons on the surface of Pd (fig. 1-14b-c). Finally, the desired reaction proceeds on Pt/Pd (Fig. 1-14d).

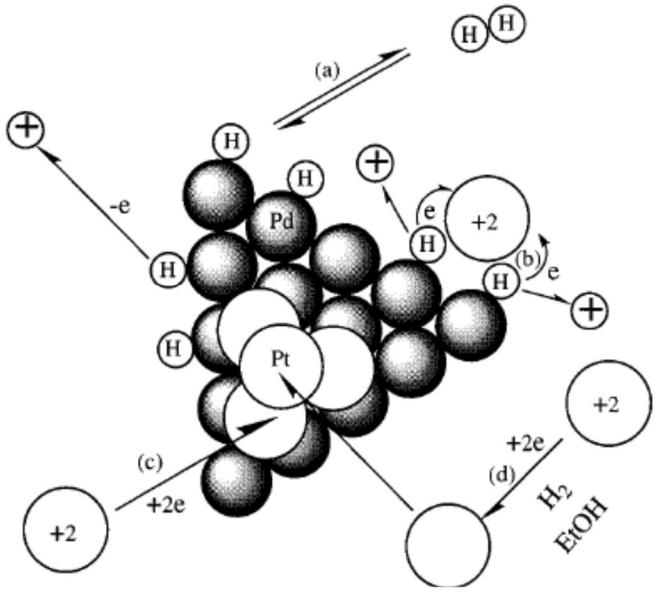

Figure 1-14 Hydrogen-sacrificial protection strategy for the preparation of bimetallic colloids with a core/shell structure. [58]

However, nanoparticles are generally complex, and multiple factors make it difficult to interpret the principle, including size effect (surface area), surface contamination (colloidal protective agents), and aggregation of catalytic particles. Regarding the hydrogen sacrificial protection method, there is no report that quantitatively discusses the relationship between the Pt precipitation mechanism and the electrochemical properties (FC properties) in principle.

Further research was carried out in 2011, and Naohara and Toshima investigated Pt/Pd catalysts using the hydrogen sacrificial protection method and perfluorosulfonic acid as a colloidal protective agent for FC catalyst applications [59]. **Figure 1-15** shows HAADF-STEM images and EDS line profiles for Pt/Pd perfluorosulfonic acid copolymers protected nanoparticles synthesized by the hydrogen sacrificial protection

method. These STEM images and EDS line profiles show the localization of Pt on Pd core nanoparticles.

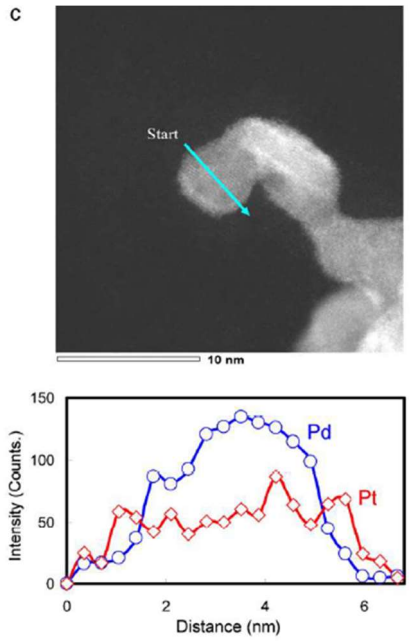

Figure 1-15 HAADF-STEM image and EDS line profiles of Pt/Pd- perfluorosulfonic acid copolymers protected nanoparticles. [59]

They also evaluate electrochemical properties such as CV and ORR. **Figure 1-16** shows the LSV of Pt/Pd nanoparticles protected with a perfluorosulfonic acid copolymer. The oxygen reduction reaction began with a high onset potential at 0.95-1 V vs. RHE. They estimated that the activity of Pt/Pd perfluorosulfonic acid copolymer protected nanoparticles (0.34 A/mgPt) was twice that of Pt/C from the Koutecky-Levich plot.

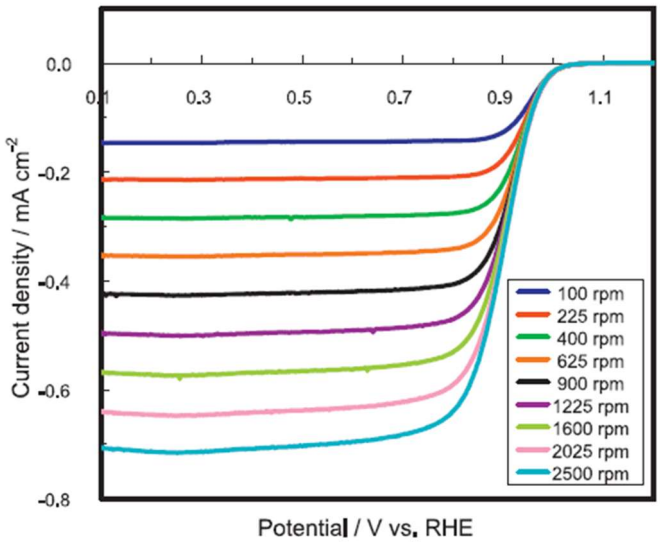

Figure 1-16 Liner sweep voltammograms of Pt/Pd perfluorosulfonic acid copolymer protected nanoparticles measured in oxygen saturated 0.1 M $HClO_4$ solution. Sweep rate was 10 mV/s. [59]

However, these previous papers are limited to electrochemical evaluation (oxygen reduction characteristics by RDE), and there are no reports on power generation characteristics or catalyst design guidelines when MEA is constructed as FC.

On the other hand, Brookhaven Science Associates holds and publishes a patent including a core-shell catalyst in which Pt is deposited using hydrogen-adsorbed Pd similar to the hydrogen scarification method. However, the structure of the catalyst and the principle of expression of its catalytic activity has not been studied academically. [60].

In the hydrogen sacrificial protection method, core nanoparticles (Pd) are produced by colloidal synthesis and a surfactant is used. Colloidal synthesis provides

nanoparticles (NPs) with controlled composition and structural characteristics Polyvinylpyrrolidone (PVP) has been used to obtain such nanostructures. PVP acts as a surface stabilizer, growth modifier, nanoparticle dispersant, and reducing agent [61]. Colloidal nanoparticles prepared by solution synthesis that control particle size, shape, composition, and structure shown great potential for catalytic applications. However, such colloidal nanoparticles are usually capped with organic ligands (as surfactants) and cannot be used directly as a catalyst. Li et al., studied the effect of surfactant removal on the electrocatalytic performance of Pt nanoparticles produced by organic solution synthesis [62]. Various methods such as thermal annealing, acetic acid washing, and UV-ozone irradiation were applied to remove the oleylamine surfactant, and the treated nanoparticles were applied as electrocatalysts for the ORR. Regarding binary alloy catalysts, there are reports of PtAu, PtRe, PtCo, etc., and although it depends on the type of surfactant, it is generally heat-treated at about 200 to 400 °C [63-68]. However, no one has discussed the residual amount of PVP before and after heat treatment, the detailed structural analysis, and electrochemical properties of the Pt/Pd core-shell structure.

1.7 Characterization method for model catalysts and core-shell nanoparticle catalyst

Traditionally, TEM observations have often been used for characterization because the core-shell structures have a sub-nanometer Pt thickness relative to the shell structure

[10-11,23-35,55-57]. In this paper, the relationship between the physical properties of the core-shell catalyst and the electrochemical properties including the fuel cell was systematically clarified, using a multifaceted analysis method using a model structure and a nanoparticle structure. This section describes non-TEM characteristic analysis methods. Next, this paper introduces electrochemical and spectroscopic methods that are effective in identifying characteristic surface chemical species. In this study, the catalytic structure was identified in the following ways: (a) Electrochemical quartz crystal microbalance method (EQCM) that can quantitatively evaluate the amount of Pt deposition on Pd polycrystalline for fabrication of model catalysts. (b) Angle-resolved X-ray photoelectron spectroscopy (AR-XPS) that can estimate Pt thickness on Pd. (c) Surface-enhanced infrared absorption spectroscopy (SEIRAS) that can be used for the analysis of catalyst surface structure. The principles of these methods will be described.

1.7.1 Electrochemical quartz crystal microbalance (EQCM)

There are various types of crystal oscillators, but it is a crystal oscillator in which electrodes are formed on both sides of a quartz plate thin film. **Figure 1-17** shows a schematic diagram of the QCM mass sensor.

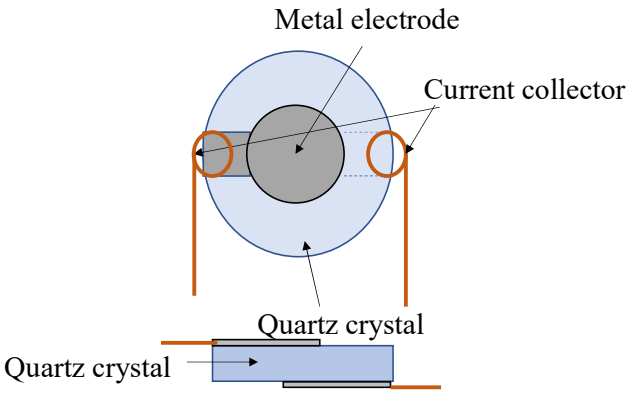

Figure 1-17 Schematic diagram of QCM mass sensor (top: front view, bottom: cross-sectional view).

It slides horizontally with respect to the surface and vibrates. The frequency of the crystal oscillator at this time is determined by the thickness of the crystal, and if a thin crystal plate is used, a crystal oscillator that vibrates at a higher frequency can be obtained. It was reported that the frequency of this quartz plate changes depending on the mass of the substance on the electrode. The relationship between the amount of change in frequency and the mass of adhering substances is expressed by the following equation called the Sauerbrey equation (1.6).

$$\Delta F = -\frac{2{F_0}^2}{\sqrt{\rho_Q \mu_Q}} \frac{\Delta m}{A} \tag{1.6}$$

ΔF: Frequency change, Δm: Mass change, F_0: Fundamental frequency, ρ_Q: Crystal density, μ_Q: Crystal shear stress, A: electrode area

As the amount of deposits increases, the frequency decreases, and as the amount

of deposits decreases, the frequency increases. The method of detecting the frequency change of the crystal oscillator using this phenomenon and measuring the mass change of the substance on the electrode is called the quartz crystal microbalance (QCM) method.

This QCM principle was applied to electrochemistry by Bruckenstein et al. [69] **Figure 1-18** shows a typical electrochemical cell equipped with a QCM. This measurement method is called an electrochemical quartz crystal microbalance (EQCM). It is possible to observe in-situ mass changes related to electrode adsorption/desorption species that occur during an electrochemical reaction by connecting the oscillator to the electrochemical cell. The metal on the quartz crystal is used as the working electrode. The metal surface is in contact with the electrolyte, and the electrode reaction proceeds at this interface. Counter and reference electrodes are also connected to the electrochemical cell. It is also possible to estimate the electrochemical reaction from the amount of reacted charge and the change in the mass of the electrode. The slope of Δm vs Q plot is called the mass per electron (mpe). Mpe is calculated by the following equation (1.7).

$$mpe = \frac{\Delta m \cdot F}{Q} \tag{1.7}$$

Δm: Mass change, F: Faraday constant, Q: reaction charge

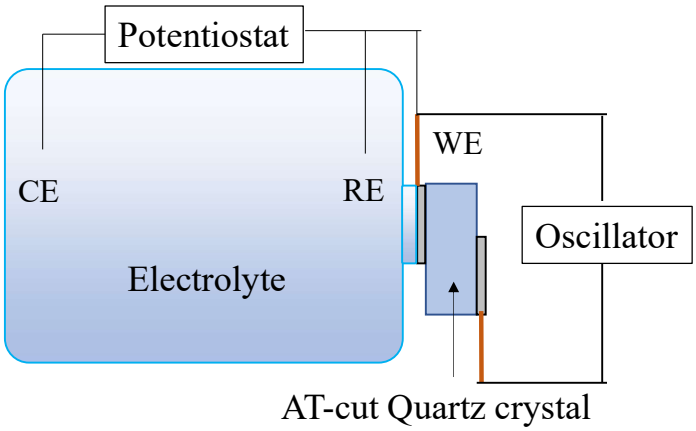

Figure 1-18 Schematic diagram of typical electrochemical cell equipped with QCM.

The formation of Pt oxide species and the deposition of Pd on Au(111) substrate was quantitatively investigated by this method combined with CV and other methods [70-71]. Shimazu et. al. studied the adsorption of water on a Pt polycrystalline electrode and discuss the species adsorbed in H_2SO_4 solution using CV. Naohara et. al. also studying the thin layer deposition of Pd on Au(111), its Pd formation mechanism, and electrochemical properties of Pd on Au(111) in acid solution.

1.7.2 Angle-resolved X-ray photoelectron spectroscopy (AR-XPS)

X-ray photoelectron spectroscopy (XPS) is a very well-known technique for identifying surface chemical species. When the sample surface is irradiated with X-rays under an ultra-high vacuum, photoelectrons are emitted from the surface into the vacuum due to the photoelectric effect. It is possible to obtain information on the elemental composition and chemical state of the surface by observing the kinetic energy of the photoelectrons.

$$E_b = h\nu - E_{kin} - \Phi \quad (1.8)$$

Where, E_b is the binding energy of bound electrons, $h\nu$ is the energy of soft X-rays, E_{kin} is the kinetic energy of photoelectrons, and φ is the work function of the spectroscope.

The thickness of the multi-layered surface coating is estimated by angle-resolved XPS measurement [72]. **Figure 1-19** shows a schematic diagram of an example of AR-XPS arrangement.

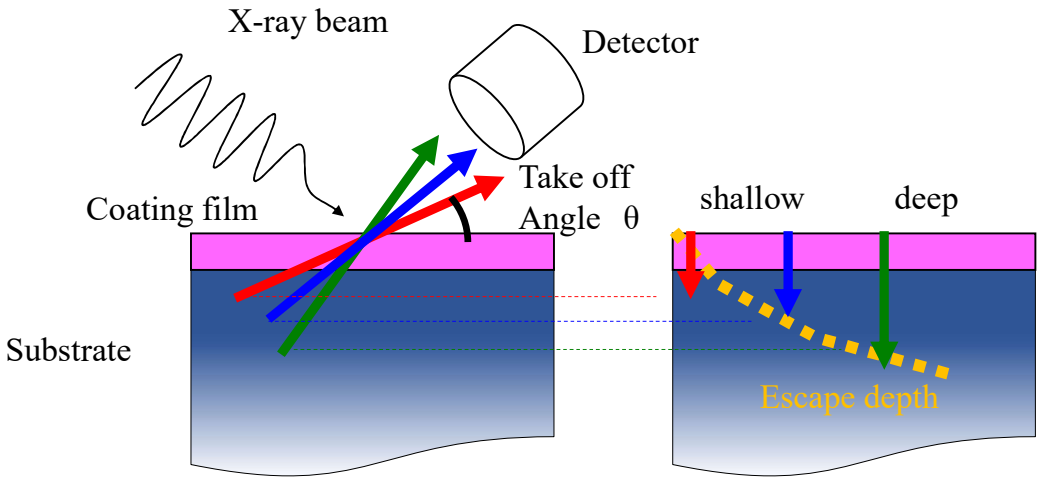

Figure 1-19 Schematic diagram of AR-XPS arrangement.

Surface element and chemical states were estimated using AR-XPS. A more quantitative analysis can be performed by using the relationship between the XPS signal intensity from the substrate covered with a thin-film and take-off angle θ, as following equation (1.9).

$$\ln(\mathrm{I}) = \frac{-d}{\lambda sin\theta} + \ln\,(I_o) \quad (1.9)$$

The thickness of the surface thin film can be estimated by eq. (1.9) because I/I_0 and $\lambda sin\theta$ can be calculated. Here, I_0 and I represent the signal intensity on a bare substrate and a substrate covered with a thin film of thickness d, respectively, and λ is the mean free path of photoelectrons in the thin film. According to eq. (1.8), $ln(I)$ must be linearly related to $1/sin\ \theta$ with a slope of (d/λ) and an intercept of $ln(I_0)$ [72]. Fukumitsu et al reported organic molecules on Si(111) by AR-XPS. They estimated the thickness of organic molecules from eq. (1.9).

1.7.3 Surface enhanced infrared spectroscopy (SEIRAS)

Metal particles (nanoparticles) smaller than the wavelength of incident light are typical active substrates for surface enhanced spectroscopy. **Figure 1-20** shows a schematic diagram of the enhanced electric field. Fine particles are polarized (p or δp) by plasmon excitation by incident light, and a strong electric field is formed around them. This strong electric field excites the vibration of the adsorbed molecules and interacts with the metal particles at close range. As a result, the transmittance and reflectance of the metal thin film change significantly with the frequency of molecular vibration. The vibration of the adsorbed molecule is observed through the infrared absorption change of the metal fine particles, and the metal fine particles act as an infrared absorption amplifier [73].

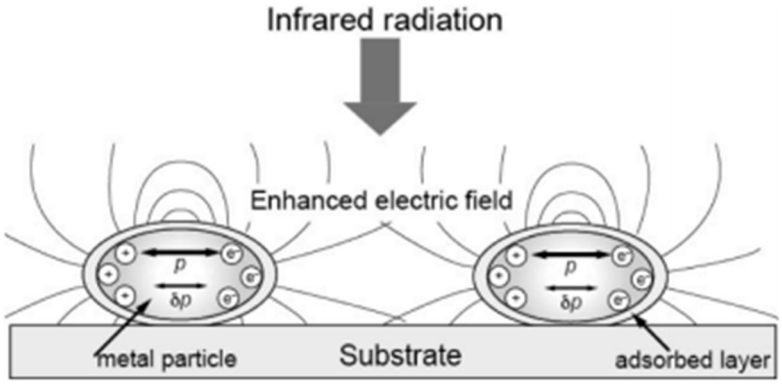

Figure 1-20 Schematic diagram of the enhanced electric field. [73]

Figure 1-21 shows a schematic of the electrochemical cell equipped with SEIRAS. IR beam is emitted in an ATR arrangement in which the light is incident from the back surface of the Si prism. As a metal thin film on Si prism as the working electrode, the counter electrode, and the reference electrode are used to proceed the electrochemical reaction. If an additive to the electrolytic solution or gas replacement is required, it can be done in the same as a conventional electrochemical reaction system. By measuring the reactants on the electrode surface while the electrochemical reaction is in progress, it becomes possible to consider the reaction mechanism.

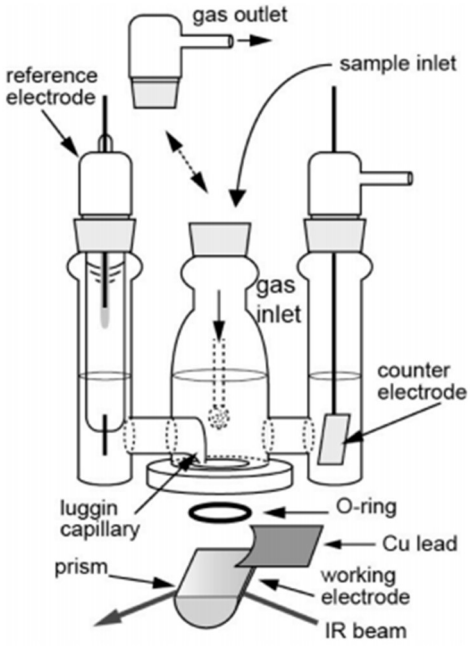

Figure 1-21 Schematic diagram of the electrochemical cell for SEIRAS measurement. [73]

Y. G. Yan et al reported molecular adsorption and reactions to industrially important transition metals by ATR-SEIRAS. They succeeded in in-situ analysis of the oxidation behavior of CO at Pt and Pd regarding the oxidation reaction of methanol [74]. They have shown the major CO bands for electrodeposited Pd, Pt, Rh, and Ru. It was experimentally confirmed that the CO band on the above metal is mainly the bridge site in the case of Pd and the on top site in the case of Pt by using CO as the probe molecule. Thus, the physical and electrochemical characteristics peculiar to the surface metal species can be evaluated by using SEIRAS.

1.8 Objective and outline of the present thesis

The theme of this thesis is to propose a new factor that enables the construction of

the topmost Pt atomic layer, which constitutes the core-shell catalyst, and contributes to its improved performance. approaching the construction of the Pt atomic layer from two perspectives, basic and applied research, the structure and properties of Pt/Pd catalysts prepared by hydrogen sacrificial protection method. The strategy was systematically clarified. Since core-shell catalysts were studied by the above two approaches, the usefulness of Pt atomic layers prepared by the hydrogen sacrificial protection method was proved and further extended to the construction of Pt atomic layers on nanoparticles.

As a result, the sufficient conditions for industrial use of core-shell nanoparticles (PEFC operating conditions including durability) were proved.

The structure of this thesis is outlined as follows:

In Chapter 1, the background of the present study was described.

In Chapter 2, the construction of Pt mono- and few atomic layers on Pd polycrystalline electrodes by hydrogen sacrificial protection method and their electrochemical ORR activities were given.

In Chapter 3, the construction of structurally-controlled Pt shell-Pd core catalysts by hydrogen sacrificial protection method was given.

In Chapter 4, the fuel cell performance was demonstrated with the constructed Pt atomic layer.

In Chapter 5, a general conclusion of this thesis and future prospects were given.

1.9 References

(1) International goals for the period from 2016 to 2030 as outlined in the 2030 Agenda for Sustainable Development, adopted at the UN summit held in September 2015.

(2) J. Kupecki, M. Skrzypkiewicz, M. Btesznowski, On the sidelines of the 24th Session of the Conference of the Parties to the United Nations Framework Convention on Climate Change (UNFCCC) - COP24 (2018) December 12th.

(3) New Energy and Industrial Technology Development Organization (NEDO), focus NEDO (2014) 53 1-16.

(4) D. Hart, F. Lehner, S. Jones, J. Lewis, M. Klippenstein, FUEL CELL INDUSTRY REVIEW 2018.

(5) J. Wisniak, Indian Journal of History of Science (2015) 50 (3) 476-490.

(6) L. Giorgi, F. Leccese, The Open Fuel Cells Journal (2013) 6 (1) 1-20.

(7) NEDO, Introduction of NEDO's Activities for Hydrogen and Fuel Cell Technology (2019) 26 February.

(8) Y. C. Park, H. Tokiwa, K. Kakinuma, M. Watanabe, M. Uchida, J. Power Sources (2016) 315 179-191.

(9) M. Watanabe, H. Yano, H. Uchida, D. A. Tryka J. Electroanal. Chem. (2018) 819 359-364.

(10) N. Ishiguro, T. Saida, T. Uruga, S. Nagamatsu, O. Sekizawa, K, Nitta, T. Yamamoto, S. Ohkoshi, Y. Iwasawa, T. Yokoyama, M. Tada ACS Catal. (2012) 2 1319-1330.

(11) X. Wang, Y. Orikasa, Y. Takesue, H. Inoue, M. Nakamura, T. Minato, N. Hoshi,

Y. Uchimoto, J. Am. Chem Soc. (2013) 135 5938-5941.

(12) C. Liu, T. Uchiyama, K. Yamamoto, T. Watanabe, X. Gao, H. Imai, M. Matsumoto, S. Sugawara, K. Shinohara, K. Oshima, S. Sakurai, Y. Uchimoto, ACS Appl. Energy Mater. (2021) 4 810-818.

(13) NEDO, NEDO's Technology Development Roadmap for Fuel Cells and Hydrogen (2017).

(14) H. S. Wroblowa, Y. C. Pan, G. Razumney, J. Electroanal. Chem. (1976) 69 195-201.

(15) M. Inaba, H. Yamada, R. Umebayashi, M. Sugishita, A. Tasaka, Electrochemistry (2007) 75 (2) 207-212.

(16) V. Stamenkovic, B. S. Mun, K. J. J. Mayrhofer, P. N. Ross, N. M. Markovic, J. Rossmeisl, J. Freeley, J. K. Nørskov, Angew. Chem. Int. Ed. (2006) 45 2897-2901.

(17) J. K. Nørskov, J. Rossmeisl, A. Logadottir, L. Lindqvist, J. Phys. Chem. B (2004) 108 17886-17892.

(18) P. Sabatier Ber. Dtsch. Chem. Ges. (1911) 44 1984– 2001.

(19) A. Rabis, P. Rodriguez, T. J. Schmidt, ACS Catal. (2012) 2 864-890.

(20) U. A. Paulus, A. Wokaun, G. G. Scherer, T. J. Schmidt, V. Stamenkovic, V. Radmilovic, N. M. Markovic, P. N. Ross, J. Phys. Chem. B (2002) 106 4181-4191.

(21) K. Okaya, H. Yano, H. Uchida, M. Watanabe, ACS Appl. Mater. Interfaces (2010) 2(3) 888-895.

(22) H. Schulenburg, E. Muller, G. Khelashvili, T. Roser, H. Bonnemann, A. Wokaun,

G. G. Scherer, J. Phys. Chem C (2009) 113 4069-4077.

(23) J. Zhang, Y. Mo, M. B. Vukmirovic, R. Klie, K. Sasaki, R. R. Adzic, J. Phys. Chem. B (2004) 108 10955-10964.

(24) N. Aoki, H. Inoue, A. Shirai, S. Higuchi, Y. Matsui, H. Daimon, T. Doi, M. Inaba, Electrochim. Acta (2017) 244 146-153.

(25) N. Aoki, H. Inoue, R. Yoshiura, Y. Hasegawa, S. Miyazaki, A. Suzuki, H. Daimon, T. Doi, M. Inaba, K. Higashi, T. Uruga, Y. Iwasawa, H. Tanida, Q. Yuan, N. Takao, H. Imai, T. Mikami, A. Daimaru, J. Electrochem. Soc. (2020) 167 044513.

(26) L. Wang, A. Roudgar, M. Eikerling, J. Phys. Chem. C (2009) 113 17989-17996.

(27) K. Miyabayashi, H. Nishihara, M. Miyake, Langmuir (2014) 2936-2942.

(28) L. Zhang, L. Wang, C. M. B. Holt, T. Navessin, K. Malek, M. H. Eikerling, D. Mitlin, J. Phys. Chem. C (2010) 114 16463-16474.

(29) S. Takenaka, H. Miyamoto, Y. Utsunomiya, H. Matsune, M. Kishida, J. Phys. Chem. C (2014) 118 774-783.

(30) K. Fugane, T. Mori, D. R. Ou, P. Yan, F. Ye, H. Yoshikawa, J. Drennan, Langmuir (2012) 28 16692-16700.

(31) P.K. Sinha, W. Gu, A. Kongkanand, E. Thompson, J. Electrochem. Soc. (2011) 158 (7) B831-B840.

(32) N.N. Kariuki, W. J. Khudhayer, T. Karabacak, D. J. Myers, ACS Catal. (2013) 3 (12) 3123-3132.

(33) A. Ishihara, M. Tamura, Y. Ohgi, M. Matsumoto, K. Matsuzawa, S. Mitsushima,

H. Imai, K. Ota, J. Phys. Chem. C (2013) 117 18837-18844.

(34) L. Colmenares, Z. Jusys, R. J. Behm, J. Phys. Chem. C (2007) 111 1273-1283.

(35) R. Ohnishi, K. Takanabe, M. Katayama, J. Kubota, K. Domen, J. Phys. Chem. C (2013) 117 496-502.

(36) J. Seo, L. Zhao, D. Cha, K. Takanabe, M. Katayama, J. Kubota, K. Domen, J. Phys. Chem. C (2013) 117 11635-11646.

(37) F. Jaouen, A. M. Serventi, M. Lefe`vre, J. Dodelet, P. Bertrand, J. Phys. Chem. C (2007) 111 5971-5976.

(38) X. Chen, F. Li, X. Wang, S. Sun, D. Xia, J. Phys. Chem. C (2012) 116 12553-12558.

(39) M. Ferrandon, A. J. Kropf, D. J. Myers, J. Phys. Chem. C (2012) 116 16001-16013.

(40) X. Chen, S. Sun, X. Wang, F. Li, D. Xia, J. Phys. Chem. C (2012) 116 22737-22742.

(41) J. Chlistunoff, J. M. Sansiñena, J. Phys. Chem. C (2014) 118 19139-19149.

(42) J. Maruyama, T. Hasegawa, T. Amano, Y. Muramatsu, E. M. Gullikson, Y. Orikasa, Y. Uchimoto, ACS Appl. Mater. Interfaces (2011) 3 4837-4843

(43) J. Maruyama, I. Abe, Chem. Mater. (2005) 17 4660-4667.

(44) J. Maruyama, I. Abe, Chem. Mater. (2006) 18 1303-1311.

(45) J. Maruyama, J. Okamura, K. Miyazaki, I. Abe, J. Phys. Chem. C (2007) 111(18) 6597-6600.

(46) T. Ikeda, M. Boero, S.F. Huang, K. Terakura, M. Oshima, J. Ozaki, S. Miyata, J.

Phys. Chem. C (2010) 114 8933-8937.

(47) J. Maruyama, J. Okamura, K. Miyazaki, Y. Uchimoto, I. Abe, J. Phys. Chem. C (2008) 112 2784-2790.

(48) T. Ikeda, M. Boero, S. Huang, K. Terakura, M. Oshima, J. Ozaki, J. Phys. Chem. C (2008) 112 (38) 14706-14709.

(49) J. Maruyama, T. Hasegawa, S. Iwasaki, H. Kanda, H. Kishimoto, ACS Sustainable Chem. Eng. (2014) 2 493-499.

(50) Y. Cui, Y. Wu, Z. Wang, X. Yao, Y. Wei, Y. Kang, H. Du, J. Li, L. Ganz, J. Electrochem. Soc. (2020) 167 06452.

(51) D. Banham, S. Ye, ACS Energy Lett. (2017) 2 629-638.

(52) T. Toda, H. Igarashi, H. Uchida, M. Watanabe, J. Electrochem. Soc. (1999) 146 3750-3756.

(53) C. Wang, M. Chi, D. Li, D. Strmcnik, D. Vliet, G. Wang, V. Komanicky, K. Chang, A. P. Paulikas, D. Tripkovic, J. Pearson, K. More, N. M. Markovic, V. R. Stamenkovic, J. Am. Chem. Soc. (2011) 133 36 14396-14403.

(54) R. R. Adzic, Electrocatal (2012) 3 163-169.

(55) K. Sasaki, K.A. Kuttiyiel, R. R. Adzic, Curr. Opin. Electrochem. (2020) 21 368-375.

(56) A. Kongkanand, N. P. Subramanian, Y. Yu, Z. Liu, H. Igarashi, D. A. Muller, ACS Catal (2016) 6 1578–1583.

(57) K. Sasaki, J. X. Wang, H. Naohara, N. Markovic, K. More, H. Inada, R. R. Adzic,

Electrochim. Acta (2010) 55 2645-2652.

(58) Y. Wang, N. Toshima. J. Phys. Chem. (1997) 101 5301-5306.

(59) H. Naohara, Y. Okamoto, N. Toshima, J. Power Sources (2011) 196 7510- 7513.

(60) WO 2006/135396.

(61) K. M. Koczkur, S. Mourdikoudis, L. Polavarapu, S. E. Skrabalak, Dalton Transactions (2015) 41 17883-17905.

(62) D. Li, C. Wang, D. Tripkovic, S. Sun, N. N. Markovic, V. R. Stamenkovic, ACS Catal. (2012) 2 1358-1362.

(63) S. Brimaud, C. Coutanceau, E. Garnier, J.-M. Léger, F. Gérard, S. Pronier, M. Leoni, J. Electroanal. Chem. (2007) 602 2 226-236.

(64) Y. Borodko, S. E. Habas, M. Koebel, P. Yang, H. Frei, G. A. Somorjai J. Phys. Chem. B (2006) 110 23052-23059.

(65) C. Hwang, J. S. Heo, K. Kimb, Y. K. Kanga, B. Choia, Y. Kim, A. Facchetti, S. K. Park, M. Kim, RSC Adv. (2019) 9 730-737.

(66) Z. Liu, C. Yu, I. A. Rusakova, D. Huang, P. Strasser, Top. Catal. (2008) 49 241-250.

(67) D. Raciti, J. Kubal, C. Ma, M. Barclay, M. Gonzalez, M. Chi, J. Greeley, K. L. More, C. Wang, Nano Energy (2016) 20 202-211.

(68) R. Devivaraprasad, N. Nalajala, B. Bera, M. Neergat, Front. Chem. (2019) 7 648.

(69) S. Bruckenstein, M. Shay, Electrochim. Acta (1985) 30 10 1295-1300.

(70) K. Shimazu, H. Kita, J. Electroanal. Chem. (1992) 341 361-367.

(71) H. Naohara, S. Ye, K. Uosaki, J. Phys. Chem. B (1998) 102 4366-4373.

(72) H. Fukumitsu, T. Masuda, D. Qu, Y. Waki, H. Noguchi, K. Shimazu, K. Uosaki, Chem. Lett. (2010) 39 768-770.

(73) T. Uchida, M. Osawa, Review of Polarography (2016) 62 2/3 93-100.

(74) Y. G. Yan, Q.X. Li, S.J. Huo, M. Ma, W.B. Cai, M. Osawa J. Phys. Chem. B (2005) 109 7900-7906.

Chapter 2

CONSTRUCTION OF Pt MONO-AND FEW ATOMIC LAYERS ON Pd POLYCRYSTYALLINE ELECTLODES BY HYDROGEN SACRIFICIAL PROTECTION METHOD AND THEIR ELECTROCHEMICAL ORR ACTIVITIES

2.1 Introduction

Core-shell catalysts for fuel cells have been studied by many researchers as candidates for platinum reduction technology [1-9]. Core-shell catalyst have more than two layers on top of core particles, the surface layers of which are less than the nanometers. Pd was proposed as a candidate for core particles because the Pt monoatomic layer on the Pd core nanoparticles can optimize oxygen absorption /desorption energy by compressing the Pt interatomic distance and improve the oxygen reduction reaction (ORR) [1-2,4-5]. However, these traditional studies have focused on the electrochemical deposition (under potential deposition) method proposed by Adzic's group [1-2,9].

On the other hand, the hydrogen sacrificial protection method proposed by Toshima's group has an industrial advantage in manufacturing catalysts because it does not require potential control, impurities, or simple procedures compared to the conventional electrochemical deposition method [3]. However, in the case of the hydrogen sacrificial protection method, the detailed construction of the catalyst for

applying the polymer electrolyte fuel cell (PEFC) based on the catalyst structure was not considered. The ideal catalyst structure can differ between the hydrogen sacrificial protection method and the conventional electrodeposition method. To propose the detailed construction guidelines for structure-based catalyst, it is necessary to consider particle size, degree of alloying, and location of the catalyst in carbon supports, which can contribute to the performance of PEFC [10-14].

In this chapter, a model electrode was prepared, investigated the structure and electrochemical properties of the electrode, and studied the factors that contribute to the performance in the development of PEFC. The model structure can reduce many of the parameters that contribute to the PEFC performance described above, thus revealing the optimized structure of the core-shell catalyst. A Pt/Pd polycrystalline electrode was prepared as a model electrode and its structures and characteristics were investigated.

The electrochemical quartz microbalance (EQCM) method was used to quantitatively investigate the deposition of Pt on Pd substrate by the hydrogen sacrificial protection method. Angle-resolved XPS (AR-XPS) and TEM-EDX revealed the structure of structurally-controlled Pt atomic layers in Pt/Pd polycrystalline electrodes. Furthermore, the electrochemical properties of Pt/Pd polycrystalline electrodes prepared by both hydrogen sacrificial protection and electrochemical deposition methods were confirmed by cyclic voltammetry (CV) and linear sweep voltammetry (LSV). Finally, the Pt deposition behavior of the hydrogen sacrificial protection method and the conventional electrodeposition method was compared and

discussed with each other to provide an ideal Pt atomic layer for ORR.

2.2 Experimental

2.2.1 Chemicals

Guaranteed reagent grade $HClO_4$ was purchased FUJIFILM Wako Pure Chemicals as an electrolyte solution for electrochemical measurement. Water was purified using a Milli-Q system (Yamato, WQ-500). $PdCl_2$ (Kojima Chemicals) and K_2PtCl_4 (Kojima Chemicals) were used as Pd and Pt precursors, respectively, for the colloidal catalysts.

2.2.2 Electrochemical quartz crystal microbalance (EQCM)

All electrochemical measurements in this thesis were carried out in a typical three-electrode system. A platinum (Pt) plate was used as a counter electrode (CE), and a reversible hydrogen electrode (RHE) (RHEK, BAS) was used as a reference electrode (RE). The electrolyte solution was saturated with Ar, O_2, or H_2 by introducing these gases through the solution for at least 20 min, and the gas was continued to flow over the solution during the electrochemical measurements.

The EQCM measurement is used for quantitative analysis for electrocatalyst. In this study, the Pt deposited on Pd electrode was estimated by this method.

Figure 2-1 shows the EQCM setup diagram. The working electrode for the EQCM measurements was a 10 MHz AT-cut quartz crystal plate covered with a Pd or Pt polycrystalline film (100 nm Pd or Pt thin film deposited on Ti substrate manufactured

by Hokuto denko) mounted to an EQCM sensor (HQ-601DK, Hokuto Denko). The oscillation frequency of the quartz crystal electrode was recorded with a sampling time of 1 s by a potentiostat/galvanostat (HZ-7000, Hokuto denko) connected to a frequency counter (HQ-101D, Hokuto Denko). Prior to each measurement, an electrochemical cleaning was carried out in Ar saturated 0.1 M $HClO_4$ solution by a continuous potential cycling in the potential region (0.05~+1.4 V) until clear and sharp hydrogen adsorption/desorption peaks appears.

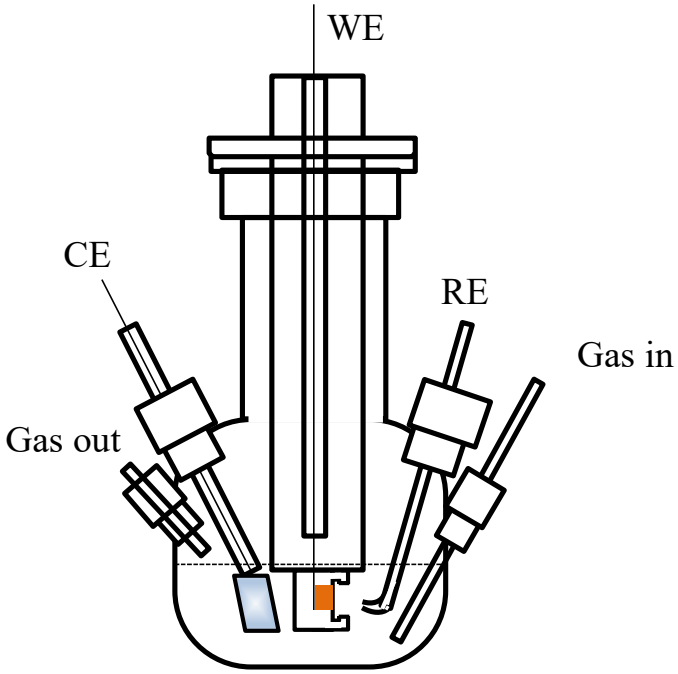

Figure 2-1 Setup diagram of setup for EQCM measurements.

The mass change (Δm) for all the EQCM results was estimated from the resonant frequency shift (Δf) by the Sauerbrey equation (2.1) [15],

$$\Delta m = - k \times \Delta f \qquad (2.1)$$

where k was 0.31 $ng \cdot Hz^{-1}$ in this thesis. This k value was confirmed in comparison to

the previous report [16]. A calibration of QCM was confirmed by using a calibration curve from the Pt electrodeposition method described below in section 2.3.1.

2.2.3 Model catalyst preparation

Figure 2-2 shows a schematic diagram of the model catalyst preparation in this thesis. Two platinum deposition methods were examined and the hydrogen sacrificial protection method was compared with the conventional electrodeposition method.

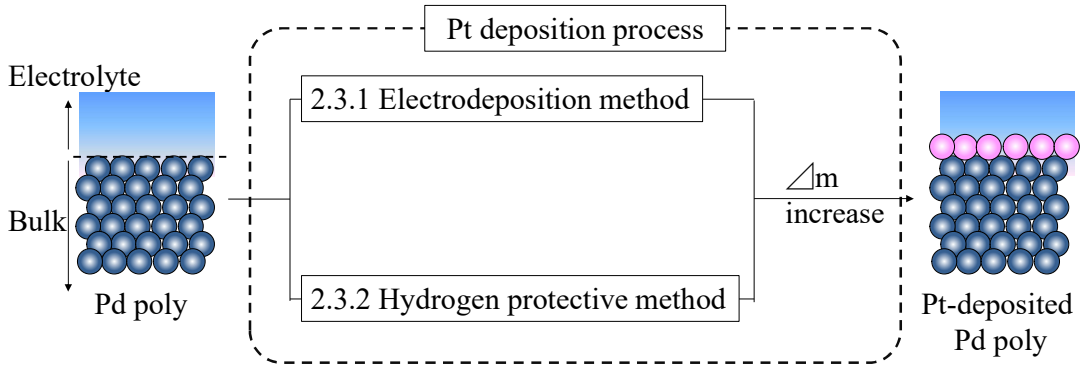

Figure 2-2 Schematic diagram of model catalyst preparation process in this study.

2.2.3.1 Electrodeposition method

Pt was electrodeposited on the Pd polycrystalline electrode at a constant potential. Prior to Pt deposition in this thesis, Pt was deposited at 0.80 V for a predetermined time in 0.6 mM K_2PtClO_4+0.05 M $HClO_4$ aqueous solution until a given frequency change was obtained. This electrodeposition potential and electrolyte concentration were determined according to the results of Pd electrodeposition on Au in a previous report [17-18].

Figure 2-3 shows the time dependence of potential (a), current density (black dots), and frequency change (blue dots) (b) at Pd polycrystalline electrode in a 50 mM $HClO_4$ containing 0.6 mM K_2PtCl_4. The black arrow shows t=0 s when the potential was applied from OCV to 0.80 V at 25 °C. Before applying the potential from OCV to 0.80 V, there was no change in current density and Δf. On the other hand, after t=0 when the potential was applied to 0.80 V (Fig.2-3 (a)), the reduction current flowed (Fig.2-3 (b) black dot), and Δf decreased linearly (Fig.2-3 (b) blue dot). It was assumed that Pt deposition was observed because such decrease in Δf was similar to metal deposition when the potential was applied to deposition potential from OCV. In addition, mass per electron (mpe) for Pt deposition was confirmed [17-18]. **Figure 2-4** shows the relationship between the mass change (Δm) and the charge (Q) obtained from the cathodic current at the Pd polycrystalline electrode in a 50 mM $HClO_4$ solution containing 0.6 mM K_2PtCl_4. Mpe was obtained as 49.2 g/mol. This value was in good agreement with the estimated value because Pt reduction in acidic solution consumed 4 electrons ($Pt^{4+}+4e^- \rightarrow Pt^0$: 49.2×4 =196.8 g/mol, while the mass of Pt was 195.8 g/mol).

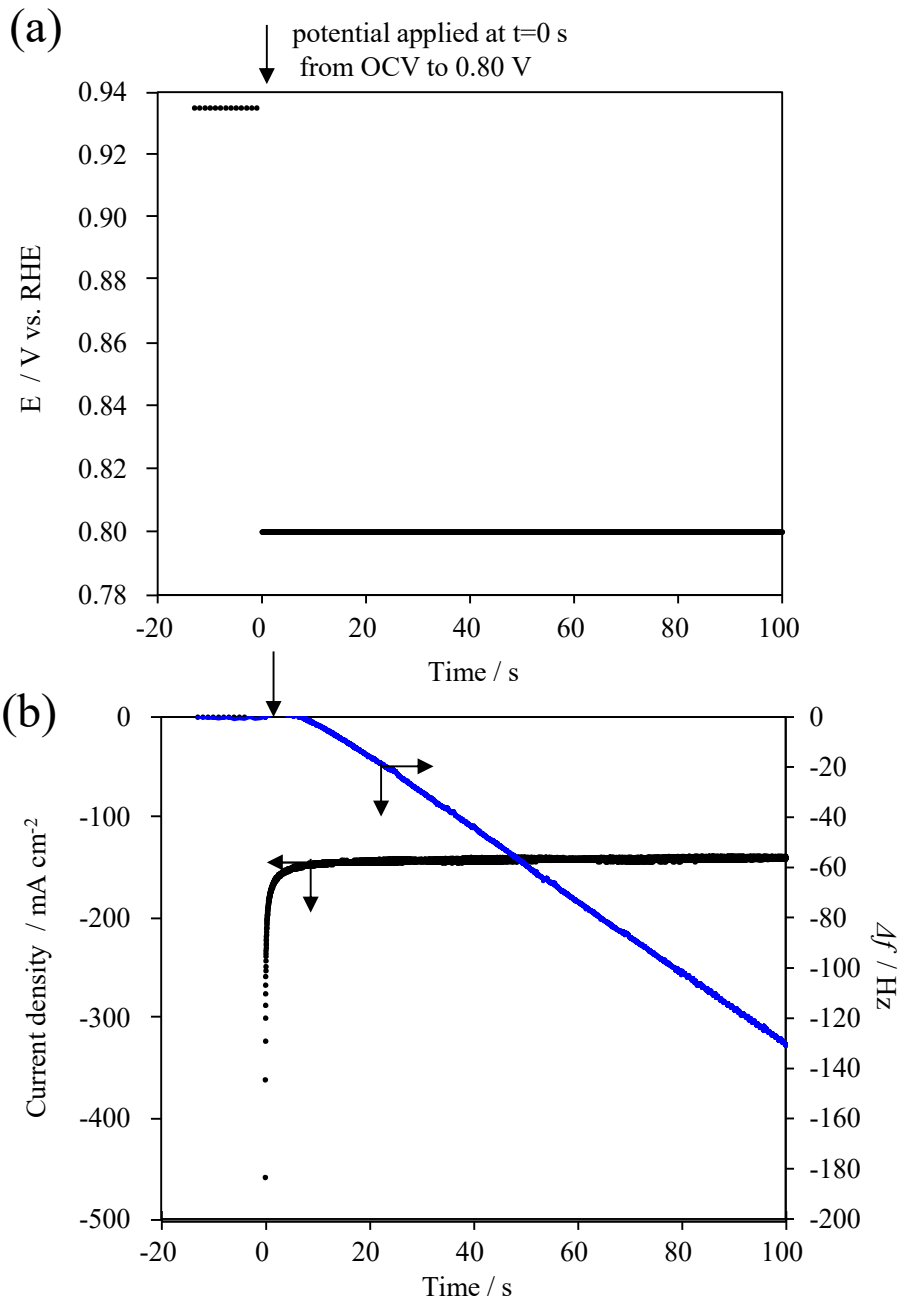

Figure 2-3 Time dependence of potential (a), current density (black dot) and frequency change (blue dot) (b) at a Pd polycrystalline electrode in a 50 mM $HClO_4$ containing 0.6 mM K_2PtCl_4. The black arrow shows t=0 s when the potential was applied from OCV to 0.80 V at 25 °C.

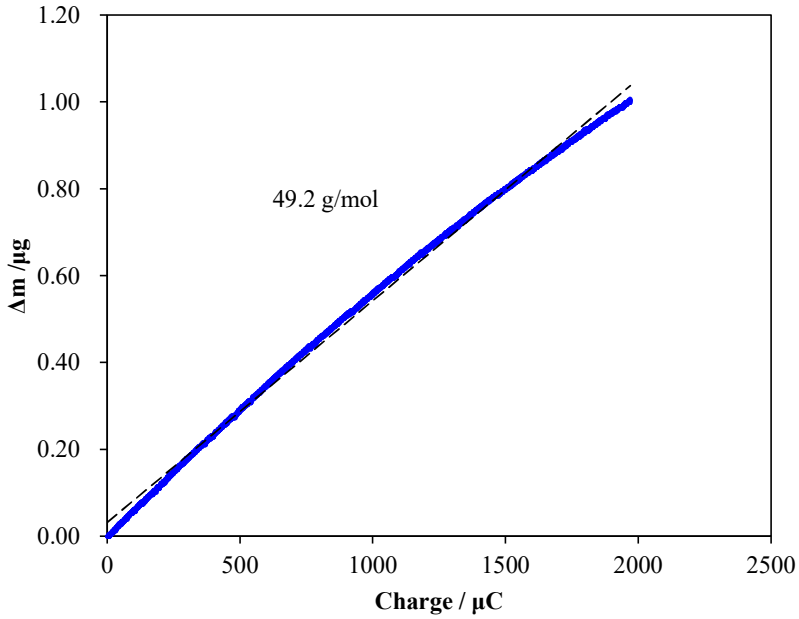

Figure 2-4 Relationship between mass change (Δm) and the charge (Q) obtained from the cathodic current at Pd polycrystalline electrode in a 50 mM $HClO_4$ solution containing 0.6 mM K_2PtCl_4 when the potential was kept at 0.80 V at 25 °C. The solid blue line and the dotted black line represent the experimental data and approximate straight line by least squares method, respectively.

2.2.3.2 Hydrogen sacrificial protection method

Pt was chemically deposited on the Pd polycrystalline electrode by hydrogen adsorption. Prior to hydrogen bubbling, the Pd polycrystalline electrode was immersed in Ar-saturated 0.1 M $HClO_4$. Hydrogen gas was supplied for 30 min. After adsorbing hydrogen on the Pd electrode, Ar gas was introduced to degas the dissolved hydrogen in the electrolytic solution [19-20]. Then, 5 mL of a 0.6 mM K_2PtClO_4+0.05M $HClO_4$ aqueous solution was added dropwise to the electrochemical cell described in Fig.2-1 and the Pd polycrystalline electrode was immersed until a predetermined frequency change was obtained to deposited Pt. In addition, OCV was recorded to confirm the

hydrogen adsorption behavior.

2.2.4 Characterization

2.2.4.1 Angle-resolved X-ray photoelectron spectroscopy (AR-XPS)

The surface coating thickness of a multi-layered structure is estimated by angle-resolved XPS measurement [21]. The Pt/Pd polycrystalline model electrode prepared in Chapter 2.2.3 was fixed to the XPS sample holder by using carbon tape. X-ray photoelectron spectroscopy was carried out under ultra-high vacuum of 10-6 Pa or less, KATROS (manufactured by Shimadzu Corporation), X-ray target is Al, voltage: 15 kV, current: 10 mA, Pass energy: 80-160, sample The binding energies around 72 eV and 334 eV corresponding to the Pt 4f and Pd 3d orbitals were measured with take-off angles: 60 °, 45 °, and 30 °, respectively.

2.2.4.2 Transmission electron microscope (TEM)

The catalyst structure and composition were determined by a transmission electron microscope (TEM: JEM-ARM200F, JEOL) equipped with an energy-dispersive *X-ray* spectroscopy (EDS: JED-2300T, JEOL) system. High-Angle Annular Dark-Field Scanning Transmission Electron Microscopy (HAADF-STEM) was performed at an accelerating voltage of 200 kV.

In this Chapter, the sample for TEM-EDS characterization was prepared by cross-sectioned by Ga ion beam. The Pt/Pd model electrodes were cross-sectioned by FIB-SEM (JIB-4501, JEOL).

2.2.4.3 Electrochemical evaluation of Pt/Pd model polycrystalline electrodes

The electrochemical evaluation of the Pt / Pd model polycrystalline electrode was carried out in a 0.1 M $HClO_4$ aqueous solution with a counter electrode (Pt plate) and a reference electrode (RHE) as described in 2.2.2 and Fig. 2-1.

2.3 Results and Discussion

2.3.1 Pt deposition process by hydrogen sacrificial protection method

2.3.1.1 Formation of Pt atomic layer

Figure 2-5 shows the response of open-circuit voltage (OCV) and frequency change (Δf) monitored simultaneously by EQCM. Supplying H_2 gas to the electrochemical cell reduced the oxide present on the surface of the Pd substrate, causing the OCV to change slightly negative from 0.88 to 0.8V in 700 s. At this point, a slight increase in Δf was observed. This frequency change can result from the introduction of hydrogen gas into the cell, which agitates the surface of the electrode and changes the surface adsorption species of the electrode [15-16].

When OCV reaches 0.8 V, hydrogen can be partially stored in Pd because Pd is a well-known hydrogen storage material [22]. Thus, the increase in Δf may be due to hydrogen storage in Pd and substitution with hydroxides and hydrogen on the surface of the Pd electrode [23]. Then, OCV decreased rapidly from 0.8 to 0.05 V from 1100 to 1800 s. After the electrolyte solution was saturated with H_2 gas, the OCV was constant and stable after 1800 s. From the binary phase diagram of Pd and hydrogen, it is known that Pd and hydrogen form Pd hydrides such as α-phase Pd-H and/or α'-phase Pd-H in

a hydrogen saturated environment (high hydrogen concentration and room temperature conditions) [22]. It is therefore the OCV is considered to be constant after 1800 s. On the other hand, *Δf* gradually decreased from 10 to -280 Hz between 1100 and 2700 s. This decrease in *Δf* is likely due to hydrogen storage into Pd.

After Ar gas to degas excess hydrogen in the electrolyte solution, Δf decreased to 3000 s and increased to 4300 s. The increase in *Δf* is thought to be due to the hydrogen desorption from the Pd surface because hydrogen was completely replaced by Ar gas.

When K_2PtCl_4 was injected into the EQCM cell, an immediate decrease in *Δ*f was observed, indicating that Pt was deposited on the Pd substrate. The electrode was removed from the solution because a frequency change of 130 Hz (or 260 Hz) corresponds to 1 ML (or 2 ML) Pt layer formation.

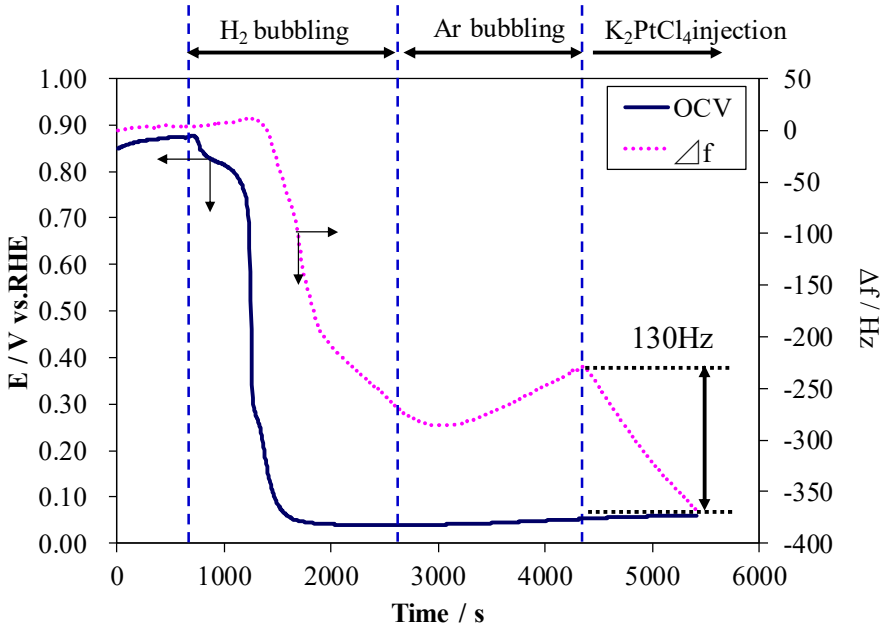

Figure 2-5 The relationship between OCV, ⊿f, and time dependence measured by EQCM. The experimental procedure is shown above.

2.3.1.2 Mass transport of Pt precursor

Figure 2-6 showed the horizontal axis shows the concentration of Pt precursor and the vertical axis showed the Pt deposition rate calculated from EQCM (see Figure 2-5 for 0.6 mM K_2PtCl_4, and the 0.3 and 1.2 mM K_2PtCl_4 were not shown in Figure, which was obtained from experimental studies.), and it was found that they showed good linearity between Pt deposition rate and K_2PtCl_4 concentration. This indicates that the Pt deposition rate was proportional to the concentration (*dC*), and this Pt deposition process was examined from the viewpoint of substance transport. The diffusion equation of Fick's law is shown in equation (2.2), which relates the diffusive flux to the gradient of the concentration.

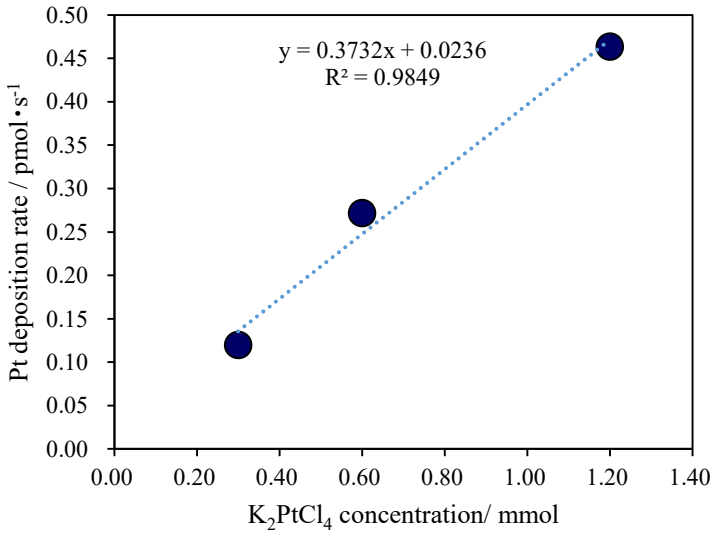

Figure 2-6 The relationship between Pt deposition rate measured by EQCM and K_2PtCl_4 concentration. The dotted line represents the approximation formula by least-squares method.

$$J = -D\frac{dC}{dx} \qquad (2.2)$$

Where, J showed flux of substance (Pt precursor K_2PtCl_4), D was diffusion coefficient, dC was difference of concentration dx showed diffusion layer thickness. Here, in this study, it was estimated that dx is constant because K_2PtCl_4 was supplied to the substrate in the static bath shown in Figure 2-1. On the other hand, from the stoichiometric equation in (2.3), it was considered that the Pt precursor (K_2PtCl_4), was reduced to Pt^0 by hydrogen from Pd to form the Pt atomic layer. **Figure 2-7** shows a schematic model of this interface reaction between Pt and H on Pd.

$$Pt^{4+} + 2H \ + 4e^- \rightarrow Pt^0 + H_2 \qquad (2.3)$$

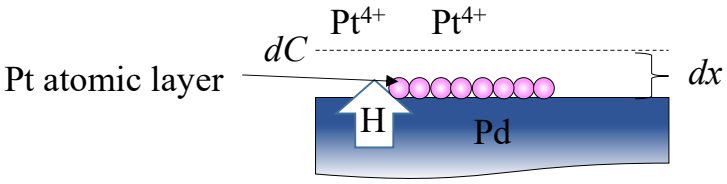

Figure 2-7 Schematic model of interface reaction between Pt precursor and H by hydrogen sacrificial protection method.

Here, when the mass transport of each reactant was estimated, the charge transfer reaction ($4e^-$) was considered to be very fast, and the supply of Pt precursor (Pt^{4+}) or hydrogen (2H) was considered to be the rate-determining step. Considering the amount of substance, the diffusion coefficient is proportional to the amount of substance, so H (hydrogen: 1 g/mol) was estimated about 200 times faster than Pt (195 g/mol).

Therefore, it was suggested that the substance transport control of Pt is effective for the control of Pt atomic layer in the hydrogen sacrificial protection method.

2.3.2 Structure of Pt/Pd polycrystalline model electrode

2.3.2.1 AR-XPS

Figure 2-8 shows the angle-dependent XP spectrum of the Pt/Pd model electrodes prepared by the hydrogen sacrificial protection method with Pt 4f (Fig. 2-8 (a), (c)) and Pd 3d (Fig. 2-8 (b), (d)). The escape angle is defined as the angle between the surface and the analyzer axis and is 30, 40, and 60 °. The coverage of the Pt layer was adjusted from the QCM frequency changes corresponding to 1 ML (Fig. 2-8(a), (b)) and 2 ML (Fig. 2-8(c), (d)).

XPS successfully detected the Pt signal, indicating that the hydrogen sacrifice method formed a thin Pt layer on the Pd surface. The thickness of Pt can be estimated from the peak intensity of the Pt 4f signal. The peak intensity of Pt 4f in the 2 ML catalyst was twice the peak intensity in 1 ML spectrum.

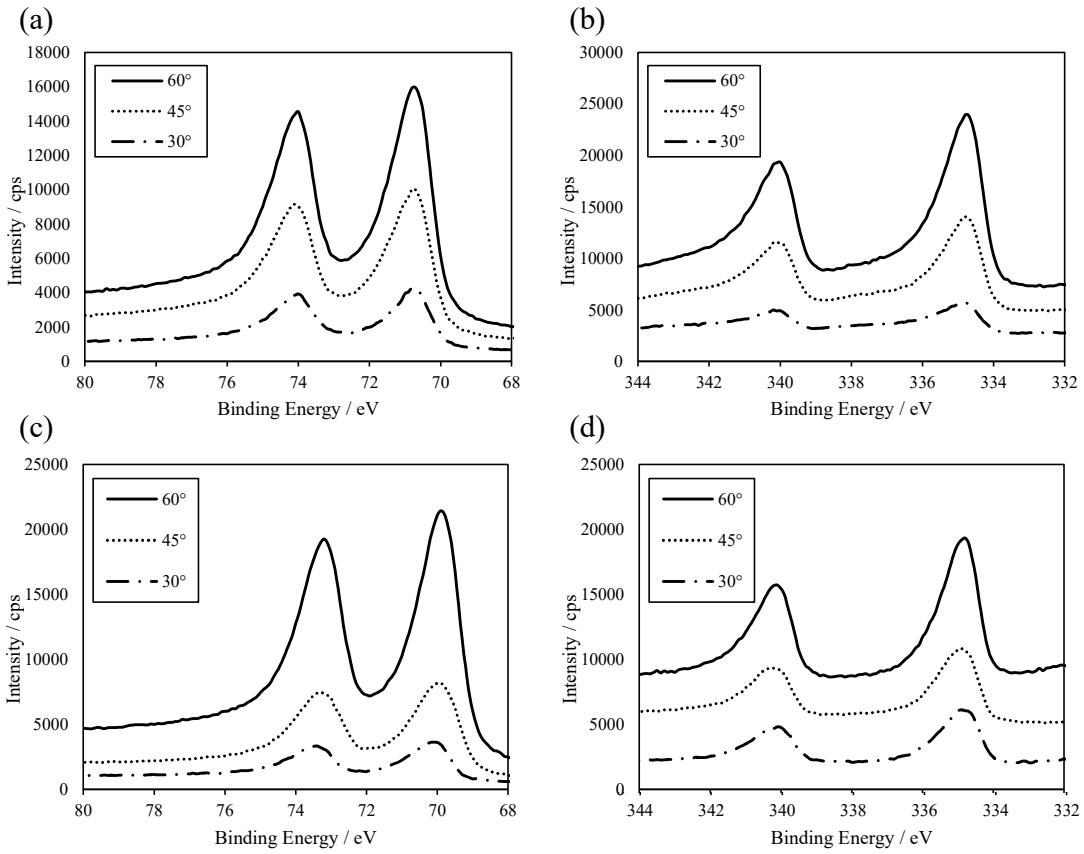

Figure 2-8 AR-XP spectra of (a) Pt4f for 1ML Hydrogen sacrificial, (b) Pd 3d for 1ML Hydrogen sacrificial, (c) Pt4f for 2ML Hydrogen sacrificial, (d) Pd 3d for 2ML Hydrogen sacrificial. The take-off angles θ are 30°, 45°, and 60°, respectively.

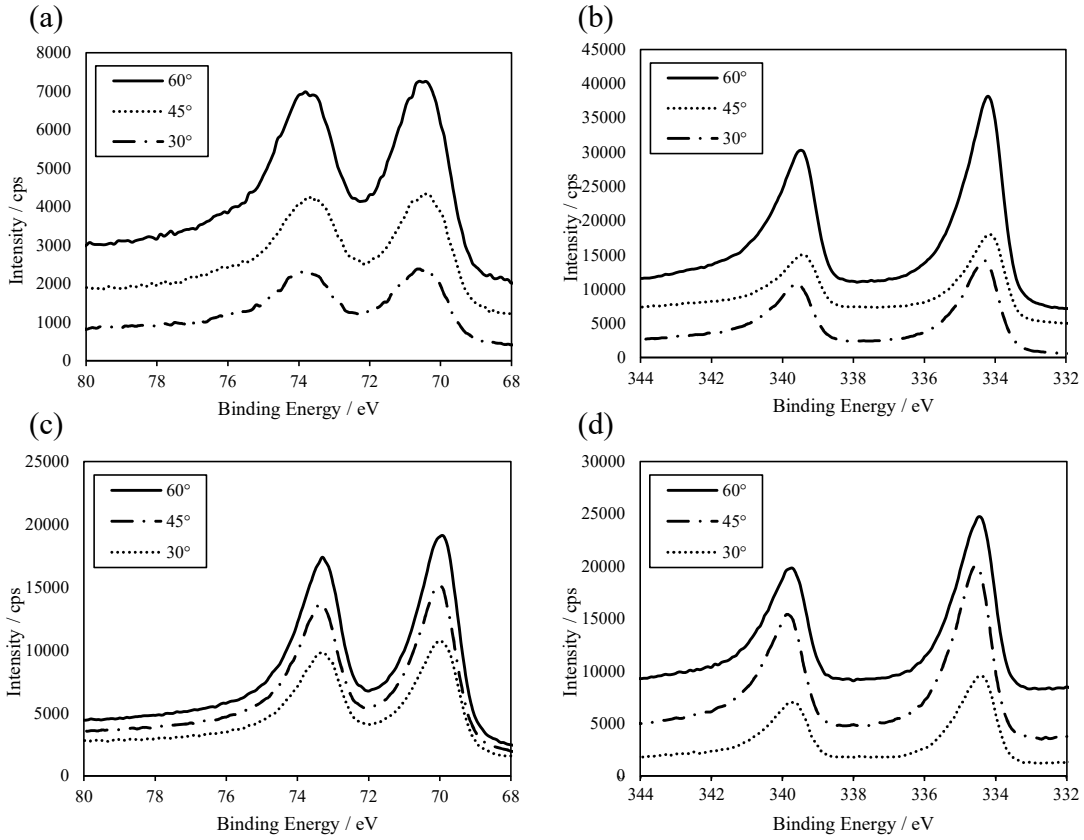

Figure 2-9 AR-XP spectra of (a) Pt4f for 1ML Electrodeposition, (b) Pd 3d for 1ML Electrodeposition, (c) Pt4f for 2ML Electrodeposition, (d) Pd 3d for 2ML Electrodeposition. The take-off angles θ are 30°, 45°, and 60°, respectively.

Figure 2-9 shows the angle-dependent XP spectrum of the Pt/Pd model electrodes prepared by the electrodeposition method with Pt 4f (Fig. 2-7 (a), (c)) and Pd 3d (Fig. 2-7 (b), (d)). The escape angle is defined as the angle between the surface and the analyzer axis and is 30, 40, and 60 °.

The Pt/Pd model electrode prepared by the hydrogen scarification method had a stronger peak intensity of Pt 4f than those prepared by the electrodeposition method. These results indicate that the amount of Pt deposited on the Pd surface is higher than

the amount deposited by the electrodeposition method.

Furthermore, the electronic state of Pt was estimated from XP spectrum. The binding energies of Pt $4f_{7/2}$ and $4f_{5/2}$ were found to be 71 and 73 eV, respectively, suggesting that the metal Pt layer formed on the Pd substrate was completely reduced by hydrogen. Then, the binding energies of the peak top intensity of Pt are summarized in **Table 2-1.** Here the peak top was calculated from θ=30° because the shallower the angle, the more it reflects the chemical state of the outermost surface.

It was found that the binding energy of Pt 4f shifts to the low binding energy side of the experimentally obtained Pt polycrystalline electrode in all the products prepared by the sacrificial hydrogen method. Especially in the case of 2 ML, it was presumed that the electron donation from the base metal specifically increased the electron donation to the Pt atom on the outermost surface.

Table 2-1 The binding energy for Pt 4f from XP spectra at θ=30°

Samples	**Pt $4f_{7/2}$ / eV**	**Pt $4f_{5/2}$ / eV**
1ML-Hydrogen sacrificial	70.8	73.8
2ML-Hydrogen sacrificial	70.6	73.5
1ML-Electrodeposition	71.1	74.5
2ML-Electrodeposition	71.0	73.9
Pt polycrystalline	71.4	74.8

As shown in Chapter 1.6.2, the thickness of Pt can be estimated quantitatively by the calculation using equation (2.4) [21],

$$\ln\left(\frac{[Pd]}{[Pt]}\right) = \frac{-d}{\lambda \sin\theta} \qquad (2.4)$$

where [Pd] and [Pt] represent the integral value of the peak intensities of Pd 3d ($3d_{3/2}$+$3d_{5/2}$) orbital and of Pt 4f ($4f_{5/2}$+$4t_{7/2}$) orbital.

Figure 2-10 shows the linear relationship between ln([Pd]/[Pt]) intensity and 1/sinθ. The mean free path of photoelectrons in the thin film was estimated to be 1.5 nm from Tanuma's equation [23].

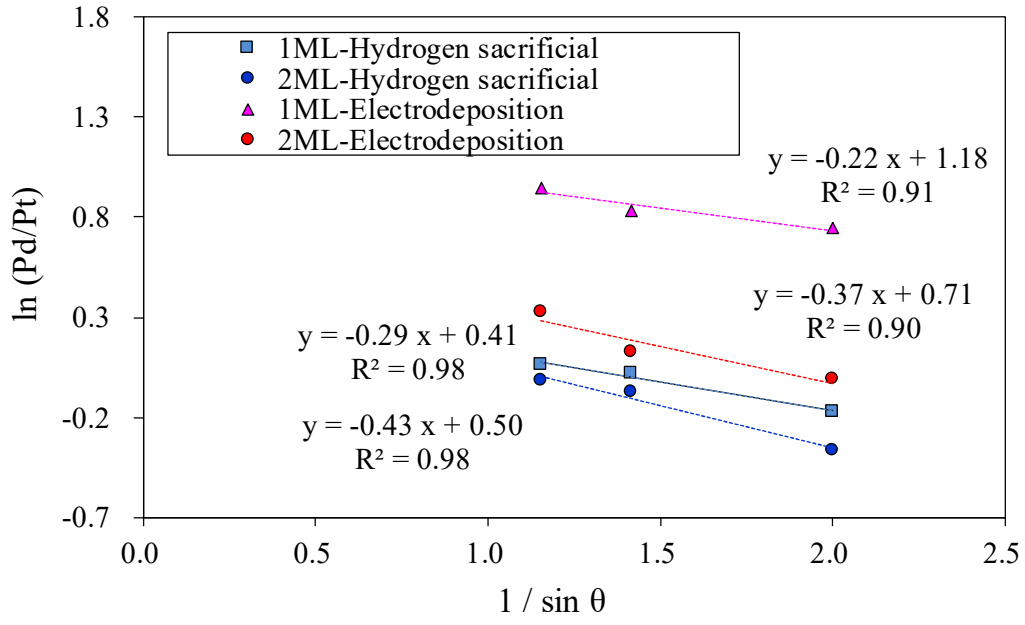

Figure 2-10 Relationship between Pd/Pt intensity and 1/sinθ calculated from AR-XPS.

Table 2-2 summarized the d/λ values calculated from the XPS results and the experimental Pt thickness. The reaction charge caused by the current is 79.8 μQ (1ML-Electrodeposition) and 159.5 μC (2ML-Electrodeposition), which correspond to the theoretical thickness of Pt. As a feature of the hydrogen sacrificial protection method, it was found that the thickness of Pt calculated from the results of AR-XPS exceeds the thickness of Pt of the electrodeposition method. The possibility that the thickness of Pt was overestimated suggests that there was a local distribution of the thickness of Pt because the amount of Pt deposited was quantitatively calculated by EQCM (Δf). This assumption must be determined by local structural analysis, as described in the next section.

Table 2-2 The value of d/λ calculated from AR-XPS, the experimental value of Pt thickness.

Samples	Q/μC	d/λ	Experimental Pt thickness/nm
1ML-Hydrogen sacrificial	—	0.29	0.44
2ML-Hydrogen sacrificial	—	0.43	0.65
1ML-Electrodeposition	79.8	0.22	0.33
2ML-Electrodeposition	159.5	0.37	0.56

2.3.2.2 TEM-EDX

Figure 2-11 shows the HAADF-STEM cross-sectional image and EDS line profile of the Pt/Pd model electrodes prepared by the hydrogen sacrificial protection method. From the EDS line profile, Pt was successfully detected in both 1 ML and 2 ML samples. Pt was also detected at the edge of the sample (the surface of the Pt/Pd polycrystalline electrode). From these results, it was confirmed from the local structure that Pt was deposited on the surface of Pd by the hydrogen sacrificial protection method. From the EDS line profile, the intensity of the Pt signal in the 2 ML sample was about twice the intensity in the 1 ML sample. This Pt thickness dependence was consistent with the AR-XPS results. Thus, it has been shown that the thickness of the Pt layer can be quantitatively controlled by EQCM, and the tendency of the thickness dependence of Pt by the hydrogen sacrificial protection method has been clarified.

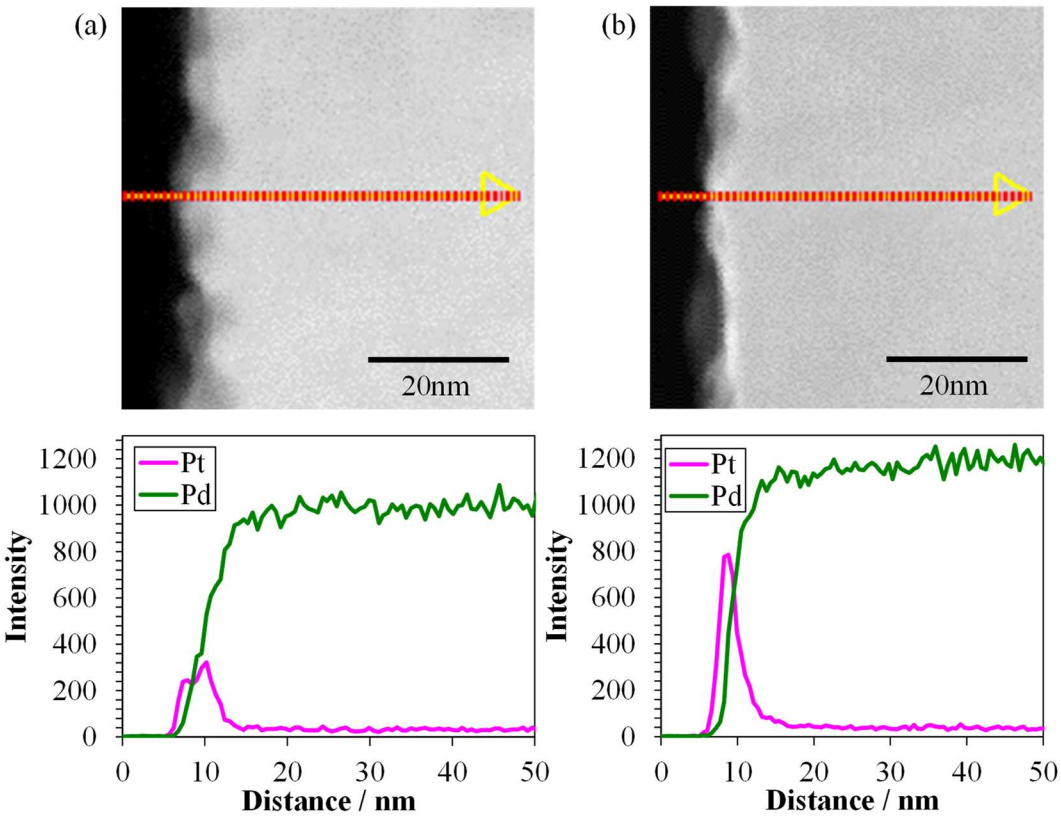

Figure 2-11 Cross sectional HAADF-STEM images and EDS line profiles of Pt/Pd model electrode. (a) 1ML-Hydrogen sacrificial, (b) 2ML-Hydrogen sacrificial. Top: HAADF-STEM image and EDS measurement line (red-yellow arrow), Bottom: EDS line profiles for Pt and Pd signals and distributions.

Figure 2-12 shows the HAADF-STEM cross-sectional images and EDS line profiles of the Pt/Pd model electrodes prepared by the electrodeposition method. It has been confirmed that the basic tendency is the same as the hydrogen sacrificial protection method. However, the EDS line profile intensity of Pt in the 1 ML sample was lower than that of 1 ML sample prepared by the hydrogen sacrificial protection method. This result indicates that the amount of Pt in 1 ML sample prepared by the electrodeposition

method was smaller than that of 1 ML sample prepared by the hydrogen sacrificial protection method. This result also in agreement with the AR-XPS result.

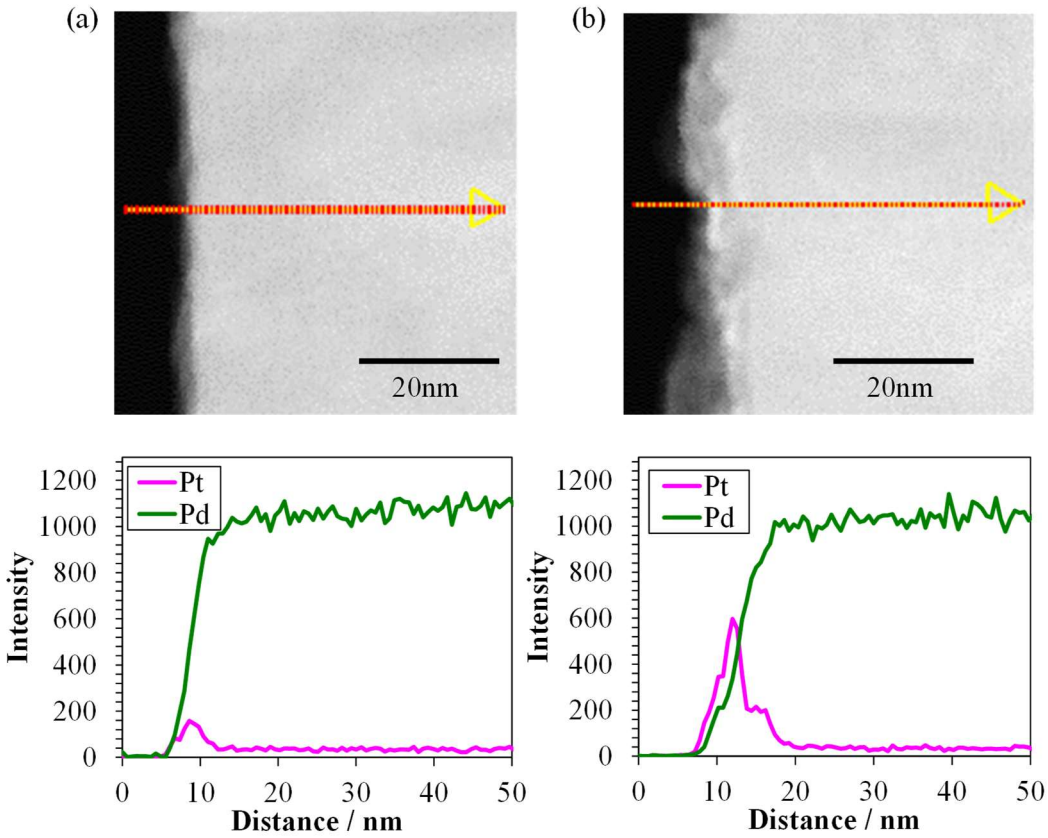

Figure 2-12 Cross-sectional HAADF-STEM images and EDS line profiles of Pt/Pd model electrode. (a) 1ML-Electrodeposition, (b) 2ML- Electrodeposition. Top: HAADF-STEM image and EDS measurement line (red-yellow arrow), Bottom: EDS line profiles for Pt and Pd signals and distributions.

2.3.3 Electrochemical properties of Pt/Pd polycrystalline model electrode

2.3.3.1 Cyclic voltammogram (CV)

Figure 2-13 shows the cyclic voltammogram (CV) of Pt/Pd model electrodes prepared by the hydrogen sacrificial protection method, Pt/Pd model electrodes prepared by the electrodeposition method, and Pd polycrystalline electrodes measured in Ar saturated 0.1 M $HClO_4$ electrolyte solution. All the Pt/Pd model electrodes showed a sharp waveform in the hydrogen adsorption/desorption region of 0.05-0.4 V (anodic and cathodic current) comparing to the substrate (Pd polycrystalline without Pt deposition). The peak potentials of metal oxide reduction at 0.6-0.9 V (anodic current) have shifted to a positive potential compare to the substrate (Pd polycrystalline substrate without Pt deposition). This result was in good agreement with Adzic's previous paper [1]. From this result, it was concluded that Pt deposition on Pd polycrystalline was successfully obtained.

Comparing the hydrogen sacrificial protection method and the electrodeposition method, it was found that the electrode prepared by the hydrogen sacrificial protection method had a larger hydrogen adsorption/desorption peak in CV. The hydrogen adsorption (H_{ads}) charge was summarized in **Table 2-3**. Interestingly, the Pt/Pd model electrodes by the hydrogen sacrificial protection method, which overestimated the thickness of Pt (previous section 2.3.2.1), showed larger H_{ads} in both 1 and 2 ML than the electrodeposition method. This difference of H_{ads} charge between the hydrogen sacrificial protection method and the electrodeposition method may be due to the roughness of the Pt deposition morphology. As mentioned in the previous section, Pt

thickness was overestimated due to the local distribution of the Pt thickness by using AR-XPS and cross-sectional TEM-EDS. This distribution can affect the roughness of the Pt deposited surface.

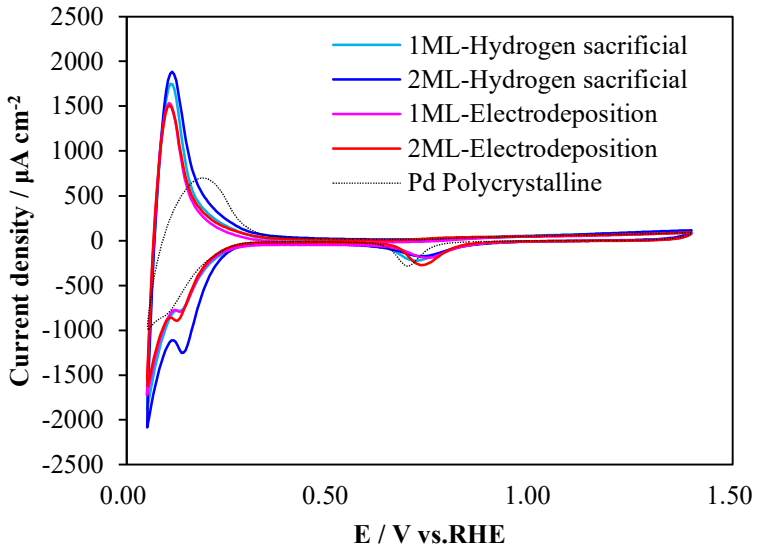

Figure 2-13 Cyclic voltammograms of Pt/Pd model electrodes prepared by the hydrogen sacrificial protection method (1ML-Hydrogen sacrificial, 2ML-Hydrogen sacrificial), the Pt/Pd model electrode prepared by electrodeposition method (1ML-Electrodeposition, 2ML-Electrodeposition), and Pd polycrystalline electrodes electrode measured in 0.1 M $HClO_4$ with Ar saturated. Scan rate was 50 mV/s, Temperature = 23 °C.

Table 2-3 Electrochemical properties of Pt/Pd model electrode prepared by the hydrogen sacrificial protection method, Pt/Pd model electrode prepared by the electrodeposition method, Pd polycrystalline, and Pt polycrystalline electrodes.

Samples	H_{ads} ($\mu C/cm^2$)	The ORR onset potential at -0.02 mA/cm^2 (mV)	Tafel slope ($mV\ dec^{-1}$)	Exchange current density ($mA\ cm^{-2}$)
1ML-Hydrogen sacrificial	2940	840	-123	1.14×10^{-5}
2ML-Hydrogen sacrificial	3950	852	-127	1.87×10^{-5}
1ML-Electrodeposition	2850	825	-128	1.71×10^{-5}
2ML-Electrodeposition	2831	846	-119	7.07×10^{-6}
Pd polycrystalline	2187	775	-93	6.46×10^{-8}
Pt polycrystalline	—	822	-124	1.08×10^{-6}

2.3.3.2 ORR (Linear sweep voltammogram: LSV)

Figure 2-14 shows the linear sweep voltammogram (LSV) of Pt/Pd model electrodes prepared by the hydrogen sacrificial protection method, Pt/Pd model electrodes prepared by the electrodeposition method, Pd polycrystalline, and Pt polycrystalline electrodes measured in O_2 saturated 0.1M $HClO_4$ solution. The onset potentials of the oxygen reduction current are summarized in **Table 2-3**. Here, the onset potential shows when the ORR current is -0.02 mA/cm^2. This is the potential for ORR to proceed when the catalyst exceeds the overpotential under PEFC operating conditions. From these results, the Pt/Pd model electrode prepared by the hydrogen sacrificial protection method shows a positive onset potential (ca. 5 mV) with respect to the Pt/Pd model electrode prepared by the electrodeposition method.

Figure 2-15 shows the Tafel plot of Pt/Pd model electrodes prepared by the hydrogen sacrificial protection method, Pt/Pd model electrode prepared by the electrodeposition method, Pd polycrystalline, and Pt polycrystalline electrodes in O_2 saturated 0.1 M $HClO_4$ solution. Since the slope of Pt/Pd polycrystalline was ca. -120

mV/dec, which was consistent with the previous Pt/Pd and Pt electrodes, suggesting that Pt deposition was successful. The Tafel slope of 120 mV/dec indicates the rate-determining step of the charge transfer of adsorbed oxygen on platinum ($O_{ad} + H^+ + e^- \rightarrow OH_{ad}$). Therefore, the ORR mechanism of the Pt/Pd model electrode prepared by the hydrogen sacrificial protection method in this study was also considered to be the rate-determining step in the previous study described above. [24]. Pd polycrystalline electrode also had the same slope of 90 mV/dec as the previous Pd polycrystalline electrodes [25-26]. As shown in **Table 2-3**, the exchange current density, the Pt/Pd model electrode prepared by the hydrogen sacrificial protection method was 1×10^{-5} mA/cm^2, and the Pt/Pd model electrode produced by the electrodeposition method were $0.7\text{-}2\times10^{-5}$ mA/cm^2. Here, the exchange current density is the current density when the electrochemical reactions in the opposite directions are in equilibrium in the dynamic equilibrium state. The current density of the ORR increases in proportion to the exchange current density. Therefore, PEFC requires a catalyst that increases the exchange current density. As the exchange current increases, the current at the onset potential of the ORR becomes sharper, and larger current densities can be achieved at this potential. Thus, it was considered that the catalytic activity of the Pt/Pd model electrode prepared by the hydrogen sacrificial protection method was higher than that by the electrodeposition method.

The reasons for this improvement in ORR characteristics are discussed in the next section.

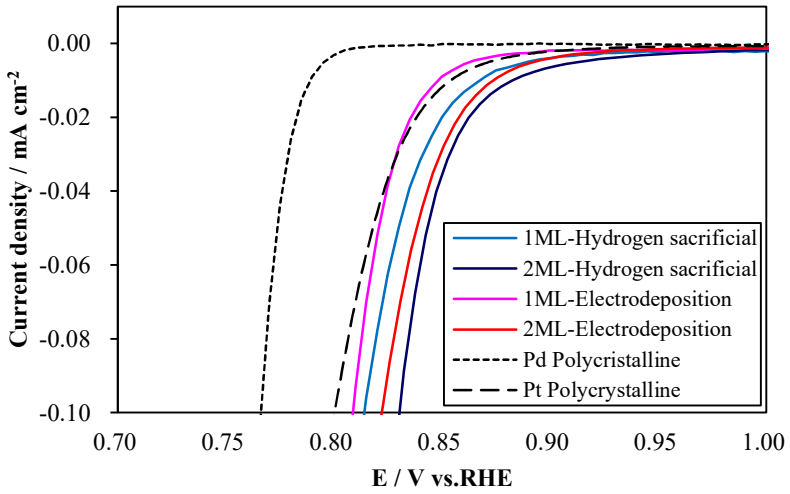

Figure 2-14 Linear sweep voltammograms of Pt/Pd polycrystalline, Pd polycrystalline, and Pt polycrystalline electrodes measured in O_2 saturated 0.1M $HClO_4$ solution. The scan rate was 1 mV/s at temperature = 23 °C.

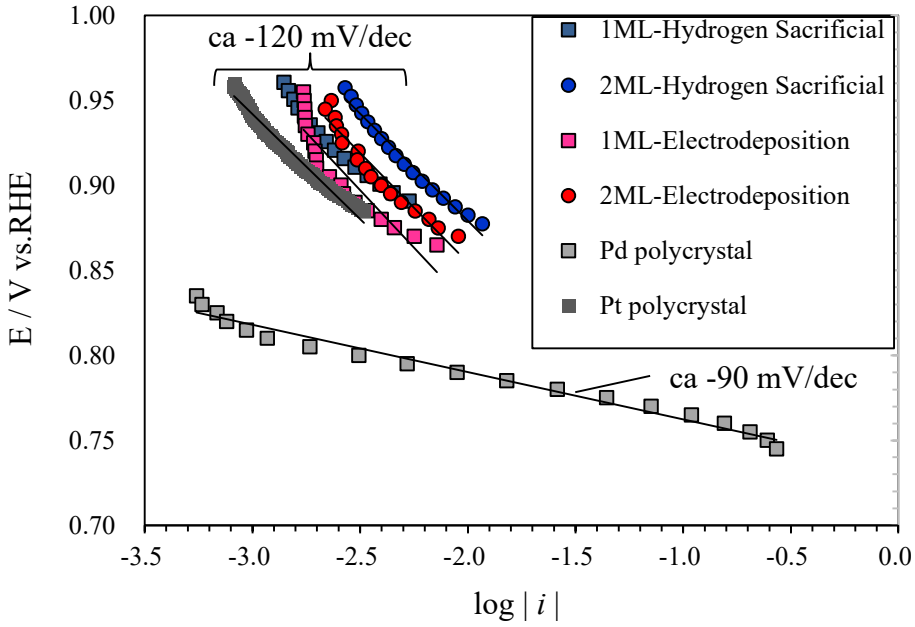

Figure 2-15 Tafel plots of Pt/Pd polycrystalline, Pd polycrystalline, and Pt polycrystalline electrodes measured in O_2 saturated 0.1M $HClO_4$ solution. The scan rate was 1 mV/s at temperature = 23 °C.

2.4 Factor contributing to the ORR performance

Figure 2-16 shows the schematics diagram of the mechanism of Pt deposition on a Pd polycrystalline substrate by hydrogen sacrificial protection method and the electrodeposition method, and the factors that contribute to ORR. As described in the previous section, EQCM, AR-XPS, TEM-EDS, and electrochemical measurements, the surface roughness of the Pt/Pd electrode prepared by the hydrogen sacrificial protection method is larger than that of the conventional electrodeposition method.

Pt deposition on the Pd substrate was derived from the formation of Pd hydride (PdHx) as an intermediate during and after hydrogen gas bubbling. This estimation was approved for the deposition of Pt or Rh on Pd hydride from a previous report [27]. Cappillino et al demonstrated the deposition of Rh on Pd powder derived from Pd hydride. They investigated Rh on Pd (Pd hydride) by a similar sacrificial hydrogen protection method. According to XPS measurement, 8 Å of Rh was deposited with a coverage of 76 % on Pd substrate. Then, 8 Å was equivalent to 3 ML (3 atomic layers) estimated from the atomic radius of Rh. From the above previous report, it was suggested that the deposition of metal by Pd hydride was not completely covered (non-uniform) on substrate. Therefore, it was considered that the thickness of Pt was estimated to be thick and rough due to the formation of hydride. This hydride may promote the deposition of Pt, but the local hydrogen concentration (surface potential) on the hydride surface (hydride/electrolyte interface) may not be uniform, resulting in a high hydrogen concentration. Since Pt can be preferentially deposited from this region,

it is considered that the difference in local hydrogen concentration can be distributed to the local amount of Pt deposition.

On the other hand, the conventional electrodeposition method had no formation of Pd hydride. Thus, Pt deposition was a relatively uniform cover on Pd substrate. It is considered that the morphology of the substrate to be precipitated contributed to the property of Pt deposited on Pd. Thus, the roughness factor and the electronic state of Pt on Pd may have changed in the case of the hydrogen sacrificial protection method.

This mechanism of onset potential shift was suggested as follows:

(i) Increased surface area increases surface steps, terraces, and concave sites on the surface of the Pt/Pd electrode.

(ii) These concave or step/terrace sites can increase the electrochemical reduction potential of Pt oxide.

(iii) These (i) and (ii) represents the binding energy shift by XPS described in 2.3.2.1 (changes in the electronic state of Pt by electron donation from Pd or PdH_x).

There are reports supporting the above hypothesis [28-29]. Efforts have been reported to improve the ORR activity by making the shell layer dendrite-like or by creating a core-shell shape such as creating a concave Pd core structure [28-29]. In this chapter, I have discussed for the first time the contribution to the ORR in the deposition morphology of Pt due to a new Pt atomic layer strategy inspired by the surface chemical state (hydride) as the substrate.

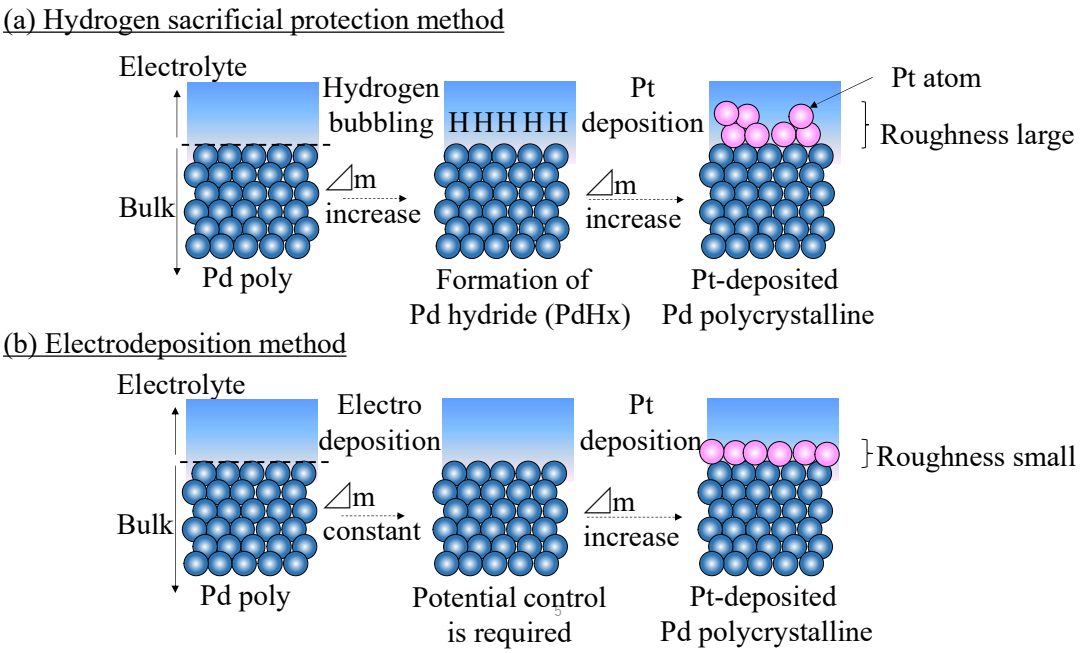

Figure 2-16 Schematic of suggested mechanism of Pt deposition on Pd polycrystalline substrate by (a) Hydrogen sacrificial protection method and (b) Electrodeposition method.

2.5 Conclusion

In this chapter, by studying basic (simple) polycrystalline model electrodes, I quantitatively consider the Pt deposition principle that has not been elucidated by the hydrogen sacrificial protection method from an electrochemical and structural point of view.

Pt/Pd model electrodes were prepared by the hydrogen sacrificial protection method. By using EQCM, it was possible to quantitatively investigate the amount of Pt deposited by the hydrogen sacrifice method, and it was possible to control the amount of Pt on the Pd substrate. It was also confirmed that the model catalyst prepared by the hydrogen sacrificial protection method had better ORR characteristics than the electrodeposition method due to the large surface roughness and its changed electronic state. It was found that when the Pt layer exceeds 2 ML, the ORR properties are as active as or better than 1 ML. Therefore, in real nanoparticle synthesis, it was considered necessary to design the thickness of the Pt coating of two or more atomic layers. Therefore, from the next chapter, I control the surface Pt atomic layer of core-shell nanoparticles by this chapter's principle (the condition for Pt atomic layers on Pd, and its application for catalysts for ORR).

As described above, I proposed guidelines for improving the electrochemical properties of Pt/Pd model electrodes prepared by the hydrogen sacrificial protection method.

2.6 References

(1) J. Zhang, Y. Mo, M. B. Vukmirovic, R. Klie, K. Sasaki, R. R. Adzic, J. Phys. Chem. B 108 (2004) 10955-10964.

(2) K. Sasaki, J. X. Wang, H. Naohara, N. Marinkovic, K. More, H. Inada, R. R. Adzic, Electrochim. Acta (2010) 55 2645-2652.

(3) H. Naohara, Y. Okamoto, N. Toshima, J. Power Sources (2011) 196 7510-7513.

(4) N. Ishiguro, T. Saida, T. Uruga, S. Nagamatsu, O. Sekizawa, K, Nitta, T. Yamamoto, S. Ohkoshi, Y. Iwasawa, T. Yokoyama, M. Tada, ACS Catal. (2012) 2, 1319−1330.

(5) X. Wang, Y. Orikasa, Y. Takesue, H. Inoue, M. Nakamura, T. Minato, N. Hoshi, Y. Uchimoto, J. Am. Chem Soc (2013) 135 5938-5941.

(6) A. Kongkanand, N. P. Subramanian, Y. Yu, Z. Liu, H. Igarashi, D. A. Muller, ACS Catal (2016) 6 1578-1583.

(7) N. Aoki, H. Inoue, A. Shirai, S. Higuchi, Y. Matsui, H. Daimon, T. Doi, M. Inaba Electrochim. Acta (2017) 244 146-153.

(8) N. Aoki, H. Inoue, R. Yoshiura, Y. Hasegawa, S. Miyazaki, A. Suzuki, H. Daimon, T. Doi, M. Inaba, K. Higash, T. Uruga, Y. Iwasawa, H. Tanida, Q. Yuan, N. Takao, H. Imai, T. Mikami, A. Daimaru, J. Electrochem. Soc. (2020) 167 044513.

(9) K. Sasaki, K.A. Kuttiyiel, R.R. Adzic, Curr. Opin. Electrochem. (2020) 21 368–375.

(10) M. Mizuhata, K. Yasuda, K. Oguro, H. Takenaka, DENKI KAGAKU (1996) 692-698.

(11) V. Stamenkovic, B. S. Mun, K. J. J. Mayrhofer, P. N. Ross, N. M. Markovic, J.

Rossmeisl, J. Freeley, J. K. Norskov, Angew. Chem. Int. Ed. (2006) 45 2897-2901.

(12) Y. C. Park, H. Tokiwa, K. Kakinuma, M. Watanabe, M. Uchida, J. Power Sources 315 (2016) 179-191.

(13) M. Watanabe, H. Yano, H. Uchida, D. A. Tryka, J. Electroanal. Chem. 819 (2018) 359-364.

(14) G. Inoue, S. Takenaka, Chem. Lett. (2021) 50 136-143.

(15) C. Gabrielli, M. Keddam, R. Torresi, J. Electrochem. Soc. (1991) 138 2657.

(16) K. Shimazu, H. Kita, J. Electroanal. Chem. (1992) 341 361-367.

(17) H. Naohara, S. Ye, K. Uosaki, J. Phys. Chem. B (1998) 102 4366-4373.

(18) H. Naohara, S. Ye, K. Uosaki, J. Electroanal. Chem. (2001) 500 435–445.

(19) Y. Wang, N. Toshima. J. Phys. Chem. (1997) 101 5301-5306.

(20) H. Naohara, Y. Okamoto, N. Toshima, J. Power Sources 196 (2011) 7510-7513.

(21) H. Fukumitsu, T. Masuda, D. Qu, Y. Waki, H. Noguchi, K. Shimazu, K. Uosaki, Chem. Lett. (2010) 39 768-770.

(22) F. D. Manchester, A. San-Martin, J. M. Pitre, J. Phase Equilibria (1994) 15 62-83.

(23) S. Tanuma, C. J. Powell, D. R. Penn, Surf. Interface Anal. 17(13) (1991) 927-939.

(24) D. B. Sepa, M. V. Vojnovic, A, Damjanovic, Electrochim. Acta (1981) 26 (6) 781-793.

(25) O. Savadogo, K. Lee, K. Oishi, S. Mitsushima, N. Kamiya, K. Ota, Electrochem. commun. (2004) 6 105-109.

(26) Z. Wu, M. Chiang, T. Wang, C. Lee, Int. J. Hydrog. Energy (2018) 43 22195-22204.

(27) P. J. Cappillino, J. D. Sugar, F. E. Gabaly, T. Y. Cai, Z. Liu, J.L. Stickney, D. B. Robinson, Langmuir (2014) 30 (16) 4820-4829.

(28) L Wang, Y. Yamauchi, Chem. Asian J. (2010) 5(12) 2493-2498.

(29) X. Xiong, W. Chen, W. Wang, J. Li, S. Chen, Int. J. Hydrog. Energy (2017) 42 25234-25243.

Chapter 3

CONSTRUCTION OF STRUCTURALLY-CONTROLLED Pt SHELL-Pd CORE CATALYSTS BY HYDROGEN SACRIFICIAL PROTECTION METHOD

3.1 Introduction

Polymer electrolyte fuel cells (PEFCs) have found considerable practical use in fuel cell vehicles (FCVs). To promote the wider uptake of FCVs, it is important to reduce the use of expensive Pt-based catalysts. The cell performance of FCVs is especially dependent on control of the oxygen reduction reaction (ORR) on cathodic Pt catalysts because the ORR is kinetically slower than the anodic hydrogen oxidation reaction. To minimize Pt usage without loss of ORR activity, many approaches to catalyst development have been reported. One promising approach is the deposition of thin Pt overlayers on non-noble or noble metal substrates to make Pt skin, resulting in core-shell structures that change the electronic structure of the catalyst to enhance the ORR activity, and hence reduce the usage of Pt [1-6].

One method for fabricating a core-shell structure is to coat several atomic layers of Pt onto particles of another metal. However, it is essential for the other metal to have almost the same crystal structure as Pt (face-centered cubic lattice, similar atomic radius) for epitaxial growth to occur. Additionally, it is necessary to select a metal species that can be phase-separated from Pt. To meet these requirements, core-shell nanoparticle catalysts with a Pd core and a Pt shell have been investigated. For example,

J. Zang et al. studied the ORR on a Pt shell deposited on Pd nanoparticles, which was formed by the galvanic displacement of an underpotentially deposited Cu monolayer by Pt atoms on the Pd surface [3]. Meanwhile, Wang et al. studied the ORR on a Pt shell deposited on Pd by a colloidal method using hydrogen as a reducing agent [7-8].

However, these previous studies were only concerned with the electrochemical evaluation and did not report the structurally-controlled Pt shell, such as Pt deposition amount on a substrate, Pt shell thickness.

This chapter reports on structurally controlled Pt shell on Pd nanoparticles by the hydrogen sacrificial protection method based on the principle of Chapter 2. This hydrogen sacrificial protection method can be used to easily control bi- or multi-metallic materials using the reduction reaction induced by hydrogen-absorbing on the substrate (core nanoparticles). The hydrogen sacrificial protection method does not involve any contaminating mediators, such as Cu. Furthermore, this procedure is effective for industry because precise potential control is not required [8].

3.2 Experimental

3.2.1 Chemicals

$PdCl_2$ (Kojima Chemicals) and K_2PtCl_4 (Kojima Chemicals) were used as Pd and Pt precursors, respectively, for the colloidal catalysts. Carbon powder (Ketjen black: EC600JD, Lion Specialty Chemicals) was used as a support for the colloidal catalysts. Polyvinylpyrrolidone (PVP: MW = 10,000, Tokyo Kasei Kogyo) was used as a colloid-

protective agent and ethylene glycol (Kanto Chemical) was used as a reducing agent for the Pt and Pd nanoparticles.

3.2.2 Nanoparticles catalyst preparation

Figure 3-1 shows the core-shell nanoparticles catalyst preparation scheme used in this study. Pd-core colloidal solutions were prepared in a flask (equipped with a dropping funnel) containing a mixture of 1.0 M $PdCl_2$ aqueous solutions, ethylene glycol, and PVP. First, the solution was stirred at room temperature for 30 min while introducing Ar gas at a flow rate of 50 mL/min. Then, the temperature was raised to 160 ℃ and kept under 50 mL/min Ar gas for 180 min to obtain a Pd core. After cooling the Pd solution to room temperature, H_2 gas was introduced into the solution for 90 min to adsorb H_2 onto the Pd core. After that, Ar gas was introduced into the solution for 30 min to degas the remaining H_2 in the solution. To prepare a Pt shell structure of the Pd core colloidal solution, a 4 mM K_2PtCl_4 aqueous solution was added to the Pd core solution under Ar gas flow for 10 h. Then, an amount of 4 mM K_2PtCl_4 aqueous solution and its flow rate were controlled by an automatic titrator (Dosimat 765, Metrohm). The condition of titration was summarized in **Table 3-1**.

The Ketjen black powder was added into the Pd core/Pt shell (Pt/Pd) colloidal solution in 90 ℃ for 1 h to prepare Pt/Pd nanoparticles on the carbon support. [8-10] After cooling the mixed solution of Pt/Pd colloid and carbon to room temperature, the solution was suction-filtered three times using a 0.2 μm pore membrane filter and

distilled water. Finally, black powder was obtained, evacuated at 90 ℃ for 300 min, and then used as the Pd core/Pt shell on carbon support (Pt/Pd/C) catalysts. Here, the Pt thickness of Pt/Pd/C was controlled as described in **Table 3-1**.

Pt-only catalyst (Pt/C) and Pd-only catalyst (Pd/C) were also synthesized by the colloidal method as described above.

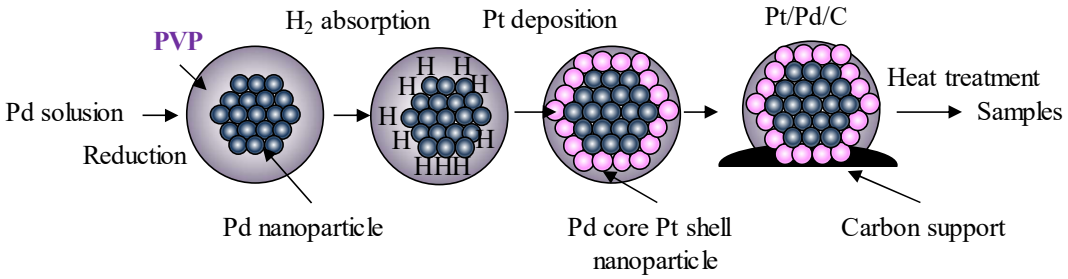

Figure 3-1 Schematic diagram of the preparation of core-shell nanoparticles catalyst by hydrogen protection method and further heat treatment.

Table 3-1 The condition of titration for Pt deposition on Pd nanoparticles

Samples	Pt/Pd atomic ratio	Dosing amount of 4 mM K_2PtCl_4 / mL	Dosing rate of 4 mM K_2PtCl_4 / mL·min^{-1}
1 ML	35/65	56.0	0.11
2 ML	50/50	99.0	0.16
3 ML	75/25	148.5	0.24

3.2.3 Characterization

3.2.3.1 X-ray diffraction (XRD)

X-ray powder diffraction (XRD SmartLab, Rigaku) measurement was performed with Cu Kα radiation (40 kV, 120 mA) in the 2 θ range from 30 to 90 degrees. The crystallite size of nanoparticles was determined by the Scherrer equation (3.1).

The peak was used at Pt (220) about 2 θ = 67 ° because the maximum intensity peak Pt (111) includes the diffraction pattern from carbon supports [11].

$$d = \frac{K\lambda}{\beta cos} \qquad (3.1)$$

Here, d was the crystalline size, K was the Scherrer constant, λ was the X-ray wavelength, and β was the line broadening at half the maximum intensity (FWHM).

3.2.3.2 Transmission electron microscope (TEM)

The catalyst structure and composition were determined by a transmission electron microscope (TEM: JEM-ARM200F, JEOL) equipped with an energy-dispersive *X-ray* spectroscopy (EDS: JED-2300T, JEOL) system. High-Angle Annular Dark-Field Scanning Transmission Electron Microscopy (HAADF-STEM) was performed at an accelerating voltage of 200 kV.

In this Chapter, the sample for TEM-EDS characterization was prepared by placing a drop of as-prepared solution containing the Pt/Pd nanoparticles on carbon supports on a carbon-coated copper grid and drying under vacuum overnight.

3.2.3.3 Electrochemical FT-IR measurement

To characterize the surface properties of the catalyst, an FTIR spectrometer (FT/IR6200, JASCO) equipped with a spectroelectrochemical cell was used, as shown in **Figure 3-2**. An Au thin film was electroless-deposited on the reflecting plane of an attenuated total reflection semicylindrical Si prism (12.5 mm radius and 25 mm length,

Pier Optics) for surface-enhanced infrared absorption (SEIRAS) [12]. The catalysts onto the Au film were used as the working electrode. Ag/AgCl (saturated NaCl) and Pt wire were used as the reference and counter electrode, respectively. Electrochemical FTIR measurements were carried out in a 0.05 M H_2SO_4 (Kanto Chemicals) electrolyte solution.

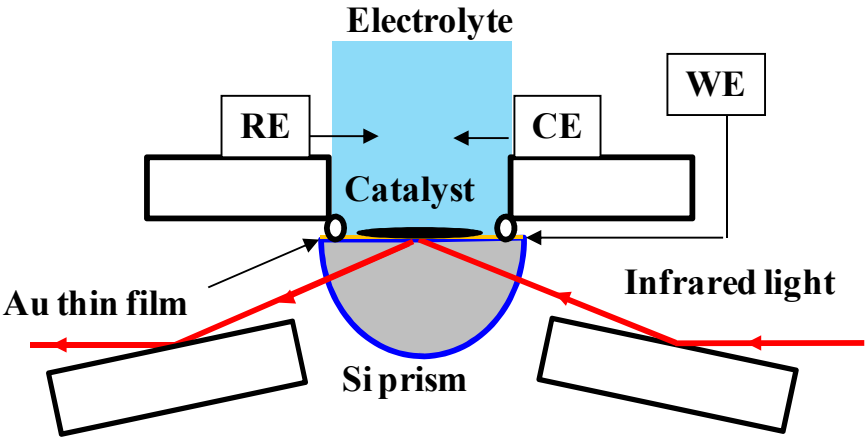

Figure 3-2 Schematic configuration for electrochemical SEIRAS measurement.

The absorbed CO on Pt, Pd can be determined by the surface composition of Pt/Pd [8,12-13]. A methanol (Kanto Chemical) solution was added into 20 mL of the H_2SO_4 electrolyte solution in the spectroelectrochemical cell to adjust the electrolyte concentration to 1.0 M at 0.1 V. The SEIRAS measurements were carried out under a flow of N_2 gas into the electrolyte solution. Background spectra were measured in H_2SO_4 electrolyte solution at each potential to obtain the absorbance spectra in the methanol-added solution in order to observe the surface-adsorbed CO on the catalyst. The reference spectrum at 1.0 V was used to plot the changes in the absorbance spectra.

3.3 Results and Discussion

3.3.1 Structure of Pt/Pd nanoparticles catalyst

3.3.1.1 XRD

The thickness of the Pt atomic layer was estimated from the crystallite size (the particle size of the nanoparticles) by measuring the X-ray powder diffraction. **Figure 3-3** showed the XRD patterns of Pd/C, 1 ML, 2 ML, and 3 ML. The upper black line showed the Pd nanoparticles without Pt atomic layer deposition, the red line showed 1 ML, the blue line showed 2 ML, and the green line showed 3 ML. In X-ray diffraction, the particle size can be calculated from the half-width of each diffraction pattern using Scherrer's equation (3-1). **Figure 3-4** shows the crystalline size and Pt thickness dependence of Pt/Pd nanoparticles. When the crystalline size was plotted on the vertical axis and the Pt atomic layer thickness (1 ML, 2 ML, 3 ML) was plotted on the horizontal axis, experimental data (red, blue, and green) was in good agreement with the white dotted line which was calculated from the geometric nanoparticle size. Therefore, XRD measurements suggested that the Pt atomic layer was quantitatively deposited on the Pd nanoparticles.

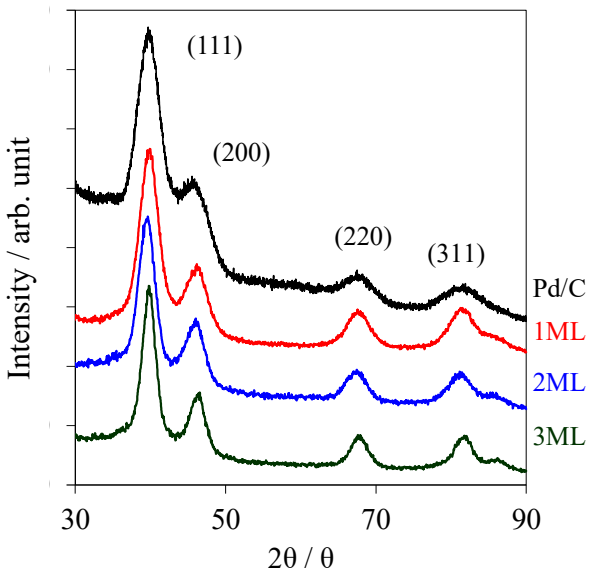

Figure 3-3 XRD patterns for Pd/C, 1 ML, 2 ML, and 3 ML.

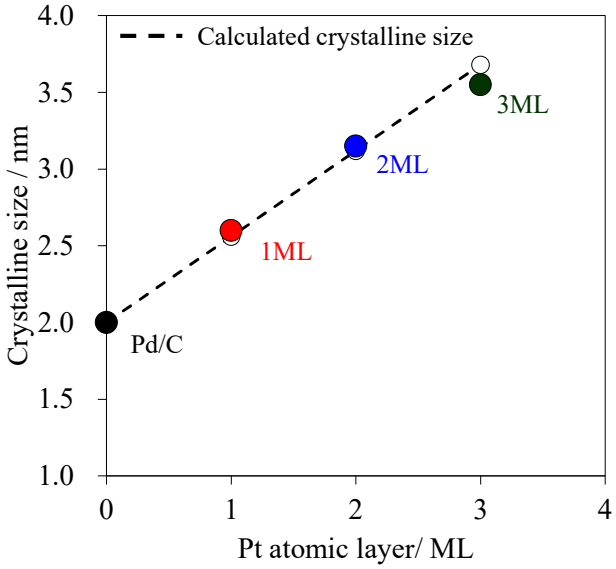

Figure 3-4 Crystalline size (particle size) for Pd/C, 1 ML, 2 ML, and 3 ML, and the white dotted line represents calculated crystalline size which was estimated from geometric nanoparticle size.

3.3.1.2 TEM-EDX

In order to examine the local information about the properties of the Pt atomic layer in more detail, elemental analysis of one nanoparticle using a transmission electron microscope and EDS was carried out. **Figure 3-5** showed the HAADF-STEM images and EDS line profiles for the various samples. In the case of all Pt/Pd/C catalyst (1 ML, 2 ML, 3 ML), the edge of the sample was rich in Pt, while the core was rich in Pd. From this result, we can conclude that the core-shell structure of the Pt/Pd/C catalyst had been successfully constructed.

As ML increased, it became possible to thicken the Pt atomic layer. This result can be said to be supported by the X-ray diffraction described in 3.3.1.1.

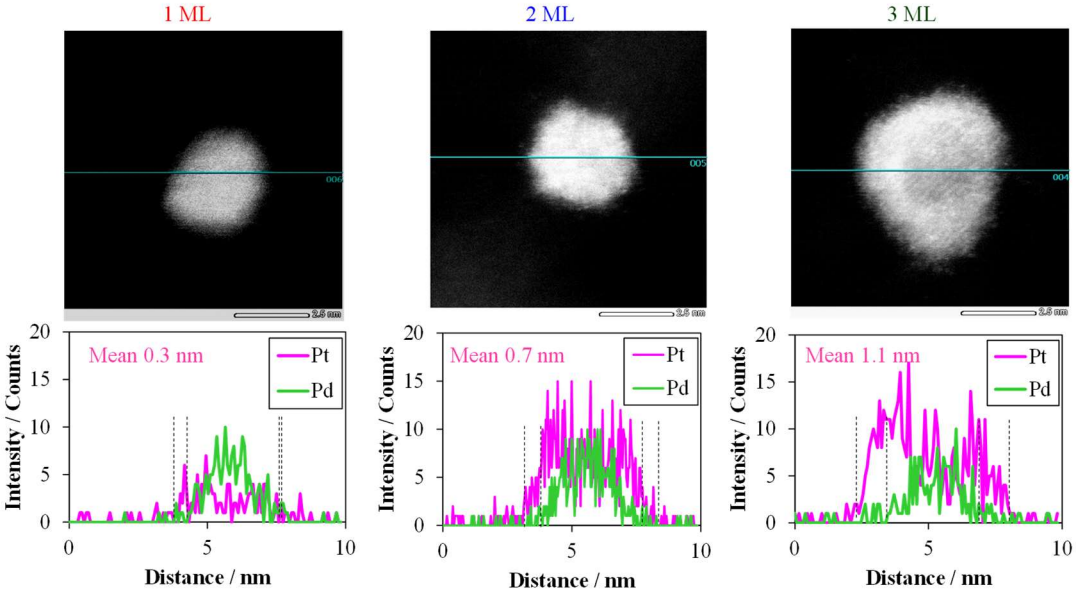

Figure 3-5 HAADF-STEM images and EDS line profiles for 1 ML, 2 ML, 3 ML respectively. The upper showed HAADF images and bottom showed EDS line profiles, the insert dotted line represents the thickness for Pt atomic layer estimated from EDS and mean estimated Pt thickness was shown.

3.3.1.3 Surface enhanced infrared absorption spectroscopy (SEIRAS)

Figure 3-6 showed SEIRAS spectra of Pd/C, Pt/C, 1 ML, 2 ML, and 3 ML. As a comparative sample from above, green shows the spectrum of Pd/C, and black shows the spectrum of Pt/C. The CO bridge site and the top site can be detected, and it can be seen that it reflects the characteristics of the surface elements of Pd and Pt. Next, the spectra of the three Pt atomic layers (1 ML, 2 ML, 3 ML) are shown below. When the Pt thickness was 2ML or more, only CO at the on-top site was detected. This result indicates that the surface of Pt/Pd nanoparticles is completely covered with Pt. On the other hand, 1ML also showed the bridge site of Pd. This indicates that the Pt atomic layer is not completely covered with Pt. Therefore, it was found that 2 ML or more is required to control the Pt thickness of Pd nanoparticles.

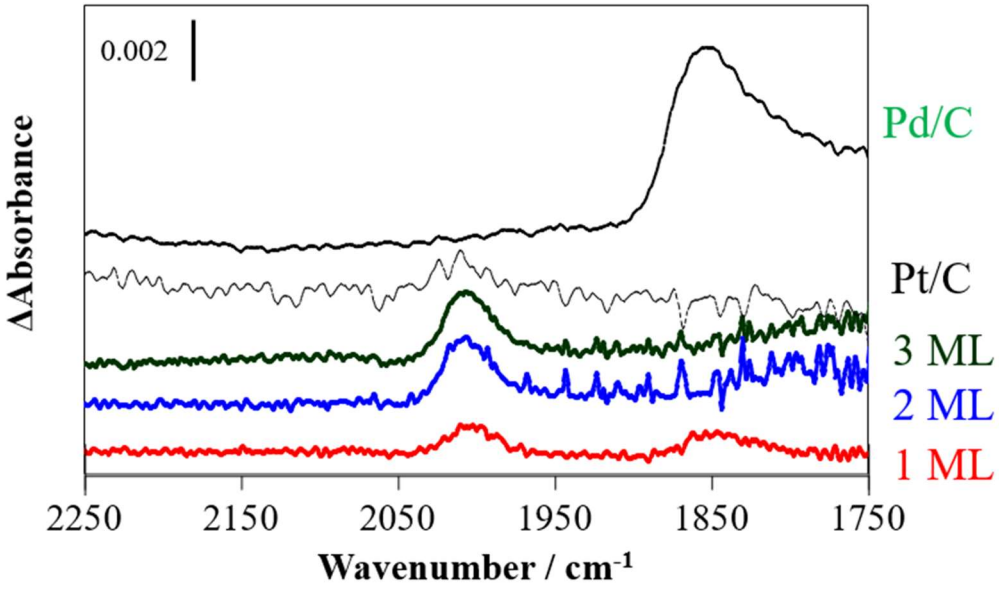

Figure 3-6 SEIRAS spectra of Pd/C, Pt/C,3 ML, 2 ML, and 1 ML.

3.3.2 Structurally-controlled Pt atomic layer on Pd nanoparticles

In the previous section, it was found that Pt precursor concentration control (auto-drop system) is effective for Pt atomic layer control. In addition, as shown in **Figure3-7**, Pt/Pd/C was prepared by the sacrificial hydrogen protection method by controlling the Pt atomic layer to 1-3 layers design (1 ML, 2 ML, and 3 ML). Analysis by SEIRAS showed that the Pt coating was complete under conditions of ≥2 ML.

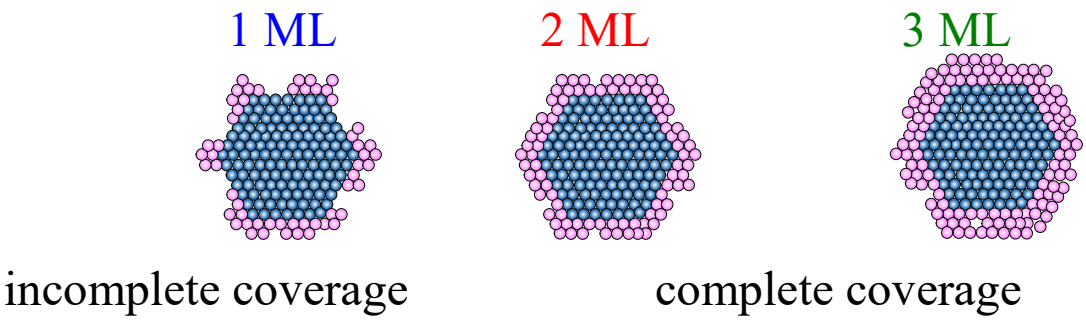

Figure 3-7 Schematic structure of a single Pt/Pd nanoparticle of 1ML, 2ML, and 3ML.

This phenomenon was inferred from the stoichiometric ratios explained in Chapter 2. In the case of the Pd polycrystalline electrode, it was estimated that 50 at% hydrogen was present with respect to Pd. If the chemical composition of hydrogen is also conserved in nanoparticles, 25 at% of the Pt precursor on the Pd surface is reduced to Pt metal by hydrogen according to equation (2.3). On the other hand, the remaining Pt is considered to have been deposited by the Pt disproportionation reaction. Therefore, for 1 ML, the Pt coating is non-uniform (incomplete coating), but for 2 ML and 3 ML, a continuous Pt reduction reaction on the nanoparticle surface completes the Pt coating.

3.4 Conclusion

This section summarizes the results of Chapter 3. By introducing an automatic dropping system that can control the amount of Pt precursor supplied to the synthesis process, we created a Pt atomic layer designed by targeting one to three Pt atomic layers. From various structural analyses, it was found that the Pt coating was completed under the condition of 2 ML or more. As in Chapter 2, the principle behind this is, in the case of nanoparticles, the relationship between the mass transport of the Pt precursor and the supply of hydrogen absorbed by Pd. In the condition where the number of Pt atoms was relatively small, it was assumed that there was an uncoated region of Pt because the Pt particles were locally grown into a few atomic layers due to the excess hydrogen supplied.

3.5 References

(1) T. Toda, H. Igarashi, M. Watanabe, J. Electroanal. Chem. (1999) 460 258-262.

(2) U. A. Paulus, A. Wokaun, G. G. Scherer, T. J. Schmidt, V. Stamenkovic, N. M. Markovic, P. N. Ross, Electrochim. Acta (2002) 47 3787-3798.

(3) J. Zhang, Y. Mo, M. B. Vukmirovic, R. Klie, K. Sasaki, R. R. Adzic, J. Phys. Chem. B (2004) 108 10955-10964.

(4) M. Chiwata, H. Yano, S. Ogawa, M. Watanabe, A. Iiyama, H. Uchida, Electrochemistry (2016) 84 133-137.

(5) L. Wang, W. Gao, Z. Liu, Z. Zeng, Y. Liu, M. Giroux, M. Chi, G. Wang, J. Greeley, X. Pan, C. Wang, ACS Catal. (2018) 8 35-42.

(6) J. Zhang, M. B. Vukmirovic, Y. Xu, M. Mavrikakis, R. R. Adzic, Angew. Chem. Int. Ed. (2005) 44 2132-2135.

(7) Y. Wang, N. Toshima, J. Phys. Chem. B (1997) 101 5301-5306.

(8) H. Naohara, Y. Okamoto, N. Toshima, J. Power Sources (2011) 196 7510-7513.

(9) Z. Liu, C. Yu, I. A. Rusakova, D. Huang, P. Strasser, Top. Catal. (2008) 49 241-250.

(10) S. Li, D. Umereweneza, Separ. Sci. Tech. 47 (2012) 104-111.

(11) K. Jurkiewicz, M. Pawlayta, A. Burian, J. Carbon Res. (2018) 4 68.

(12) Y. G. Yan, Q.X. Li, S.J. Huo, M. Ma, W.B. Cai, M. Osawa J. Phys. Chem. B (2005) 109 7900-7906.

(13) N. Todoroki, H. Osano, T. Maeyama, H. Yoshida, T. Wadayama, Appl. Surf. Sci.

(2009) 256 943-947.

Chapter 4

DEMONSTRATION OF I-V CHARACTERISTICS OF STRUCTURALLY-CONTROLLED Pt SHELL-Pd CORE CATALYSTS IN POLYMER ELECTROLYTE FUEL CELLS

4.1 Introduction

Core-shell catalysts are expected to be highly active catalysts for polymer electrolyte fuel cells (PEFCs) [1-8]. However, to date, there have been fewer reported examples of core-shell catalysts as membrane electrode assemblies (MEAs) compared to Pt alloy catalysts, and the oxygen reduction (ORR) properties have not been as good as those obtained in perchloric acid. For some of the core-shell catalysts in the previous literature, the cyclic voltammograms in the supplementary data show that the oxidation current attributed to hydrogen adsorption of Pd is still present in some cases, and there are scattered results suggesting Pd-exposed regions that are partially covered by the Pt shell layer. Therefore, this chapter verifies the fuel cell properties of the Pt atomic layer of the Pt/Pd core-shell catalyst by the sacrificial hydrogen method constructed in Chapter 2,3 above. In addition, since the hydrogen sacrificial protection method uses polyvinylpyrrolidone (PVP) as a surfactant, the effect of heat treatment on this removal method was verified. These previous studies were only concerned with the electrochemical evaluation and did not report the cell performance of these materials as MEA. When a colloidal agent (surfactant) adheres to nanoparticles, the cell

performance may be impaired because the catalyst surface is effectively polluted by the surfactant. The removal of the surfactant to preserve cell performance has been reported by several groups and showed that the heat-treated catalysts show high ORR activity [9-11]. However, there is no detailed information about the structural changes in Pd core/Pt shell catalysts induced by heat treatment.

In this chapter, I report the cell performance of an MEA based on a Pt/Pd/C catalyst formed by the hydrogen sacrificial protection method and discuss the effect of catalyst surface conditions on the performance. First, I investigated the decomposition conditions of polyvinylpyrrolidone (PVP) and selected the optimum heat treatment conditions using thermal analysis. In addition, a detailed structural analysis of the heat-treated core-shell catalyst was carried out.

4.2 Experimental

4.2.1 Fuel cell performance test for Pt/Pd nanoparticle catalyst

The structure of membrane electrode assembly (MEA) was as follows: anode: Pt/C, cathode: Pt/Pd/C, heat-treated Pt/Pd/C, or Pt/C, and membrane: perfluorosulfonic acid membrane (Nafion NR212). The Pt loading of the catalysts used at the cathode was 0.10 mg/cm^2 for Pt/Pd/C, heat-treated Pt/Pd/C, and Pt/C. We also prepared different Pt loadings of 0.18 mg/cm^2 in Pt/C for the cathode catalyst to show the effect of the Pd core-shell catalyst. The Pt loading in the anode catalyst was 0.10 mg/cm^2.

MEA was prepared by the spraying method [12]. The catalyst ink was sprayed

from the nozzle onto the PTFE film and dried to obtain a catalyst layer. The resulting Nafion film was sandwiched between the catalyst layer and hot-pressed at 135 ℃ for 5 min to obtain MEA. The geometrical active area of the prepared MEA was 13 cm^2 (36x36 mm) and the MEA was assembled into a single fuel cell using a gas diffusion layer (SGL35BC, SGL). Fuel cell performance has been tested under high-humidification operating conditions using a fuel cell test system (PEMTest890, Scribner Associates) [12]. The cell voltage was obtained by scanning the current to evaluate the overvoltage of the catalyst particles. A durability test was carried out by cycling the cell voltage between 0.6 V (hold 4 s) and 1.3 V (hold 4 s) for 200 times. The cell voltage retention at a cell current of 200 mA/cm^2 was plotted.

4.2.2 Heat treatment for Pt/Pd nanoparticle catalyst

The experimental methods (preparation and characterization) of the catalysts after heat treatment were performed under the same conditions as in Chapter 3, unless otherwise noted below.

4.2.2.1 Heat treated PVP thin film

In order to investigate the decomposition temperature of PVP spectroscopically, molecular vibrations were studied by FT-IR. 1 mg of PVP (Mw 10000) was measured and dissolved in 500 mg of ethanol. 0.5 mg/cm^2 of PVP/ethanol mixture was applied on the CaF_2 crystal. The heat treatment was carried out by holding the specimens at 100,

200, and 300 °C in an electric furnace under an air atmosphere for predetermined times (20, 40, 180, and 300 min.).

FT-IR measurements were carried out by transmission method using a collector-type Triglycine sulfate (TGS) detector. The FT-IR measurement was performed by transmission method using a collector-type triglycine sulfate (TGS) detector with the detection wavelength of 1000 - 4000 cm^{-1}. The background was measured by calculating the difference spectrum between the CaF_2 crystal before coating with PVP and the PVP thin film after heat treatment, and converting it to absorbance.

4.2.2.2 Heat treated Pt/Pd/C

Pt/Pd/C was prepared by the method described in Chapter 3.2.2. Here, the condition was set to 2 ML, where the Pt atomic layer on Pd nanoparticles becomes fully covered. To investigate their catalytic properties, the Pt/Pd/C catalysts were further heat-treated at 200 or 300 ℃ under air, or H_2 atmosphere. The heat-treated Pt/Pd/C catalysts are called (atmosphere)-(temperature)-(time)-Pt/Pd/C, and these treatments under different conditions is summarized in **Table4-1** in **Chapter 4**. Pt-only catalyst (Pt/C) and Pd-only catalyst (Pd/C) were also synthesized by the colloidal method as described above.

In order to study the effect of heat treatment on Pt/Pd nanoparticles, I have also conducted heated in-situ observations using a transmission electron microscope (TEM). In order to follow the structure of the nanoregions in the same region of the

catalyst, elemental analysis was carried out in a heatable sample holder under the following conditions to investigate the structure of the Pt atomic layers. In this Chapter, the sample for in situ TEM-EDS characterization was prepared by placing a drop of as-prepared solution containing the Pt/Pd nanoparticles on carbon supports on a sample holder for in situ heat observation (Protochips, Inc.) and drying under vacuum overnight. The observation was carried out under the condition of heating from room temperature to 300°C by increasing the temperature by 50°C every 20 min.

4.3 Results and Discussion

4.3.1 Decomposition of PVP on catalyst

Figure 4-1 shows a TG-DTA analysis of (a) Pd core/Pt shell on a carbon catalyst (Pt/Pd/C) with PVP (noted as "Pt/Pd/C with PVP"), (b) Pt/PVP/C without PVP (noted as "Pt/Pd/C without PVP"), and (c) PVP powder. In the case of Pt/Pd/C with PVP (Fig.4-1(a)), weight loss and peaks in the DTA curve were observed at 165 °C, 270 °C, and 400 °C, respectively. On the other hand, in the case of Pt/Pd/C without PVP (Fig.4-1(b)), there was no change in weight and DTA curve from room temperature to 400 °C. The weight loss and the peak in the DTA curve were observed at ca 450 °C. PVP powder (Fig.4-1(c)) showed the broad weight loss curve and DTA curve with a peak at ca. 400 °C This result showed that the decomposition of PVP powder was remarkable at about 400 °C.

From the above results, these weight loss and peaks in DTA curves were assigned

as follows:

Since Pt/Pd/C without PVP did not contain PVP, the peak in the DTA curve observed at 400 to 450 °C This weight loss and DTA peak are result from the combustion of carbon supports to carbon dioxide. The peak at 165 °C is the decomposition of the PVP thin film on nanoparticles, and the peak at 270 °C is the decomposition of the PVP thin film on carbon. This is because it is a PVP thin-film covered with nanoparticles and carbon supports.

The above results suggest that the decomposition of the PVP thin film was accelerated by Pt/Pd/C. This trend was consistent with a previous report investigating heat-treated Pt/C with PVP [12]. Using in-situ Raman and FT-IR analysis, Boroko et al. showed that Pt nanoparticles initiate PVP decomposition at temperature 100 °C below than PVP powders [13].

As mentioned above, I proposed heat treatment conditions of Pt/Pd/C above 200 °C to decompose PVP thin film on Pt/Pd/C. The next section describes the structure of heat-treated Pt/Pd/C and the characteristics of the fuel cell.

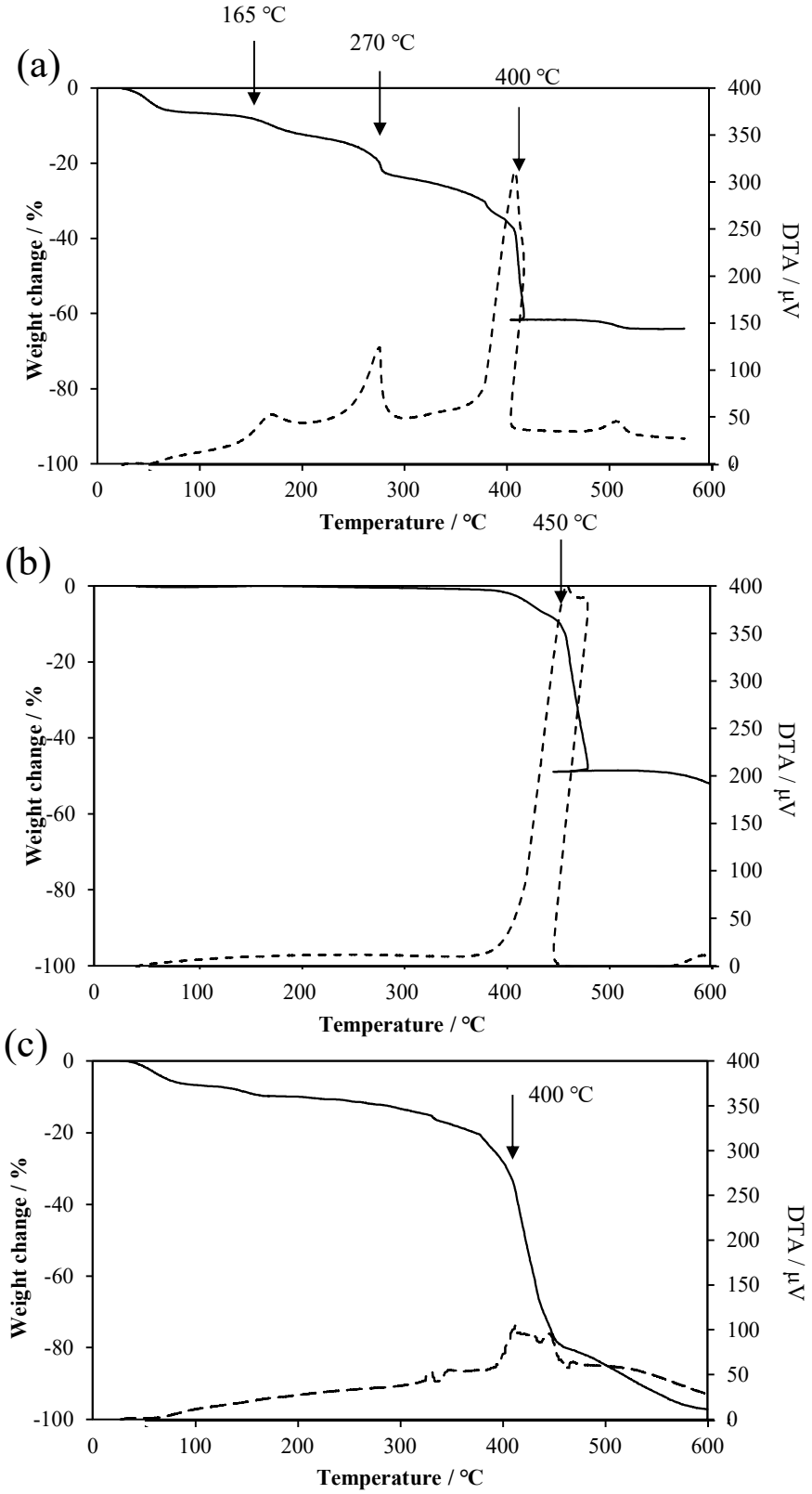

Figure 4-1 TG-DTA analysis of Pt/Pd/C with PVP (a), Pt/PVP/C without PVP (d), and PVP powder (c). The solid line shows weight change and the dotted line shows DTA. The black arrow represents temperature of main weight loss and peak for DTA

4.3.2 Decomposition of PVP thin film

The temperature and time dependence of the removal of the surface-adsorbed PVP thin film was investigated by FT-IR. **Figure 4-2** shows the FT-IR spectrum of PVP thin film for each temperature and time. No change was observed in 100 °C, although above 200°C, the bands of CO stretching vibration around 1700 cm^{-1} and CH stretching vibration around 3000 cm^{-1} decreased. These behaviors are considered to support the decomposition of PVP at temperatures above 165°C, which was observed in TG-DTA in the previous section. At 200°C, the band of CH stretching vibration decreases over time, and becomes more pronounced at 300°C, indicating that decomposition begins after 20 min.

The peak shifts to higher wavenumbers over time, which becomes even more pronounced at 300°C, where the shift occurs to higher wavenumbers. It is considered that this is because the binding energy of the decomposition product is reduced by the heat treatment and it has multiple bonds other than the CO double bonds.

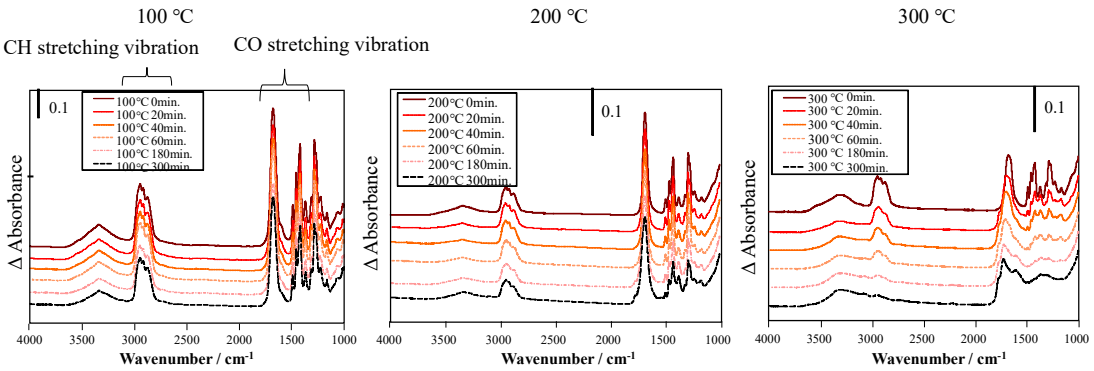

Figure 4-2 FT-IR spectra of PVP thin film for various temperatures and times. Heat treatment temperature: 100°C (left), 200°C (center), 300°C (right). Treatment time: no treatment to 300 min.

4.3.3 Structure of Pt/Pd nanoparticle catalyst

4.3.3.1 XRD

Figure 4-3 shows the Pt/Pd/C XRD patterns and crystal size before and after heat treatment. The effect of annealing at 200-300 °C on the Pt atomic layer and Pt/Pd nanoparticles, where PVP degradation was observed in the previous section, was investigated. In order to quantify this, the crystallite size was calculated from 220 to around 67° using the Scherrer equation. As a result, it was suggested that the crystal grain growth after heat treatment from 200 °C to 300 °C was about 1 nm, and that about 10 % of the nanoparticles were agglomerated on a volume average. As shown above, heat treatment not only removes PVP, but also promotes the particle growth of core-shell nanoparticles.

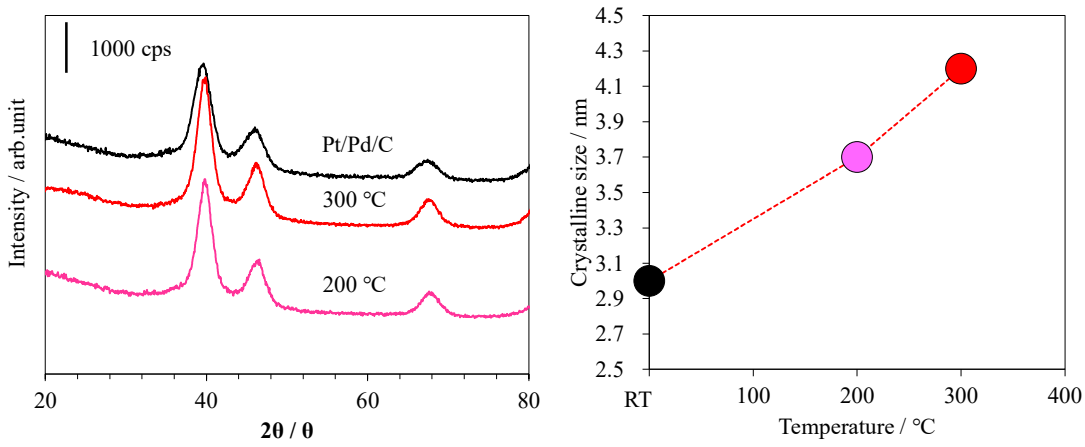

Figure 4-3 XRD patterns of Pt/Pd/C (left) and crystallite size calculated from Sherrer equation (right). Heat treatment temperature: no treatment, 200°C, 300°C, treatment time: 20 min.

4.3.3.2 in situ TEM

Figure 4-4 shows the dependence of Pt/Pd/C nanoparticles on annealing temperature observed by in situ TEM-EDS. In order to analyze in detail the effect of the increase in crystallite size on the Pt/Pd element distribution, in-situ TEM observations were carried out under heating conditions to measure the temperature dependence of the distribution. As shown in the XRD data, particle aggregation and bonding occur at 100-200°C. What is important in here is that in this temperature range, the Pt signal is sharp at the edge of the particles and the core-shell structure is maintained, that is, the Pt atomic layer is retained. However, when the grain growth exceeds 200°C to 300°C, it can be seen that the Pt atomic layer is diffused to the inner Pd side.

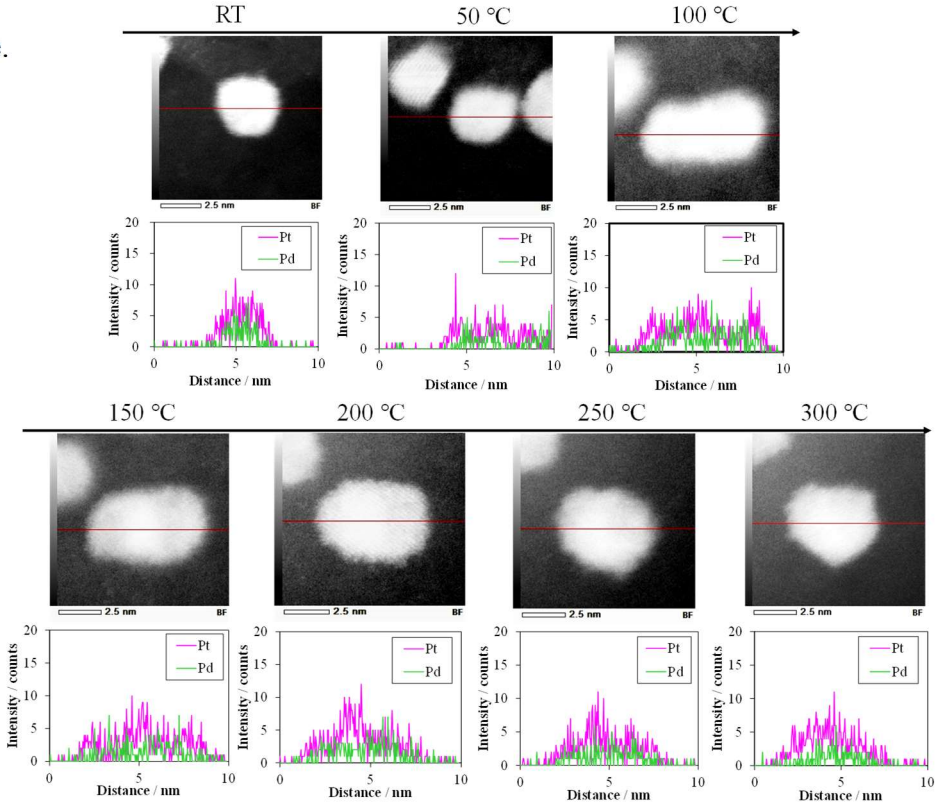

Figure 4-4 Dependence of Pt/Pd/C nanoparticles on annealing temperature observed by in situ TEM-EDX.

4.3.4 Effect of heat treatment on PVP and Pt/Pd core-shell nanoparticles

Figure 4-5 shows a schematic diagram of the proposed mechanism of structural change of Pt/Pd/C prepared by the sacrificial hydrogen method by heat treatment. Before heat treatment (25 °C), the surface adsorbed species PVP is adsorbed on the nanoparticles and carbon. At 165 °C, the PVP film adsorbed on the nanoparticles begins to decompose due to CH stretching vibration with low binding energy. Then, at 270 °C, the PVP film on the carbon also decomposes. The nanoparticles are considered to have a structure in which Pd is partially exposed to the Pt atomic layer due to agglomeration.

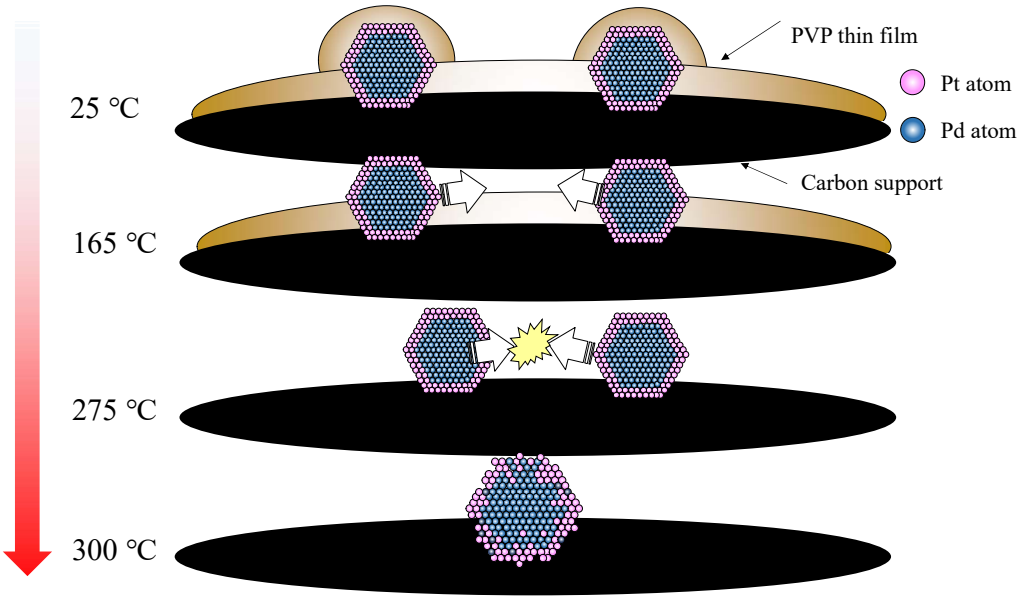

Figure 4-5 Proposed schematic diagram of the mechanism of structural change by heat treatment of Pt/Pd/C prepared by sacrificial hydrogen protection method.

4.3.4.1 TEM-EDX

Figure 4-6 shows the HAADF-STEM images and EDS line profiles for the various samples. In the case of the Pt/Pd/C catalyst, the edge of the sample was rich in Pt, while the core was rich in Pd. From this result, we can conclude that the core-shell structure of the Pt/Pd/C catalyst had been successfully constructed.

With a longer heat treatment time under air (Air-300-30-Pt/Pd/C), the Pt shell was less sharply separated from the Pd core than with shorter heat treatment (Air-300-20-Pt/Pd/C). Heat treatment under an H2 atmosphere (H2-300-20-Pt/Pd/C) also promoted the mixing of the Pt shell and the Pd core relative to the sample heat-treated under air (Air-300-20-Pt/Pd/C). This result implies that the aggregation of nanoparticles on the carbon supports was accelerated by heat treatment under hydrogen.

Furthermore, under H_2, the higher temperature heat treatment (H2-300-20-Pt/Pd/C) promoted complete mixing of the Pt shell with the Pd core and yielded a larger particle size than the lower temperature heat treatment (H2-200-20-Pt/Pd/C). Atomic diffusion between Pt and Pd is evidently easier at a high temperature. It is well known that in the Pt–Pd binary system, phase separation will occur at an elemental composition ratio of Pt: 50 at%, Pd: 50 at% [14]. However, the melting point is lower for nanoparticles than in the bulk [15]. Thus, it can be assumed that Pt and Pd mixed easily, even below 300 °C.

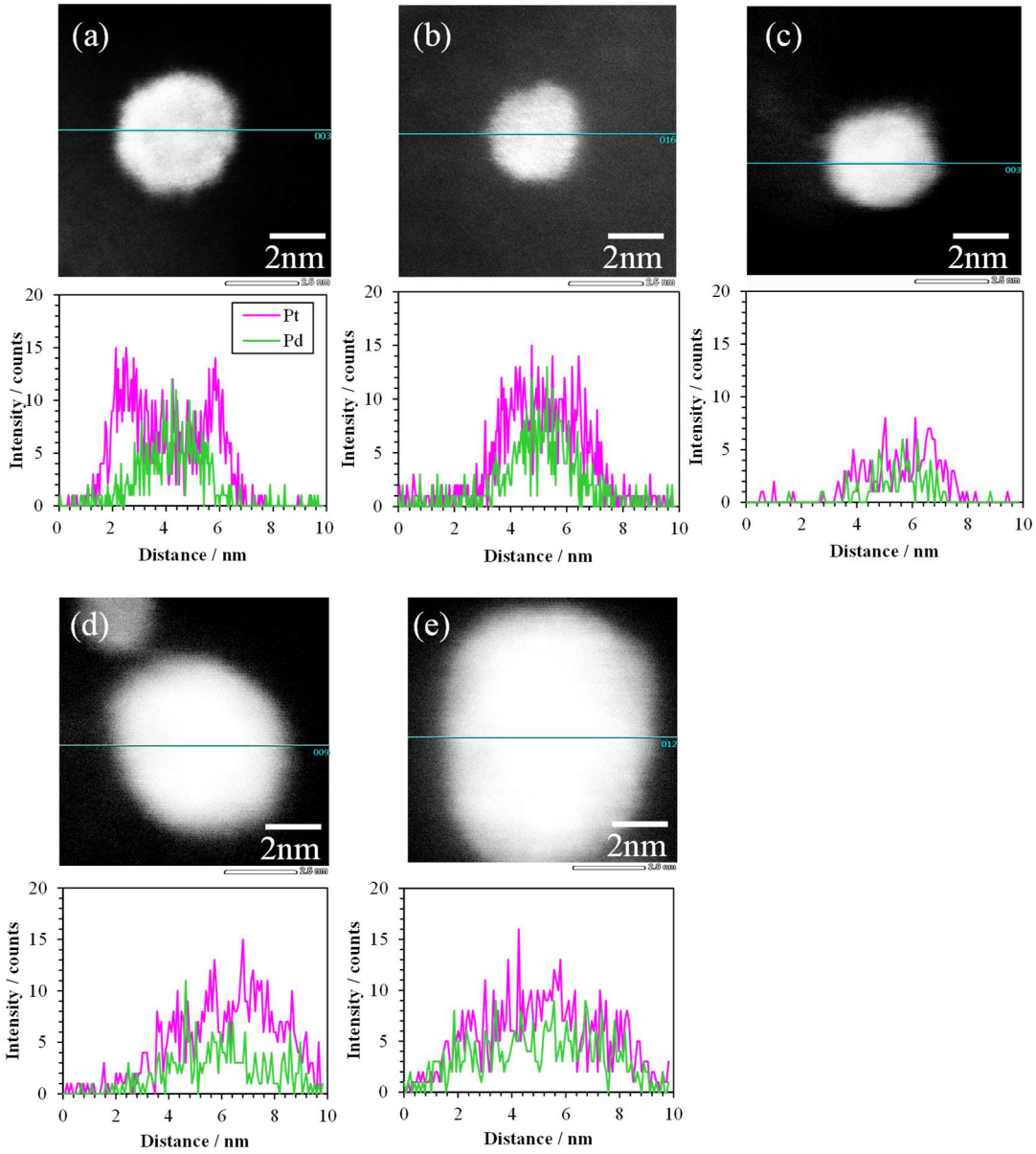

Figure 4-6 HAADF-STEM images and EDS line profiles of (a) Pt/Pd/C, (b) Air-300-20-Pt/Pd/C, (c) Air-300-30-Pt/Pd/C, (d) H2-200-20-Pt/Pd/C, and (e) H2-300-20-Pt/Pd/C.

4.3.4.2 Surface enhanced infrared absorption spectroscopy (SEIRAS)

Figure 4-7 shows the SEIRAS spectra of Pt/C, Pd/C, Pt/Pd/C, and heat-treated Pt/Pd/C catalysts. The Pt/C catalyst showed a SEIRAS peak around 2010 cm^{-1} while for the Pd/C catalyst the peak appeared around 1850 cm^{-1}. According to previous FTIR experiments on methanol oxidation at Pt and Pd electrodes, these peaks can be assigned to CO stretching vibrations on Pt on-top sites and Pd bridge sites, respectively [16]. In the case of the Pt/Pd/C catalyst, only one peak was observed, at 2010 cm^{-1}. This suggests that the CO was adsorbed only on the Pt surface of the Pt/Pd/C catalyst. Thus, we can conclude that the Pt/Pd/C catalyst prepared by the hydrogen sacrificial protection method has a core-shell structure. After heat treatment (heat-treated Pt/Pd/C), a peak at 1850 cm^{-1} was observed. This result indicates that CO was adsorbed on the Pd surface of the nanoparticles, in good agreement with the images observed by HAADF-STEM in the previous section.

With a longer heat treatment time under air (Air-300-30-Pt/Pd/C), the integrated peak area ratio of the CO bridge site and CO on-top site was increased relative to the shorter heat treatment (Air-300-20-Pt/Pd/C). Moreover, with heat treatment under H_2 atmosphere (H2-300-20-Pt/Pd/C), the integrated peak area ratio of the CO bridge site and CO on-top site increased than in the sample prepared under air atmosphere (Air-300-20-Pt/Pd/C). From these results, and the HAADF-STEM images (Fig. 4-5), we conclude that aggregation of nanoparticles on the carbon supports occurred in both cases, while the hydrogen atmosphere accelerated the oxidation of the carbon supports,

causing the detachment of nanoparticles from the supports.

Another effect of the higher-temperature treatment (H2-300-20-Pt/Pd/C) was that the peak of the CO bridge sites was more intense than under the lower-temperature treatment (H2-200-20-Pt/Pd/C). This result suggests that the diffusion of Pd atoms to the surface of the nanoparticles was promoted at high temperature.

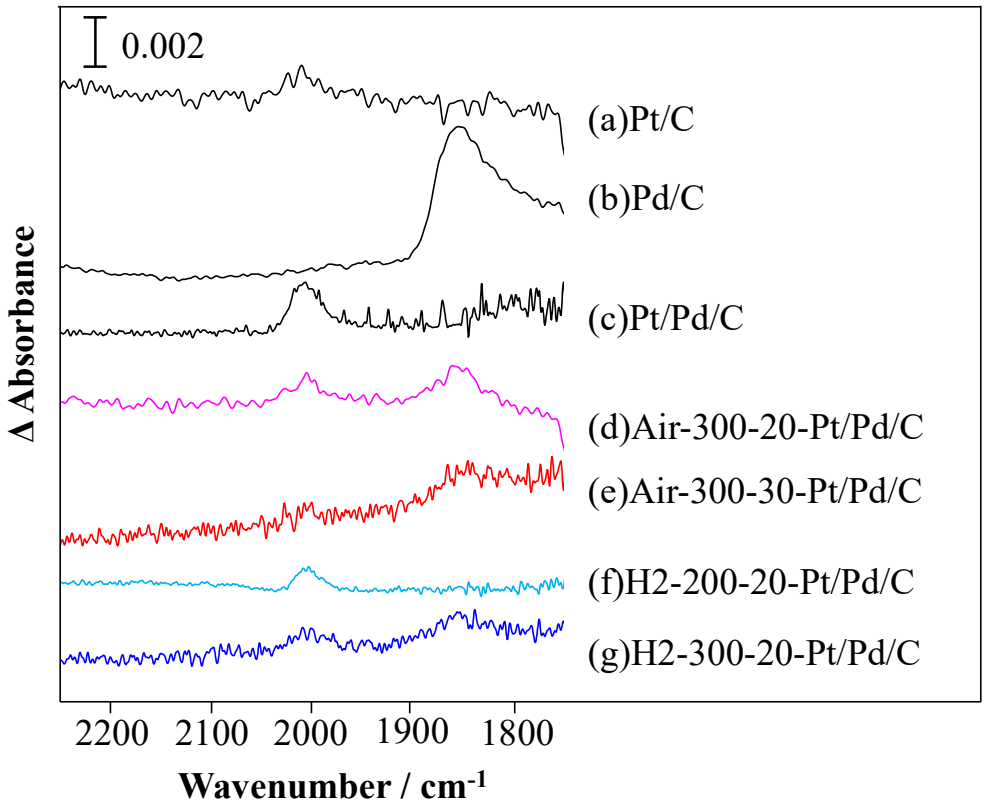

Figure 4-7 SEIRAS spectra of (a) Pt /C, (b) Pd/C, (c) Pt/Pd/C, (d) Air-300-20-Pt/Pd/C, (e) Air-300-30-Pt/Pd/C, (f) H2-200-20-Pt/Pd/C, and (g) H2-300-20-Pt/Pd/C.

4.3.4.3 Thermogravimetric analysis

Figure 4-8 shows the TG results for the Pt/Pd/C and heat-treated Pt/Pd/C catalysts. For the Pt/Pd/C catalyst, weight loss was observed from ca. 70 °C. This weight loss can be attributed to water adsorbed on the PVP, as the decomposition temperature of PVP is much higher than 70 °C. We also examined the weight loss behavior of Pt/Pd/C. In this case, three TG-DTA peaks were observed: the first peak at 165 °C, the second at 270 °C, and the third at 400 °C. I assigned these three peaks as the decomposition of PVP on the catalyst nanoparticles, the decomposition of PVP on carbon, and the combustion of the carbon support by the catalyst, respectively as mentioned in 4.3.1.

The catalyst prepared using a longer heating time under air (Air-300-30-Pt/Pd/C) shower a smaller weight loss than that prepared with a shorter heating time (Air-300-20-Pt/Pd/C).

According to these results, as the heat energy supplied during TG-DTA increased, decomposition of PVP occurred and the bulk PVP was gradually denatured above 200 °C.

In terms of effectiveness of PVP removal, the five catalysts lie in the following order: Air-300-30-Pt/Pd/C > H2-300-20-Pt/Pd/C ≅ Air-300-20-Pt/Pd/C > H2-200-20-Pt/Pd/C ≫ Pt/Pd/C. These results show that a heat treatment at 300 °C for 30 min under an air atmosphere best facilitates the removal of PVP from the nanoparticles.

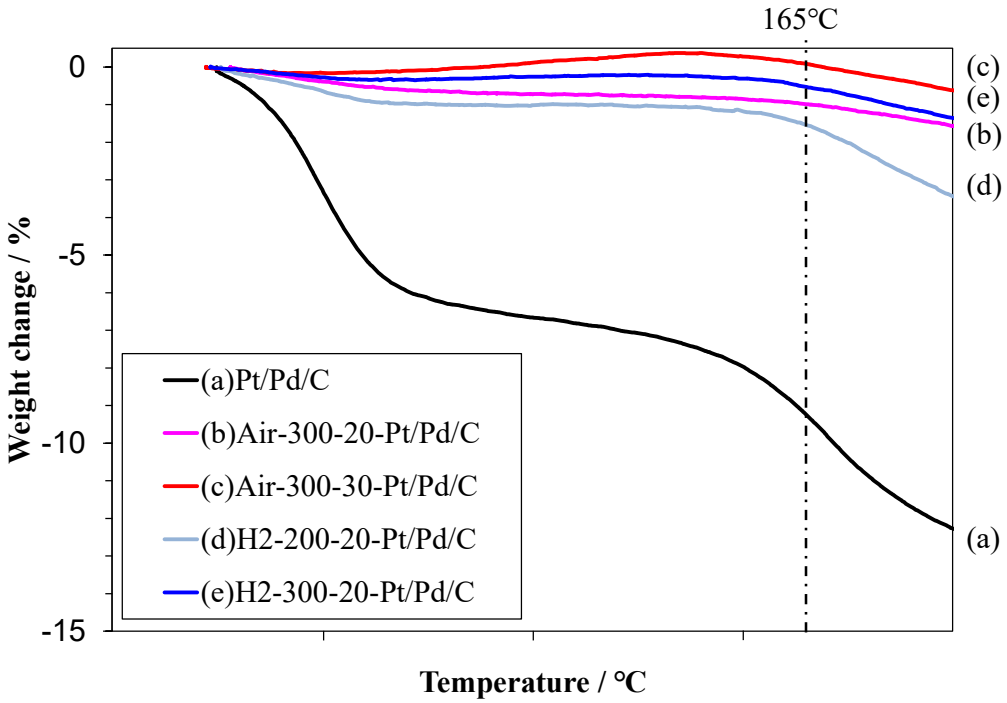

Figure 4-8 TG analysis of (a) Pt/Pd/C, (b) Air-300-20-Pt/Pd/C, (c) Air-300-30-Pt/Pd/C, (d) H2-200-20-Pt/Pd/C, and (e) H2-300-20-Pt/Pd/C.

Table 4-1 summarizes the characterization results of the Pt/Pd/C and heat-treated Pt/Pd/C catalysts. The Pt/C and Pd/C catalysts are also shown in the table. Table 4-1 also shows the heat treatment conditions for heat-treated Pt/Pd/C.

Table 4-1 Catalyst property of heat treated Pt/Pd/C, Pt/Pd/C, Pt/C, and Pd/C.

Samples	Atmosphere	Temperature (°C)	Time (min.)	Pt content (wt%)	Pd content (wt%)	Particle size※ (nm)	PVP residual (wt%)	CO bridge(Pd) / CO on top site (Pt)※※	Estimated surface components
Air-300-20-Pt/Pd/C	Air	300	20	24 ± 1.4	13 ± 0.8	3.7 ± 0.07	2.2 ± 0.9	1.68	Pt, Pd
Air-300-20-Pt/Pd/C	Air	300	30	20 ± 3,4	13 ± 0.3	3.8 ± 0.43	1.0 ± 0.7	1.98	Pt, Pd
H2-200-20-Pt/Pd/C	H_2	200	20	21 ± 1.2	11 ± 0.3	3.7 ± 0.13	3.2 ± 1.1	0.17	Pt, Pd
H2-300-20-Pt/Pd/C	H_2	300	20	22 ± 0.3	12 ± 0.6	4.2 ± 0.02	2.1 ± 1.2	2.29	Pt, Pd
Pt/Pd/C	–	–	–	20 ± 0.4	11 ± 0.1	3.0 ± 0.02	5.0 ± 1.3	.000	Pt
Pt/C	–	–	–	20 ± 0.2	0	2.5 ± 0.13	5.2 ± 0.3	0.00	Pt
Pd/C	–	–	–	0	14 ± 0.1	2.1 ± 0.30	1.9 ± 0.7	–	Pd

※The average crystalline size was calculated from X-Ray Diffraction patterns at (220).

※※The integrated peak area ratio of the CO bridge site / CO on top site by using SEIRAS.

4.3.5 Fuel cell performance of Pt/Pd nanoparticle catalyst

Figure 4-9 shows the fuel cell performance of the Pt/Pd/C and heat-treated Pt/Pd/C and Pt/C catalysts in terms of cell voltage. The Pt/Pd/C showed better performance than Pt/C. The optimal Pt/Pd/C ((b), (c), (e) the Pt loading amount was ca. 0.10 mg/cm^2) catalysts achieved a better performance than Pt/C (the Pt loading amount was ca. 0.20 mg/cm^2) despite a roughly 50% reduction in the amount of Pt used. This result indicates that preparing Pt/Pd/C catalysts by the hydrogen-sacrificial protection method is highly effective for reducing the usage of Pt in PEFCs. This result also demonstrates that the structure-controlled Pt atomic layer mentioned in Chapters 2 and 3 exhibits high ORR properties.

The cell voltage at 200 mA/cm^2 was taken as a guide to the catalytic activity because, in this potential region, the overpotential is dominant. The following results were observed. With a shorter heat treatment time under air (Air-300-20-Pt/Pd/C), the cell voltage was higher than with longer heat treatment (Air-300-30-Pt/Pd/C). However, the catalyst produced by heat treatment under H_2 atmosphere (H2-300-20-Pt/Pd/C) showed almost the same voltage as that produced under air (Air-300-20-Pt/Pd/C). Under the H_2 atmosphere, the higher-temperature heat treatment (H2-300-20-Pt/Pd/C) produced a catalyst with a greater cell voltage than that prepared at a lower temperature (H2-200-20-Pt/Pd/C).

According to these results, the cell performances lie in the following order:

Air-300-20-Pt/Pd/C (0.79 V) = H2-300-20-Pt/Pd/C (0.79 V) > Air-300-30-Pt/Pd/C (0.78 V) > Pt/Pd/C (0.75 V) > H2-200-20-Pt/Pd/C (0.74 V) > Pt/C (0.70 V) > Pt/C with a Pt loading of ca. 0.10 mg/cm^2.

I believe that the improvement in performance after heat treatment is due to the two effects of mixing Pt-Pd and removing PVP from nanoparticles.

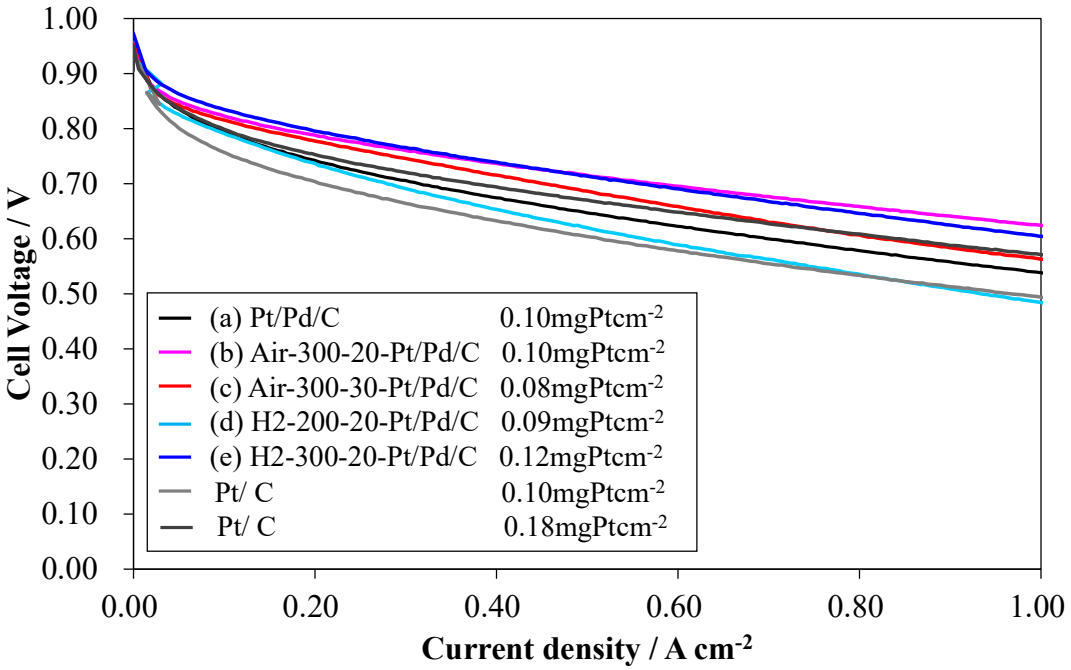

Figure 4-9 Cell voltages of (a) Pt/Pd/C, (b) Air-300-20-Pt/Pd/C, (c) Air-300-30-Pt/Pd/C, (d) H2-200-20-Pt/Pd/C, (e) H2-300-20-Pt/Pd/C, and Pt/C. Cell Temperature = 80 °C.

Figure 4-10 shows the result of the durability test, a retention rate of cell voltage at 200 mA/cm^2 cell current flow was plotted in a bar graph. It was confirmed that the durability was almost at the same level (95.7 to 99.2%) as compared to Pt/C (98.2%).

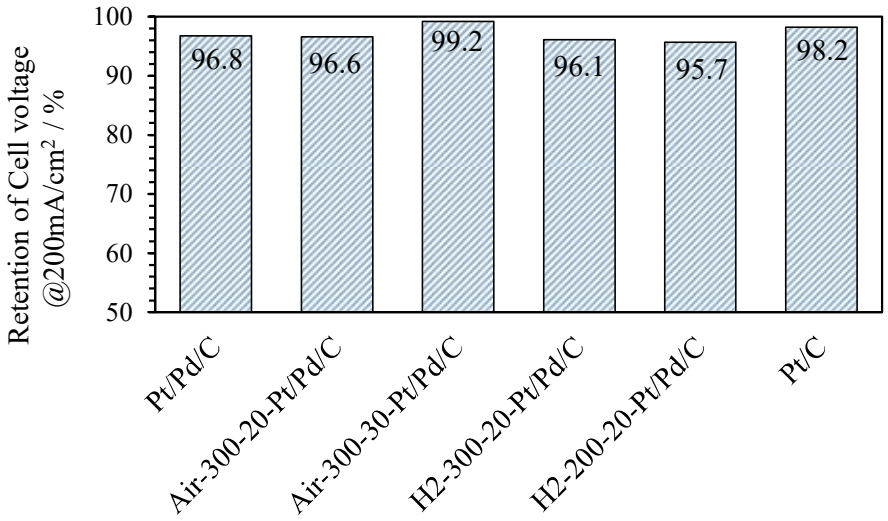

Figure 4-10 Retention rate of cell voltage at 200 mA/cm^2 cell current flow for each catalyst.

4.3.6 Factor contributing to Fuel Cell performance

The cell performances lie in a slightly different order to that of the efficiency of removal of PVP from the catalyst nanoparticles mentioned above. This suggests that the fuel cell performance is affected not only by the removal of PVP but also by the surface catalyst structure of Pt and Pd. For example, even though the removal of PVP tends to improve performance, H2-200–20-Pt/Pd/C has lower performance than Pt/Pd/C despite the removal of PVP. This indicates that the surface structure of the

catalyst contributes to the performance, as discussed in the analysis of the HAADF-STEM (Fig. 4-6) and SEIRAS (Fig. 4-7) results.

In terms of the catalyst structure (Table 4-1), the best fuel cell performance can be expected for catalysts with a mixture of Pt and Pd. This implies that it is important for the heat treatment to occur at ca. 300 °C (around the melting point of Pt and Pd nanoparticles). As described above, we surveyed the influence of time, temperature, and atmosphere on heat treatment. It appears that temperature may be the most important factor determining the performance of this core-shell catalyst.

Figure 4-11 shows the contour plot of cell performance, with the cell voltage on the z-axis, the integrated peak area ratio of the CO bridge sites/CO top sites (obtained from SEIRAS measurements) on the y-axis, and the amount of PVP remaining on the catalyst surface (obtained from TG-DTA) on the x-axis. The voltages were measured at 200 mA/cm^2. The y-axis indicates the surface condition of the catalyst.

As the integrated peak area ratio of the CO bridge sites/CO top sites increased, the cell voltage also increased when the amount of residual PVP was low, i.e., ca. 0.5–1.5 wt% (see Fig. 4-11, red area). However, when the ratio increased above 2.0, the cell voltage began to fall again. This result suggests that an excess number of Pd atoms were exposed to the catalyst surface under these heat treatment conditions (see Fig. 4-6, Fig. 4-7, and Table 4-1). Indeed, with an increasing number of Pd atoms on the catalyst surface, the cell voltage decreased: therefore, the bare Pd/C had a lower fuel cell performance than Pt/C.

Thus, we consider that other factors also contribute to the fuel cell performance: for example, the Pt–Pt bond distance and/or amount of PVP remaining on the catalyst surface. To estimate the Pt–Pt bond distance on the catalyst surface of this core-shell structure is difficult. An earlier X-ray Absorption Fine Structure (XAFS) experiment mostly revealed information about the structure of the bulk, which was found to be partially mixed Pt–Pd bonding [17-18]. However, it is quite difficult to focus specifically on the surface structure of a core-shell catalyst. Herein, we estimated the surface properties from an electrochemical spectroscopic point of view using SEIRAS. The SEIRAS results contain information on the surface structure of the catalyst in terms of the adsorption sites of CO molecules, which vary depending on the catalyst surface morphology.

Meanwhile, when heat treatment was carried out, the amount of PVP remaining on the catalyst surface decreased. The cell performance was improved by this surface cleaning (i.e. the decomposition of PVP on the catalyst nanoparticles) when the integrated peak area ratio of the CO bridge sites/CO top sites was between 0.5 and 2.0. However, when the ratio was below 0.5 the cell voltage remained low. This may imply that the surface Pt–Pt bonding was not optimized under these conditions.

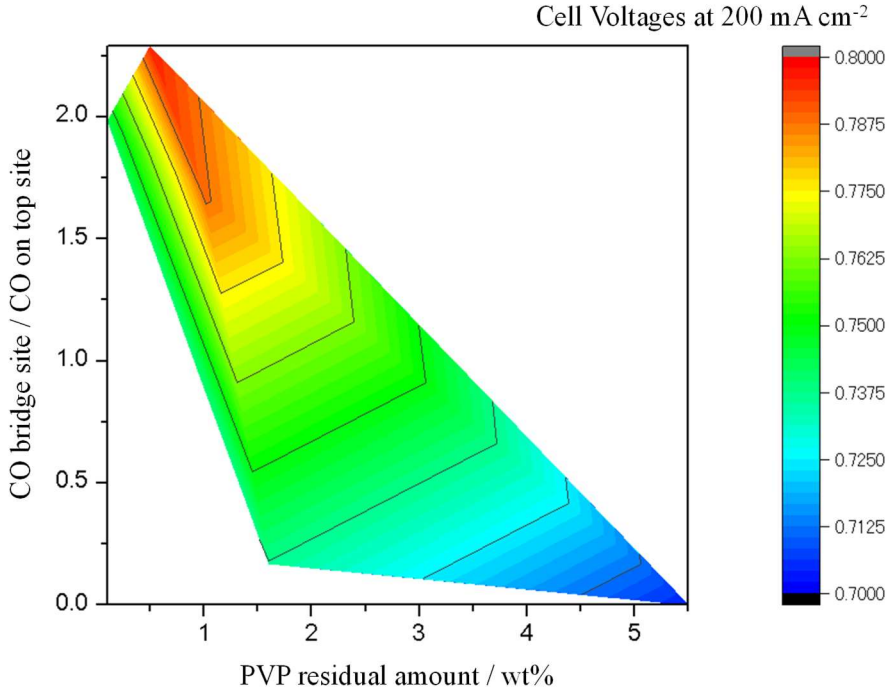

Figure 4-11 Contour plot showing the dependence of cell performance on the structural differences of the samples.

Figure 4-12 shows the relationship between cell performance and the integrated peak area ratio of the CO bridge sites/CO top sites. As shown in Fig. 7, this ratio was itself affected by the amount of PVP remaining on the catalyst surface. Therefore, to clarify the specific effect of the ratio, Fig. 4-12 plots the cell voltage when the amount of PVP on the catalyst surface was fixed at 1.5 wt%.

As can be seen, the cell voltage showed a maximum when the integrated peak area ratio of the CO bridge sites/CO top sites was ca. 1.5. This implies that Pd islands on Pt nanoparticles are highly effective for catalytic activation. According to a DFT

calculation, the optimized structure of the Pt/Pd core-shell catalyst featured Pd atoms forming islands on the Pt nanoparticles [19-20].

It is presumed that Pd is relatively easily oxidized by oxygen compared with Pt (i.e. Pd sites are more favorable for the adsorption of oxygen atoms), and the oxygen adsorbed on Pd promotes oxygen adsorption on nearby Pt by electron transfer. Therefore, this implies that the surface Pd atoms improve the catalyst performance.

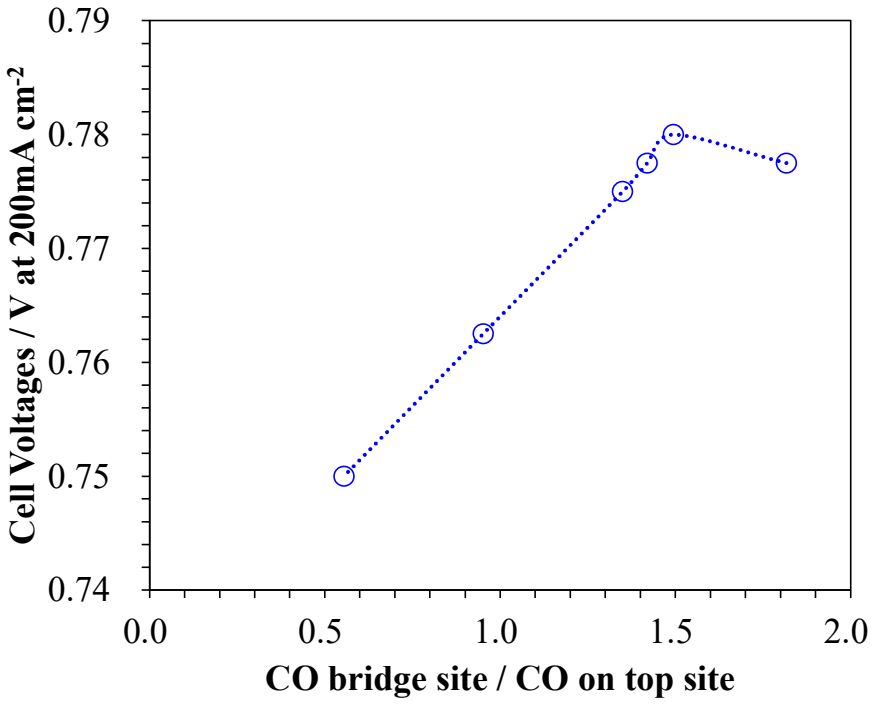

Figure 4-12 The relationship between cell performance and ratio of CO bridge sites/CO top sites for a fixed PVP residual amount = 1.5 wt%.

4.4 Conclusions

In this chapter, the effect of the Pt atomic layer of this doctoral thesis on the fuel cell performance was verified by investigating the fuel cell performance of Pt/Pd/C and heat-treated Pt/Pd/C with a structure-controlled Pt atomic layer. Pt/Pd/C and heat-treated Pt/Pd/C catalysts were characterized by TEM-EDX, SEIRAS, and TG. The optimal Pt/Pd/C catalyst achieved a better performance than Pt/C despite a roughly 50% reduction in the amount of Pt used. Heat treatment of the Pt/Pd/C catalyst effectively improved the cell performance. In core-shell catalysts, the outermost surface has conventionally consisted of Pt. However, the performance can be enhanced if different metals, such as Pd, are used to substitute Pt on the surface or to form a Pt alloy. Based on the present results, the fuel cell performance (oxygen reduction activity) can be improved even if Pd is precipitated in the form of an island without being dissolved as a solid solution.

4.5 References

(1) T. Toda, H. Igarashi, M. Watanabe, J. Electroanal. Chem. (1999) 460 258-262.

(2) U. A. Paulus, A. Wokaun, G. G. Scherer, T. J. Schmidt, V. Stamenkovic, N. M. Markovic, P. N. Ross, Electrochim. Acta (2002) 47 3787-3798.

(3) J. Zhang, Y. Mo, M. B. Vukmirovic, R. Klie, K. Sasaki, R. R. Adzic, J. Phys. Chem. B (2004) 108 10955-10964.

(4) M. Chiwata, H. Yano, S. Ogawa, M. Watanabe, A. Iiyama, H. Uchida, Electrochemistry (2016) 84 133-137.

(5) L. Wang, W. Gao, Z. Liu, Z. Zeng, Y. Liu, M. Giroux, M. Chi, G. Wang, J. Greeley, X. Pan, C. Wang, ACS Catal. (2018) 8 35-42.

(6) J. Zhang, M. B. Vukmirovic, Y. Xu, M. Mavrikakis, R. R. Adzic, Angew. Chem. Int. Ed. (2005) 44 2132-2135.

(7) Y. Wang, N. Toshima, J. Phys. Chem. B (1997) 101 5301-5306.

(8) H. Naohara, Y. Okamoto, N. Toshima, J. Power Sources (2011) 196 7510-7513.

(9) Z. Liu, C. Yu, I. A. Rusakova, D. Huang, P. Strasser, Top. Catal. (2008) 49 241-250.

(10) D. Li, C. Wang, D. Tripkovic, S. Sun, N. M. Markovic, V. R. Stamenkovic, ACS Catal. (2012) 2 1358-1362.

(11) D. Raciti, J. Kubal, C. Ma, M. Barclay, M. Gonzalez, M. Chi, J. Greeley, K. L. More, C. Wang, Nano Energy (2016) 20 202-211.

(12) K. Matsumoto, T. Iijima, M. Hiyoshi, 224th ECS Meeting 1617 Thursday,

October 31, 2013.

(13) Y. Borodko, S. E. Habas, M. Koebel, P. Yang, H. Frei, G. A. Somorjai J. Phys. Chem. B (2006) 110 23052-23059.

(14) J. B. Darby, K. M. Myles, Metall. Mater. Trans. (1972) 3 653-657.

(15) P. Buffat, J. Borel, Phys. Rev. A 1 (1976) 3 2287-2296.

(16) N. Todoroki, H. Osano, T. Maeyama, H. Yoshida, T. Wadayama, Appl. Surf. Sci. (2009) 256 943-947.

(17) X. Wang, Y. Orikasa, Y. Takesue, H. Inoue, M. Nakamura, T. Minato, N. Hoshi, Y. Uchimoto, J. Am. Chem. Soc. (2013) 135 5938-5941.

(18) S. Nagamatsu, S. Takao, G. Samjeské, K. Nagasawa, O. Sekizawa, T. Kaneko, K. Higashi, T. Uruga, S. Gayen, S. Velaga, M. K. Saniyal, Y. Iwasawa, Surf. Sci. (2016) 648100-113.

(19) T. Ishimoto, M. Koyama, J. Phys. Chem. Lett. (2016) 7 736-740.

(20) R. Al-Shareef, M. Harb, Y. Saih, S. O. Chikh, M. A. Roldan, D. H. Anjum, E. Guyonnet, J. P. Candy, D. Y. Jan, S. F. Abdo, A. A. Tapia, O. Proux, J. L. Hazemann, J. M. Basset, J. Catal. (2018) 363 34-51.

Chapter 5

GENERAL CONCLUSION AND FUTURE PROSPECTS

5.1 General conclusion

This thesis has examined the evidence of the feasibility of core-shell catalysts and the proposed factors that contribute to their performance. In this study, the correlation between the Pt/Pd model electrode and the Pt and Pd nanoparticle electrode prepared by the hydrogen sacrificial protection method was clarified by spectroscopic and electrochemical methods. Finally, discussed the feasibility of the core-shell catalyst and proved that the effectiveness of Pt atomic layer on Pd nanoparticles by hydrogen sacrificial protection method.

In Chapter 1, the background of the present study was described.

In Chapter 2, Pt/Pd polycrystalline electrodes were prepared by the sacrificial hydrogen method and their structures and ORR properties were discussed, and TEM and AR-XPS measurements indicated that the Pt/Pd polycrystalline electrodes have a bulky structure and the electronic state of the Pt atomic layer on the Pd polycrystal is changed, resulting in stronger electron donation from the underlying Pd. The ORR characteristics showed that the exchange current density was improved by more than a factor of 5 with respect to the Pt polycrystal. This effect was considered to be the suppression of OH adsorption (resistance to oxidation), which is an intermediate of the ORR reaction of Pt by the aforementioned electron donation.

In Chapter 3, Pt/Pd nanoparticle catalysts were prepared by sacrificial hydrogen method based on the principle of Chapter 2, and the coverage of Pt atomic layer on Pd nanoparticles was discussed from the structural analysis by XRD, TEM, and SEIRAS. In the case of 1 ML, the Pt coverage is insufficient, but for 2 ML and above, complete coverage is possible.

In Chapter 4, the fuel cell performance of the structure-controlled Pt atomic layer prepared in Chapter 3 was examined. 2ML showed the highest battery performance. Furthermore, the fuel cell properties of 2ML Pt/Pd/C were further improved by heat treatment to remove PVP. By following the catalytic structural changes during the heat treatment process, it was found for the first time that the decomposition of PVP and the mixing of Pt/Pd proceeded simultaneously. I proposed that the improvement of the fuel cell performance in this doctoral thesis is due to these two effects.

5.2 Future prospects

For future developments, it is necessary to clarify the correlation between the performance of the fuel cell and the structure, pursue the mechanism of high activation of the catalyst, and design the catalyst based on the principle. As a specific example, the Pt-Pt bond length is calculated from the radial distribution function of Pt using the X-ray absorption fine structure (XAFS) with time and three-dimensional resolution under fuel cell operation. Clarify the actual catalyst structure (80 °C, low pH, potential control, fuel gas atmosphere) of the core-shell catalyst, investigate the correlation with

the performance evaluation results, and if performance improvement by alloying Pt-Pd is proposed. Then this paper will be improved and seems possible to verify the mechanism. In addition, the findings from XAFS research will help in further new catalyst designs.

In addition, although Pd was used as core particles of the core-shell in this thesis, Pd is also expensive material. The selection of core particles other than Pd is effective. As a new finding in this thesis shows that even a dual catalysts that were originally phase-separated can be alloyed with certain treatments. Therefore, it is considered that the possibility of developing a new catalyst that has never existed has been suggested by examining alloy catalysts that were originally phase-separated even for metals other than Pd. In recent years, Kitagawa et al. (Scientific Reports (2016) 6 28265) have proposed research on new high-performance nanoparticles by fusing different elements because the properties of nanoparticles are significantly different from those of bulk. The results of this thesis are close to the idea of elemental fusion and form a metastable structure by synthesizing core-shell nanoparticles from many synthetic routes and supplying energy from the outside such as heat treatment without sticking to the hydrogen sacrificial protection method. From the above, it is possible to synthesize innovative fuel cell catalysts by creating nanoparticles whose structure has changed energetically.